Investigation of a Wideband Circularly Polarized Stacked-Patch Antenna for Global Navigation Satellite Systems

Investigation d'une antenne circulairement polarisée patch empliée à large bande pour les systèmes mondiaux de navigation par satellite

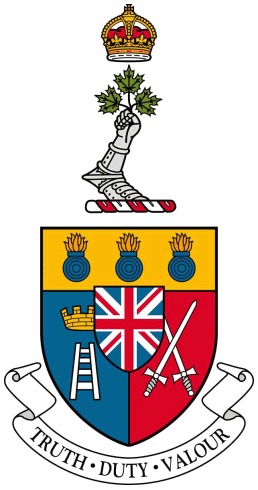

A Thesis Submitted to the Division of Graduate Studies
of the Royal Military College of Canada
by

Brian Scott Hines, BEng
Captain

In Partial Fulfillment of the Requirement for the Degree of
Master of Applied Science in Computer Engineering

May, 2024

Acknowledgements

I would like to express my gratitude to Dr. Yahia Antar, my thesis supervisor, for his mentorship and guidance throughout my graduate studies. His consistent patience, ongoing support, and valuable feedback was essential to the success of this thesis.

To Mr. Pier Drouin, a member of the Electrical and Computer Engineering Department Technical Support Staff, I am appreciative of his invaluable contribution to the fabrication of the devices appearing in this thesis.

I would also like to thank Dr. Joey Bray for his insight and guidance with the use of the anechoic chamber. I also extend my thanks to Dr. Michel Clénet and his team at DRDC for inspiring this thesis and for their technical expertise on GNSS antenna systems.

Finally, to my loving wife BJ, who now knows a lot more about GNSS antenna design. I am immensely grateful for her care and support during my master's program.

Abstract

Hines, Brian, M.A.Sc. Royal Military College of Canada, May 2024. Investigation of a Wideband Circularly Polarized Stacked-Patch Antenna for Global Navigation Satellite Systems. Thesis supervised by Dr. Yahia Antar.

State-of-the-art global navigation satellite system (GNSS) antennas, feature wideband performance that support several services across the entirety of the GNSS L-band, 1.16-1.61 GHz. However, they are typically challenging to design due to the need of a high-performance feed network that can support circularly polarized (CP) operation. In addition, many wideband GNSS antennas are large owing to lower permittivity substrates or the use of probes and air gaps. A common approach to reducing the size of these antennas is through the use of high permittivity materials, but can adversely affect some antenna performance.

This thesis investigates the use of a multi-layer, uniform permittivity substrate, balancing high-performance with antenna size. This led to the development of a wideband, dual-fed aperture-coupled stacked-patch antenna driven by an adapted ultra-wideband (UWB) branch-line coupler (BLC) in an attempt to meet all GNSS antenna requirements. Antenna simulations were conducted in Ansoft high frequency structure simulator (HFSS), comparing well with experimental results attaining a gain of $2.2 - 5.3$ dBic, impedance bandwidth (IBW) $> 42.8\%$ and axial ratio bandwidth (ARBW) of 20% covering the upper and lower L-band signals. A limited study into a printed circuit board (PCB) integrated antenna including the use of a stripline layer with microstrip-to-stripline transitions was attempted with preliminary results included. Finally, a modified version of the standalone antenna was successfully investigated in a 2×2 sequentially rotated array (SRA) which could prove valuable in future projects such as GNSS phased arrays.

Keywords: Antenna Array, Aperture-Coupled, Circular Polarization, GNSS Antenna, Printed Circuit Board, SRA, Stacked-Patch, Wideband.

Résumé

Hines, Brian. M.Sc.A. Collège militaire royal du Canada, Mai, 2024. Investigation d'une antenne circulairement polarisée patch empliée à large bande pour les systèmes mondiaux de navigation par satellite. Thèse dirigée par Dr. Yahia Antar.

Les antennes de systèmes mondiaux de navigation par satellite (GNSS) de pointe sont dotées de performances à large bande qui prennent en charge plusieurs services dans l'ensemble de la bande L GNSS, 1,16-1,61 GHz. Cependant, elles sont généralement difficiles à concevoir en raison de la nécessité d'un réseau d'alimentation haute performance qui peut prendre en charge le fonctionnement à polarisation circulaire. De plus, de nombreuses antennes GNSS à large bande sont grandes en raison de substrats à permittivité plus faible ou de l'utilisation de sondes et des entrefers. Une approche courante pour réduire la taille de ces antennes consiste à utiliser des matériaux à haute permittivité, mais cela peut nuire à certaines performances de l'antenne.

Cette thèse étudie l'utilisation d'un substrat multicouche à permittivité uniforme, en ajustant les hautes performances avec la taille de l'antenne. Cela a mené à la mise au point d'une antenne à large bande empliée, avec deux lignes d'alimentation microstrip et deux fentes, actionée par un coupleur d'embranchement adapté à bande ultra-large dans le but de répondre à toutes les exigences d'antenne GNSS. Des simulations d'antenne ont été effectuées avec le logiciel Ansoft (HFSS) et comparées bien avec les résultats expérimentaux atteignant un gain de 2,2 - 5,3 dBic, avec une bande d'impédance $> 42,8\%$ et la bande passante de rapport axial de 20% couvrant les signaux de bande L supérieure et inférieure. Une étude limitée sur une antenne munie d'une carte de circuit imprimé, avec une couche de stripline avec des transitions de microstrip-à-stripline a été tentée avec résultats préliminaires inclus.

Enfin, une version modifiée de l'antenne autonome a été étudiée avec succès dans un réseau à rotation séquentielle (SRA) de 2×2, ce qui pourrait s'avérer avantageux dans de futurs projets tels que les réseaux de phase GNSS.

Mots Clés: réseau d'antennes, doublement alimentée et couplée à l'ouverture, polarization circulaire, antenne de GNSS, carte de circuit imprimé, SRA, patch empilée, à large bande.

Table of Contents

List of Tables

List of Figures

List of Symbols and Abbreviations

AF	Array Factor
AR	Axial Ratio
ARBW	Axial Ratio Bandwidth
ATL	Artificial Transmission Line
AUT	Antenna Under Test
BLC	Branchline Coupler
dB	Decibel
dBi	Decibel Isotropic
dBic	Decibel Isotropic Circularly Polarized
DFN	Dual-feed Network
DRDC	Defence Research and Development Canada
EM	Electromagnetic
EW	Electronic Warfare
FBR	Front-to-back Ratio
FBW	Fractional Bandwidth
GBW	Gain Bandwidth
GNSS	Global Navigation Satellite System

HFSS	High Frequency Structure Simulator
HPBW	Half-Power Beamwidth
IBW	Impedance Bandwidth
LHCP	Left Hand Circular Polarization
LNA	Low Noise Amplifier
PCB	Printed Circuit Board
PNT	Positioning, Navigation and Timing
QFN	Quad-feed Network
QWT	Quarter-wave Transformer
RCAF	Royal Canadian Air Force
RF	Radio Frequency
RHCP	Right Hand Circular Polarization
RMC	Royal Military College
SOTM	Satellite-on-the-move
SRA	Sequentially Rotated Array
UWB	Ultra-wideband
WPD	Wilkinson Power Divider
$\tan\delta$	Loss Tangent
ϵ_r	Relative Permittivity
f_0	Operating Frequency
λ_0	Wavelength in Free Space
λ_g	Guided Wavelength
Z_0	Characteristic Impedance

Chapter 1

Introduction

1.1 Motivation

The objectives of this thesis are to investigate and design a wideband and compact antenna that would be suitable for global navigation satellite system (GNSS) applications. Why GNSS antennas became an area of interest requires further background information. In 2023, representatives from Royal Military College (RMC) and Defence Research and Development Canada (DRDC) met to discuss current projects that this thesis could support as these two institutions have had a long-standing relationship with antenna design and microwave engineering projects. DRDC had revealed that they had a GNSS array project commissioned by the Royal Canadian Air Force (RCAF) as this continues to be an important area of interest to this day. GNSS arrays are a valuable area of study due to their beamforming or spatial filtering characteristics which can be very useful in satellite tracking or electronic warfare (EW) applications.

There tends to be a trade-off in designing GNSS antennas – performance versus size. This is for several reasons. First, the wavelength within the GNSS L-band is relatively large and since the size of an antenna is proportional to wavelength, which can necessitate a relatively large radiating aperture. Second, for wideband microstrip or patch antennas, this requires multiple resonant structures that can increase the size and weight of an antenna. Furthermore, GNSS signals are right-hand circularly polarized (RHCP), and can demand large and complicated feed networks further adding to the size of these devices. Finally, small

GNSS antennas can be designed to perform well within a limited bandwidth, whereas high performance devices that feature wide bandwidth tend to be large and require components that would generally not make it suitable in an array such as with the use of probes and air gaps. Conversely, the use of high permittivity materials to reduce the size of these antennas also affects bandwidth performance.

Consequently, a survey of existing wideband GNSS antennas was conducted. This uncovered a gap in design capability. There were no antennas that were not large, according to GNSS standards, did not use components such as air gaps, probes, and/or high permittivity materials, with wideband performance that were specifically intended to be used both as a standalone antenna and as an element in an array. There are a multitude of GNSS antennas that have been published, but many of these designs were standalone systems that focus on performance requirements such as polarization purity, radiation pattern or phase center stability for improved ranging capability.

1.2 Thesis Objectives

To further investigate these areas of interest, insight into many sources including reports that had antennas operating inside and outside the GNSS L-band was required. The intent of this investigation was to understand how to adapt these antennas to be an effective GNSS standalone antenna and be suitable as part of a GNSS array. There were two antenna configurations that were identified as promising. The first was an aperture-coupled stacked-patch antenna used for satellite-on-the-move (SOTM) applications in the Ka-Band [1]. The antenna has a dual feed network (DFN) that uses a miniaturized BLC in a PCB stack-up shown in Fig. 1.1. A dual-polarized design in [2] was found much later in this investigation that provides similar insight into the use of the orthogonal crossed-slots, though, this design was used for dual-linear polarization and not CP applications.

The second design inspired the use of a uniform permittivity substrate where the primary and parasitic patches of the aperture-coupled stacked patch antenna in [3] are both on a substrate with the same relative permittivity (ϵ_r) and height (h). Upon assessment of these

designs, the idea of using a uniform permittivity, multi-layer substrate to create both a wideband GNSS antenna element and a GNSS 2×2 Sequentially Rotated Array (SRA) led to the development of the following thesis objectives:

- Investigate the design of wideband, dual-fed aperture-coupled stacked-patch antenna using a multi-layer, uniform permittivity substrate that meets all GNSS state-of-the-art requirements listed in Section 2.3.8.
- Integrate the optimized antenna in a wideband GNSS 2×2 SRA to study its performance in an antenna array configuration and assess whether this design would be suitable for further implementation into a GNSS phased array. A full list of design requirements are in Section 2.9.6.

To achieve these objectives, thorough research was carried out on each of the antenna components such as compact transmission line and slot design, wideband microstrip patch techniques, multi-layer laminate design and manufacturing processes including the use of prepreg, wideband matching networks, the critical nature of feed networks including their various configurations and finally the integration of all these components.

At the outset, it was revealed that one of the critical factors to a wideband antenna is the appropriate use of a corresponding high-performance feed network. One of the key difficulties in these designs is the issue of stable power division and phase shift over a bandwidth wide enough to excite RHCP necessary to capture GNSS signals, while also achieving a reduced size. This research led to the adaptation of a BLC found at [4] that has wideband performance and a compact size in comparison to a conventional BLC.

Further to the idea a robust GNSS standalone system, is its suitability in an array. As such, a study of how this antenna could be integrated into a GNSS array would be valuable since there has been limited discussion on GNSS arrays in literature over the last decade. What would be of particular interest is the study of a Sequentially Rotated Array (SRA), since this antenna configuration has been well known for its wideband design and polarization purity.

Originally, the intent of this thesis was to study the PCB integrated antenna methodology

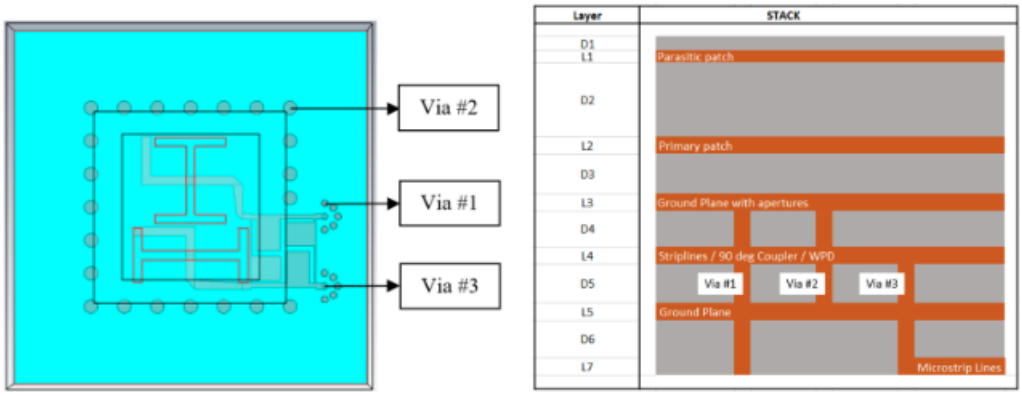

(a) **(b)**

Figure 1.1: SOTM aperture-coupled stacked-patch antenna (a) Top view (b) Side view [1].

from [1], in part so that the antenna element could be integrated directly with the use of radio frequency (RF) components such as low-noise amplifiers (LNAs) and reconfigurable switches. Furthermore, by placing a microstrip feed network closer to the center of the antenna element, its overall size could be decreased. The key feature of this design was the use of a microstrip-to-stripline transitions, necessary with the introduction of a stripline layer between the radiating aperture and the microstrip layer. However, there was limited success in the adaptation of the design for GNSS applications. As such it was decided to change the thesis objectives to those pertaining to the GNSS SRA. For completeness, the information regarding this original investigation including background info, objectives and simulation results is included in Chapter 4.

1.3 Methodology

The investigation of all antennas was conducted in several stages for each of the proposed devices in this thesis. Primarily, using MATLAB, the first stage included the evaluation of computer aided design analytical equations and expressions that were needed to determine the appropriate sizes and positions of the stacked patches, ground plane slots, feed network and substrates. The second stage was the simulation stage and was conducted in Ansoft HFSS needed to validate the analytical equations and optimize device performance. Then, designs

were exported as AutoCAD (.dxf), gerber (.gbr) and drill data (.drl) files for fabrication.

The final stages included fabrication and experimental testing. Only Antenna 1 and the SRA were fabricated and tested entirely at RMC. Reflection coefficient, $|S_{11}|$, measurements were performed using an Agilent Technologies N5244A PNA-X Network Analyzer across 121 separate frequencies. Antenna pattern measurements were captured using a far-field anechoic chamber measurement set-up [5]. Initially calibration of the chamber was conducted using two 1 to 18 GHz horn antennas as shown in Fig. 1.2(a). Both antenna configurations were used as the antenna under test (AUT) in the chamber. Measurements in the elevation plane were swept from $-90^\circ \leq \theta \leq 90^\circ$ in 1° increments. The radiation pattern of the antenna would be collected by measuring the transmission coefficient amplitude $|S_{21}|$ data across 121 separate frequencies. This pattern sweep would be carried out for the two standard radiation pattern cuts in the azimuth plane $\phi = 0^\circ$ and $\phi = 90^\circ$. However, due to inconsistent results and the discovery of several RHCP and LHCP wideband spiral antennas as shown in Fig. 1.2(b), the entire test was repeated using the CP antennas resulting in more accurate and comprehensive data. These results are further discussed in chapters 3 and 5.

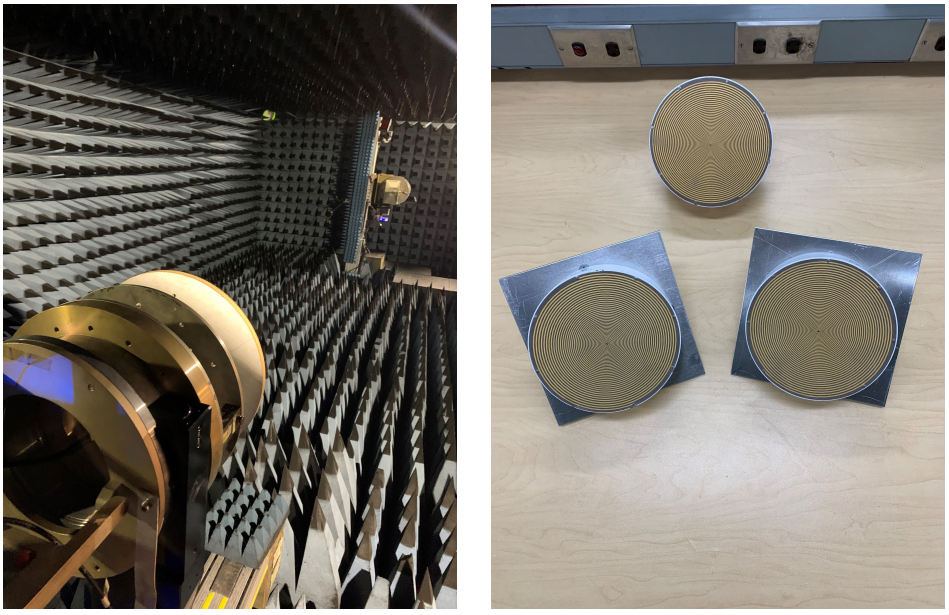

(a) **(b)**

Figure 1.2: Experimental test set-up (a) RMC anechoic chamber set-up with transmit horn antenna (b) Wideband spiral antennas

1.4 Contributions

Due to the wide range of activities required as part of this thesis, there were several contributions including the two antenna configurations that were successfully designed and tested and one novel antenna fabrication process with a complete list of contributions below:

- Antenna 1: A novel GNSS standalone antenna achieving nearly wideband performance while also being compact in size using a dual-fed design integrating an adapted compact UWB two-section BLC [4], and an orthogonal slotted ground plane design from the aperture-coupled stacked-patch antenna in [1]. This antenna is comparable to other state-of-the-art GNSS antenna designs found in literature. Due to the compact nature of the feed network, this antenna can integrated into an array not often common amongst wideband GNSS designs.

- Antenna 2: A preliminary study in a PCB integrated antenna, which included the use of a stripline layer and microstrip-to-stripline transitions for each of the feed lines [1][6]. Although this antenna design did not yield successful results, it does provide an opportunity for other works to delve deeper into the use of stripline configurations integrated with aperture-coupled stack-patch designs.

- Design of a novel 2×2 SRA using a sequential parallel array feeding network from [7], and Antenna 3, a modified version of Antenna 1. This array was wideband while also being compact and included a 3 dB increase in gain than that at the element level. This array design is comparable in performance and size to other state-of-the-art GNSS antenna arrays published in literature. With the simple incorporation of individual input ports to each of the elements, this 2×2 SRA could be integrated into a phased array design for future GNSS projects.

- A novel RMC antenna fabrication procedure: As all antenna fabrication part of this thesis was conducted at RMC, a novel procedure with the use of multi-layer core laminates and prepreg was required in the realization of Antenna 1 and 2×2 SRA.

This thesis outlines the investigation and design procedures for both a GNSS antenna

and antenna array. Detailed crucial equations essential to the investigation are presented in the main body, with supplementary information included in the relevant appendices for easy reference. The conclusions and suggestions derived from the analysis, design, optimization, and testing stages are robust and hold value for future endeavors that would be built upon this thesis.

1.5 Organization

This document is presented in six chapters including this introduction and subsequent chapters. Chapter 2 comprises of a comprehensive literature survey which covers some background of antenna theory, feed network design, and wideband GNSS antennas. Chapter 3 follows the investigation of Antenna 1, a uniform permittivity substrate, dual-fed, aperture-coupled, stacked-patch antenna, adapted from several sources [1][3][4]. Chapter 4 describes the limited investigation into the PCB integrated design of Antenna 2. Chapter 5 covers the design of Antenna 3, an altered version of Antenna 1, as an antenna element in a 2×2 SRA and provides discussion into the suitability for future studies such as GNSS phased array applications. Chapter 6 summarizes the results presented in previous chapters and some potential avenues for future work. All appendices capture further supporting information regarding the antenna configurations explored in this thesis including simulation and experimental testing results and images of the fabrication process conducted at RMC.

Chapter 2

Literature Survey

2.1 Introduction

GNSS is vital to many industries including those in positioning such as geodetic or surveying applications, navigation whether land, air or maritime, and some of the most accurate timing services found anywhere on earth. Following the introduction of GPS (USA) and then GLONASS (Russia) in approximately 1990 [8], the utilization of GNSS technology has expanded worldwide, extending beyond military use to encompass commercial and consumer sectors. As such, the interest and research around GNSS has only continued to increase as more GNSS services have come online. As of today, these efforts include the development of effective antennas and receivers that are capable of capturing signals from one or multiple satellite services in the GNSS L-band. In addition to GPS and GLONASS, there are the Galileo (European Union), Beidou (China) also known as Compass, GNSS services which are illustrated in Fig. 2.1.

There are several methods of capturing multiple signals including systems with multi-antenna, reconfigurable or multi-band antennas, with wideband antennas offering the ability to receive any of the services within the GNSS L-band without additional complicated circuitry that add weight and cost to a receiver [9]. Nonetheless, design of the wideband antenna comes with its own set of challenges mainly due to the use of feed networks that are required to support the axial ratio (AR), impedance matching, gain and radiation pattern characteristics that would be needed across the entire GNSS L-band. Finally, if a wideband antenna

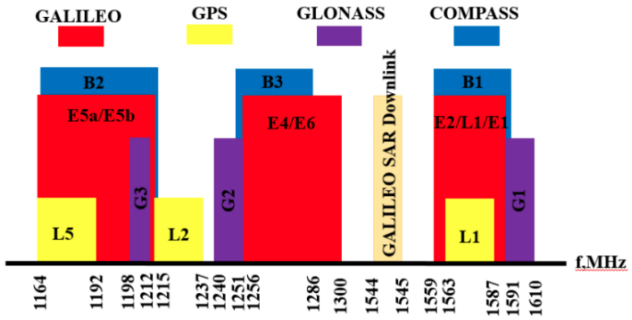

Figure 2.1: GNSS L-band frequency spectrum [9].

has suitable performance and is compact enough, it can be used as part of a larger array that would provide certain enhancements in performance including increased bandwidth and gain along with use phased array applications which is why is remains a topic of much research to-date.

This chapter provides a summary of antennas with an emphasis on their feed networks, and the current state-of-the-art in this area of study. This chapter will commence with a review of antenna theory, basics of feed networks that will be pertinent for establishing the foundation for the remainder of this thesis. Next, specific GNSS antenna and feed network performance requirements are disclosed that are inherent to the thesis objectives. Additionally, there will be discussion on antenna array principles, followed by microstrip or patch antennas and their types of feed configurations. This chapter concludes with a presentation of several state-of-the-art wideband CP patch antennas. The antennas presented are assessed against all requirements listed in Section 2.3.8 including performance, size, and ability to be integrated into an array configuration.

2.2 Antenna Theory

2.2.1 Foundations of Antennas

Antennas serve as electromagnetic (EM) transducers, converting guided waves, with a wavelength of λ_g within a transmission line into EM waves that travel through an unbounded

medium, typically free space, with a wavelength of λ_0 and vice versa [10]. For the purposes of this thesis, the focus will be on antenna reception. As the name may suggest, EM waves are composed of electric and magnetic fields, both synchronized and orthogonal to each other. Assuming a linear, isotropic homogeneous region, these fields can be represented by the Hemholtz equations for $\mathbf{E}$ and $\mathbf{H}$ also known as the plane wave equations [11], the general solutions are

$$\nabla^2\mathbf{E} + \beta^2\mathbf{E} = \frac{1}{\epsilon}\nabla q_{ve} + \nabla \times \mathbf{M_i} + j\omega\mu\mathbf{J_i} \tag{2.1}$$

$$\nabla^2\mathbf{H} + \beta^2\mathbf{H} = \frac{1}{\mu}\nabla q_{vm} - \nabla \times \mathbf{J_i} + j\omega\mu\mathbf{M_i} \tag{2.2}$$

where $\mathbf{E}$ is the electric field, $\mathbf{M_i}$ is the impressed magnetic current density, $\mathbf{J_i}$ is the impressed electric current density, q_{ve} and q_{vm} represent the electric and magnetic current density. Furthermore, these two wave equations are also a function of the wave number or propagation constant $\beta = \omega\sqrt{\mu\epsilon}$ which itself is a function of frequency, ω, in rad/s, as well as the permeability, μ, and permittivity, ϵ, of the medium the wave is travelling through. The scale and performance of an antenna is directly related to the properties of the antenna as well as the frequency of operation, f_0. These ideas will be further expanded upon later in this section.

In addition to the permittivity of a material, is its loss tangent $\tan\delta$. This is an indicator that quantifies a dielectric material's inherent dissipation of EM energy and is

$$\tan\delta = \frac{\omega\epsilon'' + \sigma}{\omega\epsilon'} \tag{2.3}$$

where $\omega\epsilon''$ is the dielectric damping, σ is the conductivity of a material and $\epsilon' = \epsilon_r\epsilon_0$ where ϵ_0 is the permittivity of free space. This can also be described as the ratio between the lossy reaction to an electric field to a lossless reaction [11]. Good insulators are materials with a low $\tan\delta$ and are preferred to minimize dielectric losses and maximize radiation efficiency as discussed later on in this section. In fact, a medium with a $\tan\delta < .01$, is said to be a good insulator [12].

2.2.1.1 Radiation Intensity

All discussion of antenna characterization stems from power density. This can be mathematically shown in (2.4) where the power radiated or average power of the system is equal to the time-averaged Poynting Vector, $\mathbf{W_{rad}}$, integrated over a closed surface. The Poynting Vector is also described as one-half the real part of the cross-product of the complex orthogonal electric and magnetic fields, associated with an EM wave uniformly distributed over a sphere, as a function of frequency.

$$P_{rad} = P_{av} = \oiint_s \mathbf{W_{rad}} \cdot \mathrm{d}\mathbf{s} = \frac{1}{2} \oiint_s \mathrm{Re}(\mathbf{E} \times \mathbf{H}^*) \cdot \mathrm{d}\mathbf{s} \tag{2.4}$$

$$P_{rad} = \oiint_\Omega U \, \mathrm{d}\Omega = \int_0^{2\pi} \int_0^{\pi} U \sin\theta \, \mathrm{d}\theta \, \mathrm{d}\phi \tag{2.5}$$

However, for EM radiation we are interested in both the magnitude and the direction of how an antenna emits radiation. This is done by analyzing the radiation around the antenna per unit solid angle $\mathrm{d}\Omega$ or $\sin\theta \, \mathrm{d}\theta \, \mathrm{d}\phi$, where ϕ is the angle in the azimuthal plane and θ the angle in the elevation plane at a fixed distance r [13] as shown in Fig. 2.2. This is referred to as radiation intensity U as described in (2.5). Each solid angle corresponds to a region of a surface of a sphere that of radius r. If the radius is large enough, the radiation is essentially independent of the r. Multiplying the radiation density by the square of a fixed r, results in radiation intensity $U = r^2 W_{\mathrm{rad}}$. The total power radiated from an antenna can be found by multiplying the radiation intensity per unit solid angle by 4π.

2.2.1.2 Radiation Pattern

A radiation pattern represents the transmission or reception of the radiation intensity of an antenna and is a function of both the elevation and azimuthal angles $U(\theta, \phi)$. These radiation patterns also provide information regarding the performance of an antenna which fundamentally includes the direction and magnitude of the ratio of radiation intensity in any direction to that of the maximum radiation intensity. Although radiation patterns are three-dimensional in nature, it is a generally accepted practice to illustrate these radiation

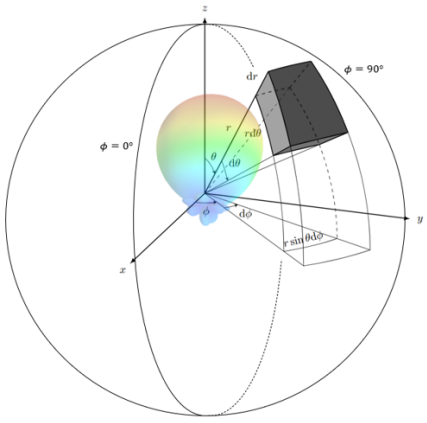

Figure 2.2: Coordinate system for antenna analysis

patterns in terms of its two principal planes, $\phi = 0°$ and $\phi = 90°$ as shown in Fig. 2.2 [13]. An illustration of a radiation pattern in both these radiation cuts can be found in Fig. 2.3 with the numbers on the left of the figure indicating the power relative to that at maximum in dB.

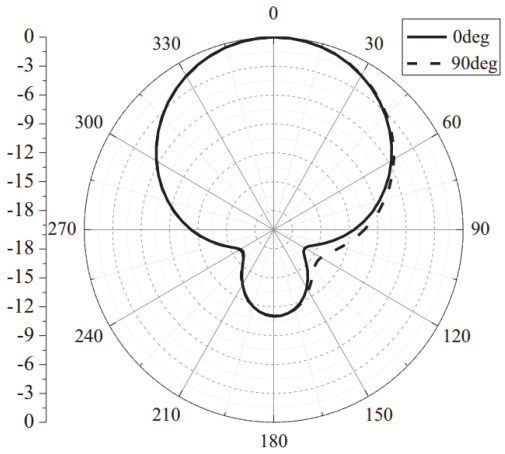

Figure 2.3: Antenna radiation pattern [14].

2.2.1.3 Field Zones

As noted earlier, the radiation pattern of an antenna is assumed to be taken far enough away that the radiation is independent of radial distance. This occurs in the far-field or

Fraunhofer zone. This is because the radial component of a travelling wave is small and is neglected from radiation calculations. In fact, there are three regions of an antenna, the reactive near-field region, the radiation near-field region and the far-field region. For this thesis, the analysis, simulation and testing of all far field parameters such as Gain and AR, will be conducted in the far field. For this to be valid, all the data collected regarding the radiation characteristics of the antenna must be a minimum distance of $2D^2/\lambda$ from the antenna, where D is the longest dimension of the antenna and λ is the operating wavelength [15].

2.3 Antenna Performance Specifications

Prior to assessing the performance of the antennas in this work and others, it is important to understand the specifications that are key to antenna design. There are various parameters that contribute to antenna performance but for brevity this section will cover the following main parameters or figures of merit (FOM): gain, half-power beamwidth (HPBW), AR, $|S_{11}|$ and consequently ARBW, IBW, gain bandwidth (GBW), axial ratio beamwidth, and front-to-back ratio (FBR).

2.3.1 Directivity and Gain

As discussed in Section 2.2.1.2, the radiation pattern defines the magnitude and direction of the radiation emitted by an antenna. Furthermore, directivity, is defined as "the ratio of the radiation intensity in a given direction from the antenna to the radiation intensity averaged over all directions" [15]. If a pattern is shaped such that the radiation intensity is focused in a certain direction or directions, this describes the directional capability of an antenna and is measured by directivity which is detailed in (2.6) where D is directivity and P_{rad} is the radiated power of an antenna.

$$D = \frac{4\pi U(\theta, \phi)}{P_{\text{rad}}} \tag{2.6}$$

Gain, G, is often used in place of directivity to describe the directional capability of an

antenna. As detailed in (2.7), gain is a function of the accepted power radiated isotropically, P_{in}, which takes into account dielectric and conductive losses in the antenna as well as antenna mismatch. Equivalently, the gain of the antenna is simply the directivity of the antenna multiplied by e_{cd} which represent the antenna dielectric and conductive losses. As the area of interest in this thesis is for CP antennas, the gain is measured in decibels isotropic (dBi) for linear antennas or decibels isotropic circularly polarized (dBic) for CP antennas. These are used to describe the gain of an antenna relative to an antenna radiating isotropically. Unless specified, the gain of an antenna is generally referred to that simulated or measured at boresight $\theta = \phi = 0°$. Finally, consistent gain as a function of frequency is a sign of a state-of-the-art antenna and is denoted by a maximum of a 3 dB drop in gain within the band of interest.

$$G = \frac{4\pi U(\theta, \phi)}{P_{\text{in}}} = e_{\text{cd}} D \tag{2.7}$$

2.3.2 Half-Power Beamwidth

HPBW is defined as "in a plane containing the direction of the maximum of a beam, the angle between the two directions in which the radiation intensity is one-half of the beam" [15]. As radiation plots are normally expressed in dB, the HPBW refers to the point where the radiation pattern drops by a factor of -3 dB from maximum. For reference, the HPBW of the pattern in Fig. 2.3 would be approximately 60°. For GNSS applications, a wide beamwidth is required to capture multiple satellites at several different elevation angles. The standard GNSS antenna requirements call for an HPBW of $100° - 140°$ for terrestrial applications [8]. If the HPBW $< 100°$ then the antenna and therefore the receiver, are not as likely to capture the four (4) satellites needed for accurate positioning, navigation, and timing (PNT) [16]. Conversely, at angles greater than 140°, the antenna is subject to increasing interference, noise and multi-path near the antenna horizon [9].

2.3.3 Front-to-Back Ratio

FBR is an additional quantitative measure of a radiation pattern. The FBR defines the ratio of the main lobe, or radiation emitted in the intended direction with the radiation that is emitted at the rear of an antenna, also known as the back lobe of a radiation pattern. FBR marks the difference in magnitude (dB) of these two radiation intensities. An FBR $>$ 10 dB is considered an acceptable value. For reference, the FBR found in Fig. 2.3 is approximately 11 dB.

2.3.4 Reflection Coefficient

The standard used to describe the characteristics of the input impedance of an antenna is with $|S_{11}|$. This parameter describes the ratio of the incident voltage in comparison to the reflected voltage at the input port of the antenna. For a receiving antenna, the more voltage that is available to be delivered to the load in this case a receiver input, the more likely the signals from a source will be delivered to the receiver by way of the antenna. An $|S_{11}| < -10$ dB is the minimum standard for an antenna to be considered impedance matched to its receiver [13].

2.3.5 Polarization and Axial Ratio

Strictly by definition, a uniform plane wave polarization can be illustrated by a curve that is traced by the tip of a resultant electric field vector that is always orthogonal to the direction of propagation as a function of time and at a specified location [10]. The polarization of a wave is determined by the magnitude of its two resultant components. There are several polarization states including linear, elliptical, and circular as shown in Fig. 2.4.

CP is a degenerate polarization state where the two electric vectors components, in this example, E_y and E_x, are equal in magnitude and have an odd-multiple 90° difference as shown in the bottom left and top right states in Fig. 2.4. The sense of the polarization, whether it is RHCP, or left hand circularly polarized (LHCP) is dependent upon the time-phase lag between the electric field components and assumes wave propagation is occurring

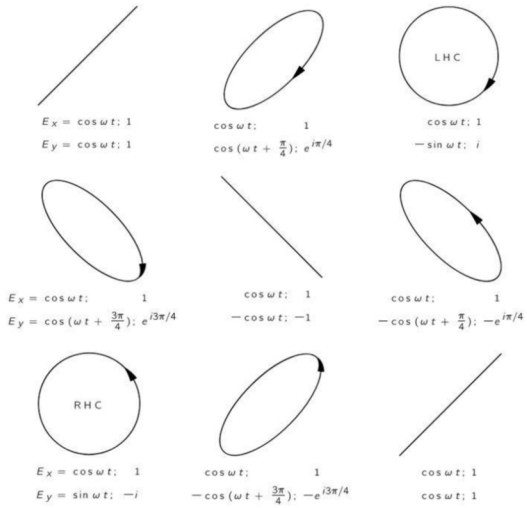

Figure 2.4: Illustration of polarization states [17].

in the $+z$ direction or out of the page. Then, if the time-phase difference between E_y and E_x is $-90°$ the wave is RHCP. Conversely, if the time-phase difference between E_y and E_x is 90° the wave would be LHCP [10].

AR is an indication of CP purity and is mathematically described in (2.8) where OA and OB are the major and minor axes of an ellipse. An AR = 0 dB indicates perfect CP where an AR $<$ 3 dB is considered the acceptable value for CP applications [8]. Furthermore, CP antennas can capture CP signals regardless of their orientation in relation to the orientation of the transmitted signal assuming the sense of CP is matched (i.e. both signal and antenna are RHCP or LHCP) and that the antenna is designed to receive the frequency or frequencies of interest. Finally, antennas with poor AR could result in reducing the ability of the receiver to acquire a GNSS lock by up to 50% particularly in metropolitan areas [9].

$$\mathrm{AR} = 20 \log \left(\frac{|\mathbf{OA}|}{|\mathbf{OB}|} \right) \tag{2.8}$$

2.3.6 Bandwidth

IEEE defines antenna bandwidth as "the range of frequencies within which the performance of the antenna, with respect to some characteristic, conforms to a specified standard" [15]. For

the performance of an antenna including those in this work, the bandwidth will serve as one of the keys to understanding antenna performance against specified criteria. It is common practice for antenna designers to publish their results in fractional bandwidth (FBW) as shown in (2.9), where f_h and f_l are the highest and lowest frequencies of the band in question. For the GNSS L-band, a bandwidth of greater than 30% [9] is considered wideband. For reference, the GNSS L-band is approximately 32.5% so the antenna must effectively cover the whole band to be considered a wideband device.

$$\text{FBW} = \frac{2(f_h - f_l)}{f_h - f_l} \tag{2.9}$$

Although there are numerous parameters in which bandwidth performance is measured, there will only be three that will be the focus of this paper. First, IBW denotes the range of frequencies in which the reflection coefficient $|S_{11}| < -10$ dB. Next, ARBW is the frequency band where the AR < 3 dB. Finally, GBW is the continuous range of frequencies where the gain is above a minimum specified value and is ≥ -3 dB of the maximum gain within the band of interest.

2.3.7 Physical Size

The size of an antenna affects its versatility and application. Generally, the smaller the antenna the more versatile it is including the ability to be integrated into an antenna array. However, there are limitations to reducing the size of an antenna such as impedance matching and antenna efficiency. There will be more discussion on physical size requirements for antenna elements in an array configuration later on in this chapter. Nonetheless, for antenna designers, an antenna that is comparable to or more compact in size to contemporary designs is the mark of a state-of-the-art device.

2.3.8 GNSS Antenna Performance Requirements

For wideband GNSS applications, both fundamental antenna design and specific GNSS specifications are required to be met. They are as follows and are applicable within the GNSS

L-band:

- RHCP Gain ≥ -10 dBic. This is minimum gain ($G_{\min}$) required to provide adequate signal-to-noise ratio for detection [8] within the band of interest.
- Maximum 3 dB Gain drop as a function of frequency. Although not a core GNSS specification, this metric denotes Gain stability and is a trait of state-of-the-art antenna designs [18]. The first two specifications listed comprise the GBW of the antenna.
- FBW $\geq 30\%$. A bandwidth of greater than 30% is considered wideband, this includes IBW, ARBW, and GBW [9].
- HPBW: $100^\circ \leq \theta \leq 140^\circ$. For GNSS applications, a wide beamwidth is required to capture multiple satellites at several different elevation angles (θ) [8].
- Long Planar Dimension < 120 mm. Most compact GNSS devices have their longest dimension < 120 mm, otherwise it is considered large [19].
- Antenna height $h < 10$ mm. As will be discussed in the literature survey, compact state-of-the-art GNSS antennas are generally less than 10 mm in height.

2.4 Antenna Feed Networks

The feed network of an antenna is composed of a transmission line system that bridges an input port, usually a receiver input with a 50 Ω impedance, with an output or outputs exciting an antenna radiating aperture. The performance of the feed network has a large effect on the antenna performance including polarization, impedance matching and radiation features. However, there is a trade-off between system performance, size and complexity. This section will cover their performance parameters, with some feed network examples.

There are many feed networks that have been researched, yet, for the purposes of this thesis the focus will be wideband feed networks that are part of the design of some wideband antennas. This will be specific to multi-port feed networks, with one input and two or more outputs.

2.4.1 Feed Network Parameters and Figures of Merit

There are three aspects that are needed for a well-designed feed network, impedance matching, power imbalance and phase imbalance. These describe the overall performance of a feed network and are key to the optimal operation of an antenna. Note these metrics, especially those regarding phase and power imbalance, are only applicable to a feed network with multiple ports.

2.4.1.1 Impedance Matching

The impedance matching of a feed network ensures that radiating aperture is matched with the input impedance seen at a receiver input. If the feed network is not well impedance matched, then neither will the antenna. Furthermore, feed network impedance matching is measured the same as an antenna. However, for the antenna to have a $|S_{11}|$ of a certain bandwidth, the feed network needs to have a larger bandwidth than the antenna to account for any mismatch that may occur between the feed network and radiating aperture. Additionally, although not directly related to antenna design, for some couplers, power dividers and phase shifters that would comprise of a wideband feed network, the reflection coefficient standard minimum value is disclosed as $|S_{11}| < -15$ dB [4][20]. Ultimately, this could account for some mismatch between the feed network and radiating aperture, thus ensuring that the overall antenna impedance matching level is $|S_{11}| < -10$ dB.

2.4.1.2 Phase Shift and Phase Imbalance

The following two feed network performance requirements are with respect to CP. As stated previously, there is an assumption that the components of a travelling electric wave were 90° out-of-phase so that the resultant electric field trace would rotate in a circle as viewed from the direction of travel. This implies that the phase between two adjacent output ports needs to be orthogonal and stable throughout the band of interest. Still, it is a challenge to design a stable phase shift over a wide range of frequencies due to the complexities inherent in a feed network utilizing phase shifters. A $90 \pm 5°$ phase imbalance [4] is considered the maximum differential phase between two output ports, and is noted by the difference in phase between

the forward transmission and reverse transmission coefficients, $\angle S_{21} - \angle S_{31}$. There is no published quantitative comparison between phase imbalance and AR, however, it is inferred by [9], with an antenna feed network achieving a maximum phase imbalance of $90 \pm 5°$, that minimizing the phase difference between ports is necessary for best AR performance.

2.4.1.3 Power Division and Power Imbalance

CP requires the components of the travelling electrical field wave be as close in magnitude as possible such that an antenna AR < 3 dB. For example, a dual-fed antenna requires two lines feeding the radiating aperture and the amplitude at each output port be one-half that at the input. This is measured as the difference in amplitude between two output ports, the magnitude of the forward transmission and reverse transmission coefficients, $|S_{21}| - |S_{31}|$, and should not be greater than 1 dB. This scenario would require -3 ± 0.5 dB or a maximum of 1 dB power imbalance between two output ports [20]. Similar to phase imbalance, there is no specified link between power imbalance and AR, however, minimizing power imbalance is expected to minimize AR [9].

2.4.1.4 Bandwidth

The bandwidth of a feed network must be greater than or equal to that of the overall antenna as it largely determines the performance of the antenna. The difference are the parameters that are being measured. There are three bandwidth parameters, IBW, phase imbalance bandwidth, and power imbalance bandwidth that will be identified as critical to both the operation of the feed network and overall antenna design. IBW for a feed network is measured the same as the antenna except where the reflection coefficient $|S_{11}| < -15$ dB over the band of operation. The phase and power imbalance bandwidths between two adjacent output ports are $90 \pm 5°$ and 1 dB power imbalance, respectively, over the band in question.

2.5 Wideband Feed Networks

As will be discussed later in this chapter, some antennas such as patch antennas, are inherently narrowband. Any small deviation from their resonance results in a significant decrease

in antenna performance. Due to this limitation, single feeds are not capable of generating wideband performance unless, for example, when both electric and magnetic sources exist within the radiating aperture [18]. Instead, a multi-feed approach, where two or more feeds are used to drive the radiating aperture of an antenna will be explored in this thesis. At the core of their design, feed networks require stable power division and 90° phase shift over the entirety of the band of interest. What follows are some examples of wideband feed networks.

2.5.1 90° Wideband Power Dividing Phase Shift Network

This wideband circuit is comprised of two stages, the power division stage and a 90° differential phase shift stage. The Wilkinson power divider (WPD), shown in Fig. 2.5(a), is a popular power divider design due to its ease of analysis and implementation. It is composed of two-quarter-wave transformers (QWTs) that branch out from an input port of characteristic impedance, Z_0, usually 50 Ω connected to two output ports of the same characteristic impedance. This design requires an impedance of value $2Z_0$, generally 100 Ω resistor, between the two output ports for isolation and matching purposes. T-junctions are also used for equal power dividers where the input of characteristic impedance Z_0 forms a "T" with a line having two output ports, both with an impedance of $2Z_0$. It is commonly used in arrays due to its compact size, however, it may suffer from poor isolation between the two output ports [11].

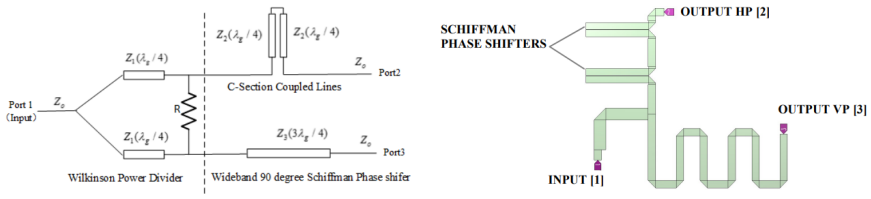

Figure 2.5: 90° Wideband Power Dividing Phase Shift Network (a) WPD and phase shifter [21] (b) T-junction and Schiffman phase shifter [22].

The second stage provides the 90° phase shift. The key to this stage is that the phase of one of the output ports leads the other by 90° and needs to be stable over a wide range of frequencies. According to the examples in Fig. 2.5 taken from GNSS antenna designs,

port 2 needs to lead port 3 by 90°, necessary for CP operation. One of the output ports, for CP applications, requires a dedicated phase shifter that uses some form of filter design such as open and short matching stubs or Schiffman phase shifters in Fig. 2.5(a) and (b). The transmission line connected to the remaining port must be physically $\lambda_g/4$ or electrically 90° longer than the port with the phase shifter. It is possible that additional stages of phase shifters may be required to increase the phase imbalance bandwidth of the system. In fact, the researchers at [22] used two Schiffman phase shifters in series after discovering that the bandwidth of a single phase shifter was too narrow. Nonetheless, performance of these broadband circuits comes at a cost, size. According to the Fig. 2.5(a), port 2 transmission line requires a total length of at least $3\lambda_g/4$ and correspondingly, port 3 transmission line requires a total length of at least λ_g. For GNSS applications this can be a significant length, especially if several stages of phase shifters are required. Therefore, the use of meandering, single-coupled or artificial transmission lines (ATLs) may prove necessary to ensure a compact design.

2.5.2 Branchline Coupler

A BLC, also known as a hybrid coupler or quadrature hybrid, is a device that combines the power division and phase shift capabilities found in the two stages of the 90° Wideband Power Dividing Phase Shift Network. At its core, a BLC is designed to couple a specific amount of EM power to a particular port so that multiple outputs can be driven from a single input [11]. Unlike the Power Dividing Phase Shift Network, the BLC, as shown in Fig. 2.6(a), has four ports: the input port (port 1), the through port (port 2), the coupled port (port 3) and the isolated port (port 4) with four QWTs between adjacent ports. This configuration supports equal power division between the two output ports 2 and 3, where the amplitude is ideally $|S_{21}| = |S_{31}| = -3$ dB in reference to the input port. In addition, the phase between the two output ports, $\angle S_{21} - \angle S_{31} = 90^\circ$ out-of-phase. The isolated port is terminated with a matched load [11], normally a 50 Ω resistor.

A single stage BLC has good performance with an IBW of $10 - 20\%$ [11], however, this is not suitable for driving a wideband GNSS antenna. One way to improve the performance

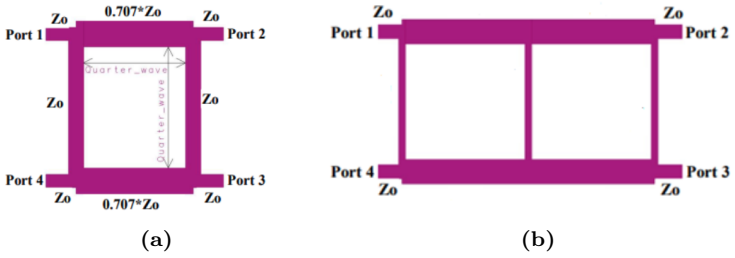

Figure 2.6: Branchline coupler (a) Single-stage (b) Two-stage [23].

is to add stages, like that in Fig. 2.6(b). This two-stage BLC has improved bandwidth up to 50% including IBW, power and phase imbalance bandwidths [4][20][23]. Although this device can be designed to provide unequal amplitude division and impedance transformation between the input and output ports, for the purposes of this work, it will only be considered using equal power division and no impedance transformation.

Nevertheless, there is an obvious trade-off with the use of a two-stage BLC. It is approximately twice as large as the single-stage BLC with dimensions of $\lambda_g/4 \times \lambda_g/2$ which is comparable in size to a radiating aperture such as a rectangular patch if it were etched on a substrate of similar properties. As such, considerable research has gone into decreasing the size of a two-section BLC using techniques such as high or double-high permittivity materials, ATLs or single-coupled-lines [4][20][24]. Ultimately, this has been found to be critical to achieving compact antennas with wideband performance.

2.5.3 Single-Coupled-Lines

Single-coupled-lines are commonly used in phase shifters as they provide a stable phase shift response and are a method to reduce the size of a microwave circuit. These two-port devices are designed to be all-pass filters with even- and odd-mode impedances, Z_{0e} and Z_{0o}, and electrical length, θ that can approximate a conventional transmission line of impedance Z_c and length θ_c as illustrated in Fig. 2.7. If a two-port network has an impedance at input port 1, Z_{i1} and its output port 2 terminated with an impedance of Z_{i2} and concurrently, if the output impedance is Z_{i2}, with its input terminated with an impedance, Z_{i1}, then Z_{i1} and Z_{i2} are defined as image impedances [11]. Single-coupled-lines shorted at one end have

an all-pass filter response with an image impedance described at (2.10) and is only valid if the electrical length of the coupled section is $0 \leq \theta \leq \pi$. The crucial characteristic in this circuit is that the phase of a transmitted signal is adjusted as a function of frequency to account for phase variation in the greater transmission line system [11], enabling stable phase shift operation over a wide range of frequencies. Single-coupled-lines can reduce the realized transmission line such as a microstrip line trace with similar performance to that of a conventional transmission line but are not as simple to analytically model since the use of even- and odd-mode impedances are required as part of their circuit model.

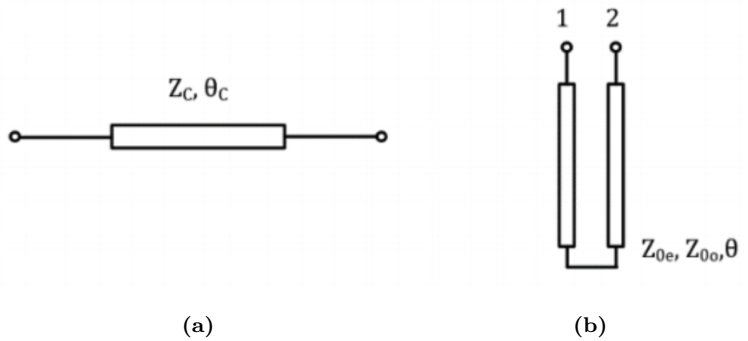

Figure 2.7: Transmission Lines (a) Conventional (b) Single-Coupled-Line [4].

$$Z_{il} = Z_{i2} = \sqrt{Z_{0e} Z_{0o}} \tag{2.10}$$

2.6 Printed Circuit Board Technology

GNSS patch antennas are generally composed of PCB technology including core laminates with electroplated conductive elements that can be designed to serve as ground planes, microstrip transmission lines and resonant patches. Depending on the application, this may also include surface mounted devices such as resistors and phase shifters. What is less commonly found in GNSS patch antennas are vias and striplines. Vias are electroplated drilled holes and are the physical and electrical connections between different layers of a PCB stack-up [25]. Striplines are conductive traces that exist between two ground planes. As will become clear later, for aperture-coupled patch antennas, these devices provide the

opportunity to reduce the size of an antenna by feeding the slots in the same physical area as the rest of a feed network but at different layers. Also, it is necessary to determine how additional ground planes will affect the radiation pattern of an antenna, especially aperture-coupled patch designs.

There are some challenges when using vias and striplines. First, vias introduce sharp vertical transitions that incur a parasitic capacitance and parasitic series inductance that have a significant impact on the impedance of a via. These changes can lead to impedance mismatching that can decrease the performance of a transmission line and antenna [25]. Second, introducing multiple layers with microstrip lines, striplines and vias will increase the complexity and cost of the antenna. And as will be seen, if there is a microstrip layer and stripline layer that are concurrently used in a PCB design, then a microstrip-to-stripline transition is required.

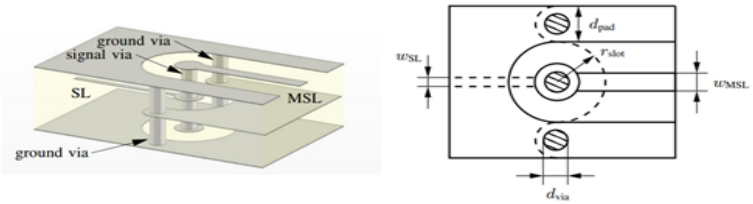

Figure 2.8: Microstrip-to-stripline coplanar waveguide transition a) 3D view b) 2D top view [26]

2.7 Signal, Shielding and Stitching Vias

Vias have several uses within a PCB, including signal, shielding and stitching vias. First, signal vias serve as the interconnection between transmission lines that exist on different layers of a PCB. There are three separate components of a signal via, the via-hole, via-pad and anti-pad. The via-hole is the center cylinder shown in Fig. 2.8(a) and carries the signal between traces on different layers. The common radius for a signal via noted as d_{via} in Fig. 2.8(b) is between 0.6 mm $-$ 1.0mm with the smallest holes being around 0.3 mm [25][26], though they should be minimized to achieve optimal performance.

These via-holes are connected to a line trace with the use of via-pad or annular ring that

surrounds the via-hole as shown in Fig. 2.8(a). Vias require a minimum amount of conductive material to establish a connection with a transmission line trace during fabrication. These via-pads also provide impedance matching between the copper traces and the via-holes. Furthermore, according to [25][26], d_{pad} in Fig. 2.8(b) should also be made as small as possible and should be approximately twice of size of d_{via} for optimum performance.

Furthermore, the anti-pad is a void annulus area around a signal via where no conductor can exist as shown in 2.8(a). This provides insulation from surrounding conductors to ensure that there is no interference or unintentional return path that could be created with adjacent circuits. There have been several anti-pad sizes that have been quoted in literature, with the consensus that the anti-pad radius, r_{slot} in Fig. 2.8(b) should be anywhere from 2-3 times larger than that of the d_{pad} for best results [25][26].

Finally stitching vias, as indicated by via #2 in Fig. 1.1 on page 4, are introduced between a PCB utilizing multiple ground planes [27]. Their function is to mitigate the effects of parallel-plate mode coupling. The parallel-plate mode of operation is of most concern with stripline designs. The fundamental mode of a parallel plate waveguide exhibits no field-variation in the transverse (orthogonal) direction of transmission. This results in a uniform electric field between the top and bottom plates sandwiching a stripline trace, allowing propagation down to direct current (DC). To prevent excitation of the parallel-plate mode, it is essential that both ground planes are at the same potential. This is achieved by periodically shorting the two ground planes together using stitching vias [27].

2.8 Microstrip-to-Stripline Transition

Blind vias connect an exterior layer or microstrip trace to an interior layer or stripline trace. They are also known as a microstrip-to-stripline transition and are a critical point of impedance matching. As illustrated in Fig. 2.9, signal vias and shielding vias in the transition can be modeled as an equivalent coaxial cable model. In this electrical model, the shunt capacitance C and series inductance L detailed in (2.11) and (2.12) respectively, where d is the diameter of the signal via, D is the inner diameter between shielding vias, h is the

height of the substrate μ_0 is the permeability of free space, μ_r is the relative permeability of the conducting material [11]. Finally, there are resistive losses, R, from the signal via and the shunt conductance, G, due to the dielectric losses in the substrate [11]. This transition can be modeled as a two-port matching network where two transmission lines, modeled as Z_1, θ_1 and Z_2, θ_2 are the microstrip and stripline traces respectively [6].

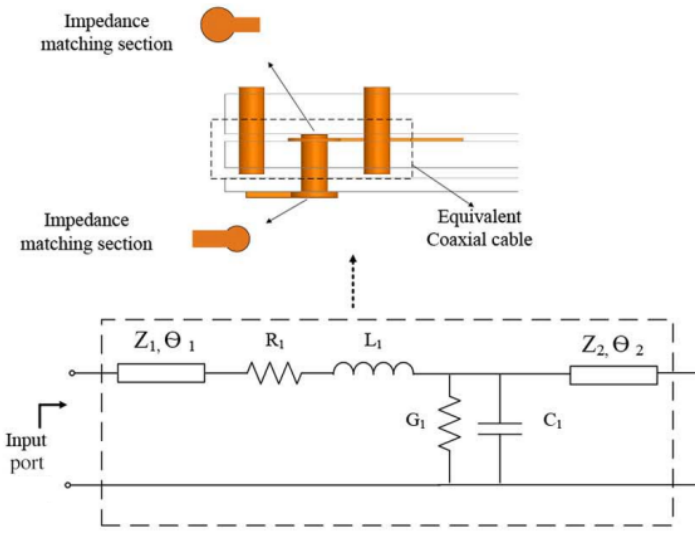

Figure 2.9: Microstrip-to-stripline transition electrical model [6].

$$C = 2\pi h \epsilon_0 \epsilon_r \ln\left(\frac{D}{d}\right) \tag{2.11}$$

$$L = h\mu_0\mu_r 2\pi \ln\left(\frac{D}{d}\right) \tag{2.12}$$

2.9 Antenna Array Fundamentals

All the requirements and parameters discussed to this point have been regarding a single, standalone antenna. In general, the performance of such a device is defined as having a radiation pattern with a wide HPBW, and low gain. There are some instances where there may be a need for higher gain and narrower beamwidth. Two primary solutions to address this issue would be to increase the size of a standalone antenna or construct a device using

multiple antenna elements in an array. It may be tempting to simply increase the size of the antenna but this could lead to large devices that may not be practical in many applications. In addition, arrays can further be integrated into a phased array configuration where a beam-steering capability or the ability to change the direction of the main lobe of a radiation pattern to a desired location can be achieved. This would be a valuable feature especially for SOTM communications or in EW applications.

Electric or magnetic fields from a source such as an antenna can, through superposition, be added to one another resulting in a net field at a specific point in space. When analyzing EM fields from multiple sources using this approach, it also leads to both constructive and destructive interference. Achieving a high gain in an array design requires constructive interference occurring in the desired direction.

Antenna array patterns can be shaped in five primary ways: the geometric layout of individual radiators, the spacing between antennas, the phase at each radiator, the excitation amplitude of each element, and the relative pattern of individual antennas [13]. For the purposes of this thesis, the discussion of antenna arrays will be limited to changes in the layout and the spacing between antennas specifically, with only uniform spacing between all radiator elements.

2.9.1 Linear Arrays

The simplest and most practical way to form an array is to place identical source elements in a line like that in Fig. 2.10 where θ is the observation angle in the elevation plane and the distances between the elements are denoted by d_0, d_1, d_n, etc. By placing two or more antenna elements together in a line, the total field now becomes the multiplication of the individual antenna pattern and its array factor (AF). This process, which is defined as pattern multiplication, described at (2.13), is the fundamental principle in antenna array design. The AF is defined as the radiation of an isotropic radiator as it does not depend on the directional characteristics of an antenna element [13].

$$\mathbf{E}_{\text{Total}} = [\mathbf{E}_{\text{Single Element}}] \times [\text{AF}] \tag{2.13}$$

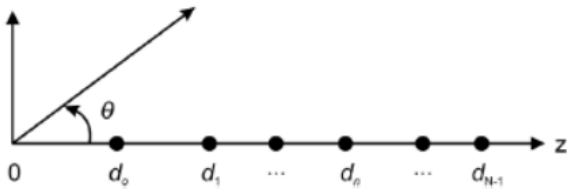

Figure 2.10: Illustration of linear array [28].

$$\text{AF} = \sum_{n=0}^{N-1} I_n e^{j\beta d_n \cos\theta} \tag{2.14}$$

The array factor is detailed at (2.14) where I_n is the amplitude at each element, wavenumber $\beta = 2\pi/\lambda$, and θ which again is the reference angle of the observation point [28]. One of the critical parameters of AF that affect the performance of an antenna is the distance between elements or inter-element spacing, d_n. With the distance between elements small, an antenna array behaves like a large antenna of roughly equivalent size. However, as the distance increases, the array starts to act like a group of individual antenna elements. This can result in multiple radiation pattern maxima such as back and grating lobes. The introduction of these additional maxima reduces the overall radiation that is available in the intended direction of propagation. To avoid these unwanted features, the inter-element spacing between elements must be $< \lambda_0/2$ [13].

The required element spacing restriction can be illustrated using a 10-element uniform amplitude linear array in Fig. 2.11 which describes the radiation pattern as a function of the elevation angle θ. For most antenna applications, including satellite communications, the radiation pattern is intended to have only one radiation maxima to maximize the gain of the antenna. When $d_n = \lambda_0/4$, the radiation pattern has only one maxima at 0°. However, when $d_n = \lambda_0/2$, now a back lobe exists as an additional pattern maxima. The power radiated in the direction of propagation would be significantly less as a result, leading to undesirable performance. If the distance between elements was increased further to $d_n = \lambda_0$, two additional maximum would be introduced at $-90°$ and 90°, where these are known as grating lobes resulting in even less radiation in the intended direction of emission.

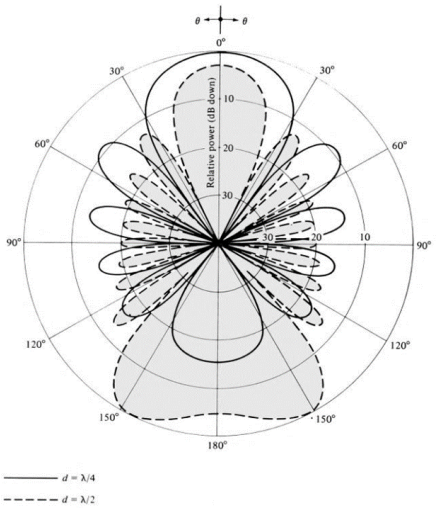

Figure 2.11: Array factor pattern of a 10-element uniform amplitude Hansen-Woodyard end-fire array ($N = 10$, $\beta = -(kd + \pi/N)$, exhibiting a back lobe [13].

2.9.2 Planar Arrays

A planar array is the two-dimensional extension of the linear array, illustrated in Fig. 2.12. In this model, the AF of planar elements can be considered as an array of one dimensional arrays. An AF of a rectangular planar array can be determined by finding the AF along one of the planar axes, and then use that AF to evaluate the AF along the remaining axis to establish the total AF, described mathematically as

$$\text{AF} = I_{nm} \sum_{n=1}^{N} e^{j(n-1)\psi_x} \sum_{m=1}^{M} e^{j(m-1)\psi_y} \tag{2.15a}$$

$$\psi_x = kd_x \sin\theta \cos\phi + \beta_x \tag{2.15b}$$

$$\psi_y = kd_y \sin\theta \sin\phi + \beta_y \tag{2.15c}$$

where I_{nm} is the weight factor for the element in question (n,m), ψ_x and ψ_y are the progressive phase in the x and y directions, β_x and β_y are the phase between elements, and d_x and d_y are the inter-element spacing on the x- and y-axes respectively [13]. Factors such as inter-element spacing remain applicable even in a planar array configuration. The

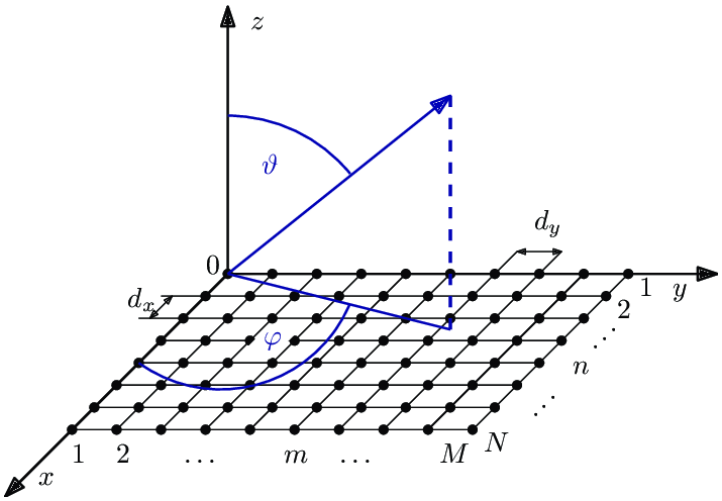

Figure 2.12: An N x M element planar antenna array configuration [29].

minimum dimension of each axis that can exist in the planar array is $d_x = d_y < \lambda_0/2$ to avoid any additional pattern maxima. Therefore, the largest element area that each element can occupy is $< \lambda_0^2/4$.

2.9.3 Phased Arrays

One of the key benefits of antenna arrays, in addition to enhanced gain, is the capacity to control the direction of EM energy. In some cases, there is a need for the direction of the array maxima to be fixed, while in others, the pattern maxima needs to be dynamically adjusted while the array is in operation. This directional control is achieved by altering the AF, typically by adjusting the phase β at each radiating element. This changes how the EM fields combine, either reinforcing or canceling each other, consequently reshaping the overall pattern of the array. These phase shifters are commonly implemented through the use of semiconductor devices, thin film ferro-electric materials, micro-electro-mechanical systems (MEMS), slow-wave or periodically loaded transmission lines, ferrite or ferrimagnetic materials or digitally [28].

2.9.4 Mutual Coupling

When antennas are in proximity to each other, where any combination of them are in transmit or receive mode, some of the energy that is primarily intended for one ends up at another. As such, each antenna behaves like a secondary transmitter rescattering energy in different directions. This process is known as mutual coupling. This can depend on the radiation characteristics of each device, their relative separation and orientation. Mutual coupling complicates the conventional approach to antenna array analysis, typically oversimplified by analyzing the individual element pattern and the AF separately, then combining them together through pattern multiplication. So, to gain a comprehensive understanding of the underlying physics, it is essential to adopt a more nuanced perspective that accounts for the scattering and coupling phenomena within the antenna array and its feed network.

Although mutual coupling has three components [30] including coupling inside the antenna array feed network, interactions between an antenna and nearby objects, it is the third component, radiation coupling between two nearby antenna elements, that will be discussed in this section, presenting an introduction to mutual coupling in antenna arrays. It is regarded as the final step needed to design a realistic phased array antenna [30].

2.9.4.1 Active Impedance in Antenna Arrays

For mutual coupling, it is important to discuss an example of the process of coupling between two antenna elements, 1 and 2, placed in an array as shown in Fig. 2.13. Assuming they were perfectly matched to their feed networks with load impedance z, the return signals of antenna element 1, V_1^-, should ideally be zero, such as the case in Fig. 2.13(a). However, in reference to Fig. 2.13(b), as an incident plane wave strikes antenna element 2, part of the wave will continue into the feed network, part will be rescattered into space, and some of the energy will be directed toward antenna element 1, where it will add vectorially with the incident wave.

For antenna element 1, this causes a signal moving from the antenna to the transmission line such that $V_1^- \neq 0$. This new condition has a mismatch between the antenna and its transmission line where the reflection coefficient is now non-zero. This interaction directly af-

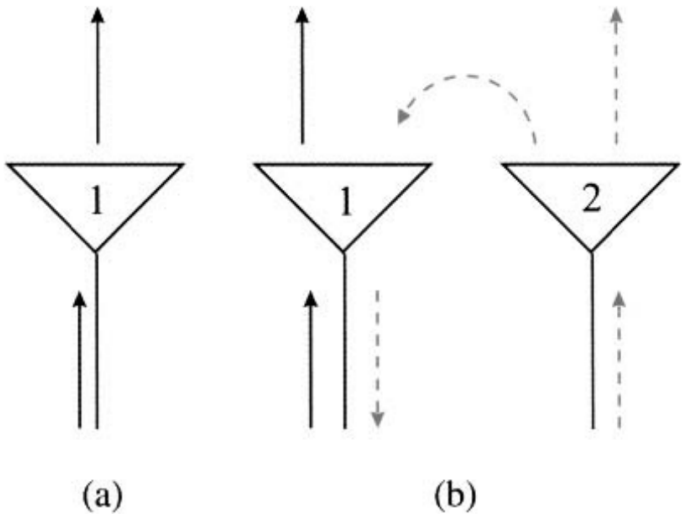

Figure 2.13: Reflected and radiated fields between array elements (a) A matched isolated antenna with no reflections (b) A second antenna in proximity to the first antenna radiating fields that are received by the first antenna [30].

fects the element impedance and is composed of several elements starting with self-impedance which can be described as

$$V_1 = Z_{11} I_1 \tag{2.16}$$

where V_1 is the voltage at antenna element 1 terminal, I_1 is the current on the antenna element 1 terminal and Z_{11} is the impedance of the antenna element 1 in isolation. Self-impedance would be the only impedance present if an antenna was isolated like that in Fig. 2.13(a). The voltage on antenna element 1 due to antenna element 2 radiation can then be described as

$$V_1 = Z_{12} I_2 \tag{2.17}$$

where I_2 is the current on antenna element 2 and Z_{12} is the mutual impedance between antenna element 1 and antenna element 2. The total voltage is the vectorial sum of the incident wave and the re-radiated energy from antenna element 2, the total voltage at antenna element 1 can then be expressed as

$$V_1 = Z_{11}I_1 + Z_{12}I_2 \tag{2.18}$$

This idea that the impedance of one element as a function of other elements in the array can also be expressed as driving point, or active impedance. Active impedance can be described by rearranging (2.18) as

$$Z_{d1} = Z_{11} + Z_{12}\frac{I_2}{I_1} \tag{2.19}$$

A general expression of mutual impedance between any two elements of an array is determined by dividing the open-circuit voltage V_{oc} at the terminals of one element by the current at the other element [30], described as

$$Z_{mn} = \frac{V_m}{I_n} \tag{2.20}$$

The more elements that are added to the array, the more interactions that occur. If the two-element array was extended out to an N-element linear array, then each of the elements would have their own self-impedance or N interactions, while there would be $N(N-1)$ mutual impedances since the element values are capturing the interactions with all other elements. If the impedance matrix of the array containing all the self- and mutual impedances of N-element array is known, then the impedances of all elements in this N-element array can be captured in an $N \times N$ element matrix as follows

$$Z = \begin{bmatrix} Z_{11} & Z_{12} & \dots & Z_{1N} \\ Z_{21} & Z_{22} & \dots & Z_{2N} \\ \vdots & \vdots & \ddots & \vdots \\ Z_{N1} & Z_{N2} & \dots & Z_{NN} \end{bmatrix} \begin{bmatrix} I_1 \\ I_2 \\ \vdots \\ I_N \end{bmatrix} = \begin{bmatrix} V_1 \\ V_2 \\ \vdots \\ V_N \end{bmatrix} \tag{2.21}$$

In this impedance matrix, the diagonal line contains all self-impedances, while all other off-diagonal elements represent the mutual impedances of the N-element array. The mutual impedance Z_{mn}, describes the interaction of element in row m and column n of the matrix. Reciprocity or the relationship between currents and voltages at two points, requires $Z_{mn} =$

Z_{nm} [31]. Mutual impedance is the sum of all the open circuit voltages between two elements divided by the current at the element in question. However, it is more commonly expressed as the summation of the impedances between two elements multiplied by the ratio of the currents seen at each of the respective elements, that is

$$Z_{dn} = \sum_{m=1}^{N} Z_{mn}\left(\frac{I_m}{I_n}\right) \tag{2.22}$$

2.9.4.2 Parameters Affected due to Mutual Coupling

Mutual coupling affects various parameters of array performance. As discussed in the previous section, the impedance of each of the elements is directly affected by the self- and mutual coupling between elements. Because the impedance is affected, so too is the current distribution on each element, and thereby the steering vector of the array. The steering vector is the response of an array towards an incident signal. As a result, other performance parameters would be affected such as the radiation pattern, specifically the direction where the main beam would be directed [32]. There are many other parameters such as direction of arrival (DOA), resolution, interference suppression, and output signal-to-interference noise ratio (SINR) that are also impacted by mutual coupling but will not be expanded further in this thesis.

2.9.4.3 Compensation Methods

Several compensation methods for mutual coupling are available depending upon the source of the coupling in the system. Coupling within the feed network can be mitigated by choosing an appropriate feed system and routing the transmission lines to avoid coupling. Changes to active impedance are more complicated. While the system can be re-matched for the new Z_d value at each element, the driving impedance changes with the scan angle of the array, making it an unreliable methodology.

A different approach to this problem can be taken, instead of designing the array to compensate for mutual coupling, elements can be integrated ensuring an appropriate level of isolation between antenna elements. Requiring elements have enough inter-element distance

is one method. However, if the elements are spaced too far apart this will introduce additional maxima in the radiation pattern. An additional technique uses metal fences (essentially metallic walls) to separate the radiating elements [30], however this has a distinct effect on the antenna pattern, introducing a null, or a direction where no radiation is being received by the antenna.

2.9.5 Array Feeding Schemes

As discussed, the geometric configuration of an array design is one of the factors that determines AF. There are many geometries that have been developed including rectangular, triangular, hexagonal or circular arrangements. An additional critical factor is how these configurations are driven by their feed networks. Specifically, with respect to rectangular geometries, there are two array feed network designs that are commonly used, including the corporate-fed antenna array and the SRA.

2.9.5.1 Corporate-Fed Antenna Array

This configuration is designed with the intent of maximizing gain, with an example of a 2×2 arrangement shown in Fig. 2.14. All the elements are in the same orientation, and the array feed network is designed such that all elements have the same amplitude excitation and phase. As such, this antenna configuration is generally easier to design and can be made large especially at higher frequencies to achieve high gain performance. The trade-off though is this should be used in applications where a smaller bandwidth is required as the IBW, ARBW and GBW can be compromised to some extent [18].

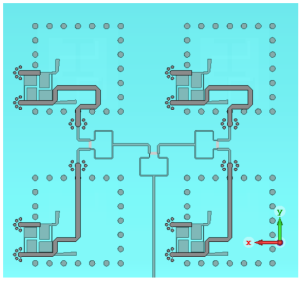

Figure 2.14: 2×2 Corporate-fed antenna configuration bottom view [1].

2.9.5.2 Sequentially Rotated Antenna Array

An SRA is known as a successful technique that can construct a CP array with both wide IBW and ARBW [18]. This is done by rotating each element 90° to neighbouring elements while ensuring that each element are also electrically fed in a progressive phase shift in the same rotational sense. If the excitation amplitudes are identical at each antenna element, then direction of rotation and excitation phase determines the polarization. For example, an RHCP SRA requires all elements be rotated counterclockwise in increments of 90° when viewed from above. Likewise, the array feed network exciting the elements must also have a progressive phase shift which increases by 90° when rotating counterclockwise in the same direction. In addition, the array direction of rotation needs to be the same as the direction of rotation of a CP element. SRAs demonstrate both a wide IBW and ARBW simultaneously but consistently exhibit lower gain when compared to the corporate-fed antenna array stemming from the SRA scheme, when the polarization purity of the CP array is not perfect [18]. An example is illustrated in Fig. 2.15.

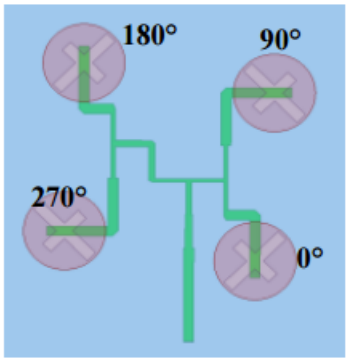

Figure 2.15: 2×2 Sequentially rotated array [33].

2.9.6 GNSS Antenna Array Requirements

The following specifications include fundamental array antenna design and specific GNSS specifications, and are applicable within the GNSS L-band:

- RHCP Gain. Must be greater than the gain that is measured at each element to be

considered an effective array. However, there was no specific minimum standard that could be cited as part of this specification.

- Maximum 3 dB gain drop as a function of frequency. Although not a core GNSS specification, this metric denotes gain stability and is trait of state-of-the-art antenna designs. The first two specifications listed comprise the GBW of the antenna.

- Inter-element distance $d_n < \lambda_0/2 = 93.4$ mm at the upper end of the GNSS L-band must be observed to mitigate significant back lobe radiation.

- FBW $\geq 30\%$. Like standalone antenna design specifications, a bandwidth of greater than 30% is considered wideband, this includes IBW, ARBW, and GBW.

- Antenna area must be less than 210 mm $\times$ 210 mm due to RMC fabrication constraints. This area is valid since it is greater than twice the inter-element spacing distance (for symmetry) at the upper end of the GNSS L-band.

- Antenna height, h. Similar to GNSS antenna design, compact state-of-the-art GNSS antennas are generally less than 10 mm in height.

- Easy access to each of the ports for phased array applications.

2.10 State-of-the-Art in Wideband GNSS Microstrip Antennas

Microstrip antennas have a rich history spanning over seventy years, but it was not until the 1970s that they gained significant attention in research circles. This surge in interest was primarily spurred by the growing military need for phased array radars and the emergence of the telecommunications industry. Additionally, advancements in computational tools further contributed to their exploration.

There are many types of antennas that are available although microstrip or patch antennas are some of the most popular within microwave applications. This is due to their simple design and ease of integration with PCB technology allowing versatile fabrication either as standalone antennas or as part of a larger array. These antennas, typically consisting of

a metal patch separated by a dielectric laminate from a larger ground plane, are available in various shapes and sizes, with electrical size being a crucial factor. An example of a physical model is illustrated in Fig. 2.16(a). This section will delve into their operation, feed mechanisms, and a survey of the current state of the art.

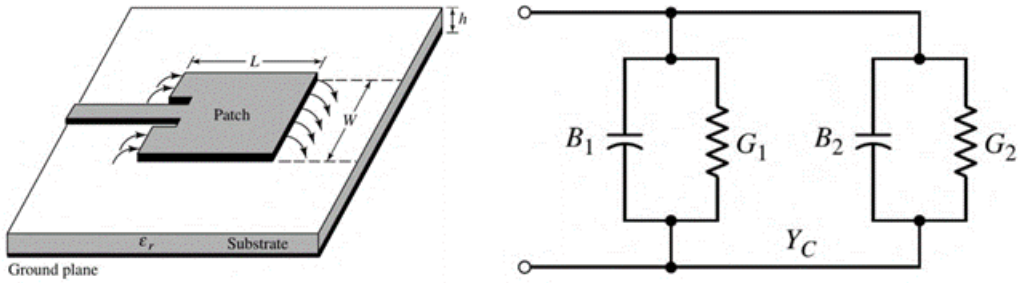

(a) **(b)**

Figure 2.16: Patch Antenna (a) Physical model (b) Transmission line model [13].

The rectangular microstrip antenna is the easiest configuration of patch antenna to analyze. It is generally modelled either as segment of transmission line or a cavity. In the transmission line model as shown in Fig. 2.16(b), the patch is symbolized by two resonant slots, separated by a low impedance transmission line of slightly less than $\lambda_g/2$ to account for fringing affects. The length, L, of a patch corresponds to f_0, while the width, W, determines the input impedance of the patch, Z_0. Features such as patch geometry, substrate height, h, material composition, and element size all impact patch antenna performance.

2.10.1 Patch Antenna Excitation Methods

What may be more important than any of the geometric properties of a patch antenna is the excitation or how the patch is fed electromagnetically. This is a separate feed network discussion from that in Section 2.5 which was in regard to the feed network itself. This section covers the interaction between the feed network and the patch. Typically, these are classified into four categories: printed circuit, probe, aperture-coupled and proximity-coupled excitation methods.

The printed circuit, also known as edge-fed method shown in Fig. 2.17(a), connects a

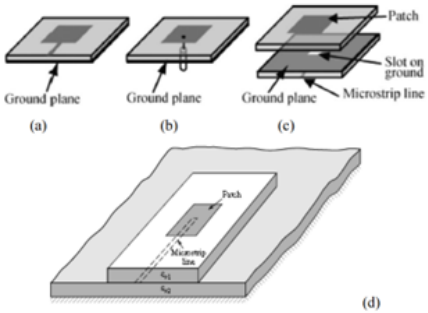

Figure 2.17: Microstrip Excitation Methods (a) Printed circuit (b) Coaxial (c) Aperture-coupled (d) Proximity coupled [34].

printed circuit trace directly to the edge of the radiating patch. The fabrication, impedance matching, and modelling are simple. However, spurious feed radiation, or the unintentional emission of radiation outside the desired band, as well as surface waves, limit the bandwidth of a printed circuit patch antenna to $2-5\%$ [34].

The coaxial or probe fed method, shown in Fig. 2.17(b), is realized using a coax connector with the conducting pin soldered directly to the radiating patch while the coax shielding is soldered to the ground plane of the antenna. This technique has low spurious radiation, is simple to impedance match and easy to fabricate, however is difficult to model with substrate $h > 0.02\lambda$ and is inherently narrowband [34].

Next, is the aperture-coupled method. The entire feed network is placed below the ground plane and is not directly connected to the patch unlike the first two excitation methods. Instead, this feed network is coupled to the patch antenna through a slot or slots in a ground plane as shown in Fig. 2.17(c). This method of excitation was developed to mitigate the spurious radiation effects of the edge-fed model while also improving the bandwidth and simplifying modeling in comparison to the coax feed method. This becomes increasingly important in an array where the losses that would be attributed to the spurious radiation and surface waves could have a significant effect on array performance [28]. In contrast, this feed method can be tedious to design due to the many components, and thus, many parametric design variables required.

Furthermore, fabrication can also be difficult and can be expensive depending on the

number of layers required. However, due to the slots in the ground plane, there is an increase in back lobe radiation present. Nevertheless, because the feed network and patch are not directly connected, each subsystem can be optimized separately without significantly affecting the performance of the other which can simplify modelling [34].

Finally, there is the proximity-coupled patch antenna, depicted in Fig. 2.17(d). In this configuration, the feed line is located between the ground plane and the radiating patch and is known to have the widest bandwidth of all the excitation methods discussed. Like aperture coupling, the fabrication and impedance matching can be difficult, but the spurious radiation is low and the ability to model is simple [34]. What makes this configuration less practical is that it is more challenging to integrate with conventional surface mount components, especially those needed for power dividers or couplers, typically utilized in a microstrip feed design.

2.10.2 State-of-the-Art Wideband Circularly Polarized Patch Antenna Survey

Among these broad categories of patch antennas and excitation techniques, recognizing the multitude of variations published over the past four decades, choices had to be made to streamline the search. Initially, it was determined that a multi-layer, aperture-coupled stacked-patch design was the most advantageous, facilitating the convenient placement of surface mount components and enhance the isolation between the feed network and the antenna element. This configuration supports the balance between high performance and compact size needed for GNSS antenna design.

Many antennas were examined for their ability to meet these fabrication criteria and performance requirements listed in Section 1.2 including [1][2][3][9][14][21][22][35][36] [37], with a summary provided in the remainder of this section.

2.10.3 Wideband Circularly Polarized Microstrip Antenna for Compass and GPS

The first antenna in this literature survey is an aperture-coupled stacked-patch wideband GNSS antenna [14] shown in Fig. 2.18. It features a QFN with one input and four output ports where each of the output port traces are coupled to two square stacked-patches through a crossed-slot in the center of the ground plane. This antenna makes use of medium permittivity dielectric materials, $\epsilon_r = 3.5$ for the feed network and $\epsilon_r = 2.2$ for the patch substrates. This multi-layer design is relatively low profile at 8.5 mm with no air gaps, although the antenna was assembled using screws of unknown material. It has good performance with an IBW, and ARBW that covers the entire GNSS L-band. The QFN utilizes a two-stage power divider design composed of three WPDs and delay lines to excite a progressive phase shift of 0°, 90°, 180°, and 270°. The antenna size was not published so it is unclear whether this antenna is large according to GNSS standards.

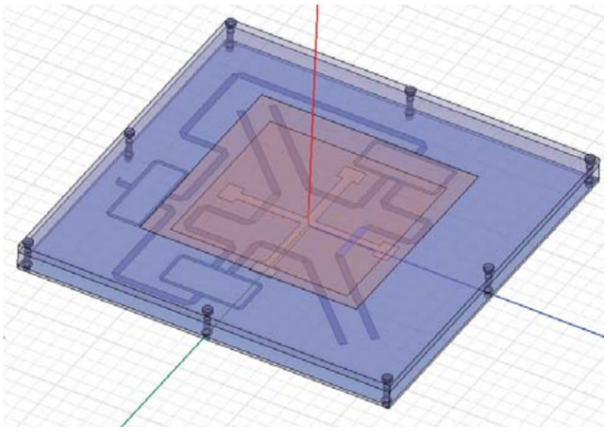

Figure 2.18: GNSS Stacked-patch antenna with QFN [14].

This antenna has several shortfalls. The QFN has a large footprint on the bottom of the antenna which may not allow for enough space to integrate into an array configuration. The gain is not consistent within the GNSS L-band as it is 4 dBic at the upper and lower ends of frequency band but the gain drops approximately 3 dB between 1.375 GHz and 1.51 GHz. It is possible that the gain drop will increase in an array configuration which would significantly decrease GBW and not be suitable for array applications. Lastly, the HPBW is

only 80° where GNSS antennas should be $100° < \theta < 140°$ depending on the application.

2.10.4 Wideband Antenna for Global Navigation Satellite Systems

A different route was chosen to achieve high performance in [35], depicted in Fig. 2.19. Two L-probes are used to excite an aperture coupled square patch at two perpendicular locations to generate CP. L-probes are a class of proximity-coupled excitation method where instead of a printed circuit trace, bent wires in an air substrate are coupled to the radiating aperture.

This antenna has three substrates, the upper substrate is printed on a thin FR-4 board 1 mm thick ($\epsilon_r = 4.4$ and $\tan\delta = 0.02$) and has an etched cross-slot to reduce the size of the radiating patch. The middle substrate is air and encompasses two L-probes above a ground plane. Below the ground plane is a relatively simple microstrip 90° Wideband Power Dividing Phase Shift Network, printed on a double-high permittivity Rogers RO3010™ ($\epsilon_r = 10.2$ and $\delta = 0.0035$) where the two outputs are connected to two L-probes. This antenna poses excellent performance. First, it has an IBW of 62.80% owing to the robustness of L-probe coupled feeds in air gaps. Second, this antenna has an ARBW of 51.9% due to the balanced output port power distribution and consistent phase imbalance bandwidth of 45.69% from the use of a single-coupled-line phase shifter. Finally, the gain is greater than 2.1 dB over the entire L-band with a peak gain of 6.24 dB at 1.25 GHz.

This antenna has several shortcomings. One stems from the use of the L-probes. Although this type of feed can significantly improve antenna performance, it would not be simple to fabricate and creates variability in assembly dimensions that could affect antenna performance. Furthermore, the use of L-probes, requires a large antenna, with planar dimensions of 140 mm × 140 mm and height of 22.3 mm with 90% of the height owing to the air gap substrate. Due to the size of the antenna, its versatility would be limited, and it would not be possible to use this antenna in an array configuration at this time. Another issue, similar to the previous example, there is a large variability in gain across the band, exceeding a 3 dB drop in gain. The radiation patterns were not published and thus there is no comment available on the HPBW of this antenna.

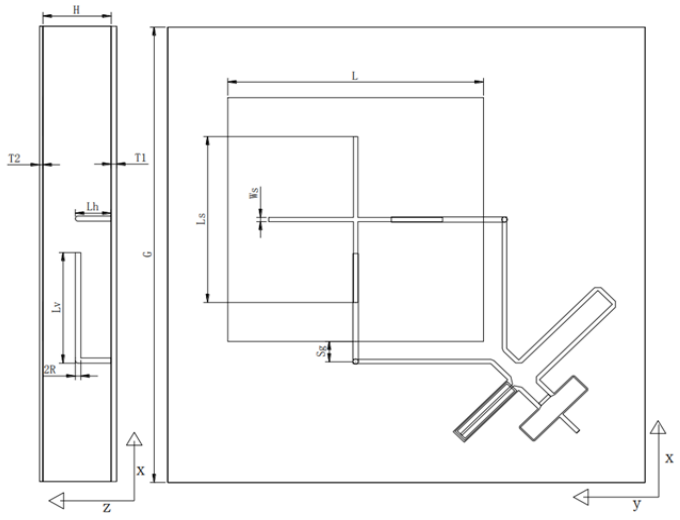

Figure 2.19: GNSS L-probe coupled wideband antenna with side and top views [35].

2.10.5 Wideband Circularly Polarized Slotted Multi-Port Patch Antenna for High Precision GNSS Systems

In this wideband microstrip antenna design found at [36], a 60 mm diameter slotted circular patch is etched on 1.52 mm thick substrate ($\epsilon_r = 3.5$, $\tan\delta = 0.0018$). The patch is mounted 20 mm above a ground plane that is plated on a laminate with the same properties as the patch substrate except larger in size as depicted in Fig. 2.20. One cross-slot and four sets of two concentric ring slots are etched into the radiation patch to decrease the size and increase the performance of the antenna. Soldered to the center of each of the ring slots are coax feeds which are driven by a QFN located at the bottom size of the lower dielectric. This feed network is composed of a two-stage WPD with delay lines that generate a progressive phase shift feeding each of the concentric ring slots.

This antenna requiring only one radiator has measured results demonstrating high GNSS performance with 45% IBW, 42.8% ARBW and with a gain greater than 4 dBic over the entire GNSS L-band including a peak gain of 7.9 dBic at 1.575 GHz. Despite the high performance, it features some limitations especially for use in an array. First, the element is large. With simulations featuring a ground plane size of $160-200$ mm owing to both antenna performance optimization and the size of the QFN, this is a large GNSS antenna and would

be too substantial in size to be featured in an antenna array without introducing back lobes. Second, the use of stand-offs and wire pins between the patch and the larger ground plane would make fabrication of this design tedious having similar non-standard PCB fabrication technique issues to other antennas described in this section. In addition, there is a large variation in gain resulting in a GBW $\approx$ 23%. No comment on HPBW as this information was not available.

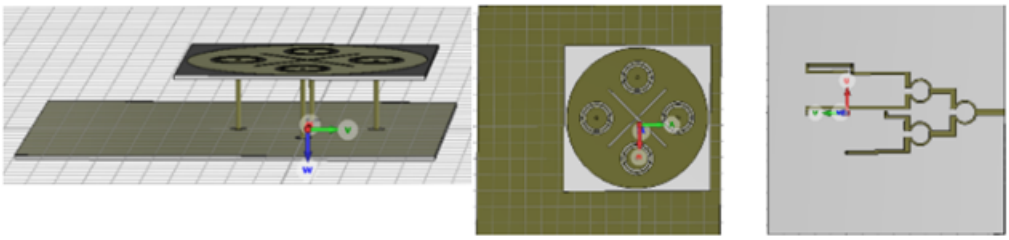

(a) **(b)** **(c)**

Figure 2.20: Patch Antenna (a) Side view (b) Top view (c) Feed network (bottom view) [36].

2.10.6 Compact Wideband Patch Antenna for GNSS Application Using Shorting Loaded Pins

The antenna from [37] presented in Fig. 2.21, uses a shorting loaded square patch to increase the bandwidth of patch antenna. The size and position of the shorting pins inside the patch, decompose the dominant resonance mode of patch antenna into two secondary modes at different frequencies that are combined to form a wideband response. The inner four probes are connected to the feed network whereas the outer four probes are connected to ground. The antenna radiating element is etched on a microwave composite ($\epsilon_r = 6$ and $\tan\delta = 0.002$), 15 mm in height and 50 mm in width and length. The radiating element is mounted on a ground plane that is much larger, 120×120 mm in size. On the other side of the ground plane is where a QFN is etched on 0.8 mm of Rogers RO4350B™ ($\epsilon_r = 3.48$ and $\tan\delta = 0.0037$). This device achieved high performance with an IBW, ARBW and a suitable gain profile that covered the entire GNSS L-Band. In addition, the HPBW of the antenna was found to be 120° which is ideal for GNSS applications.

While the methodology to generate a wideband response is unique, the antenna requires

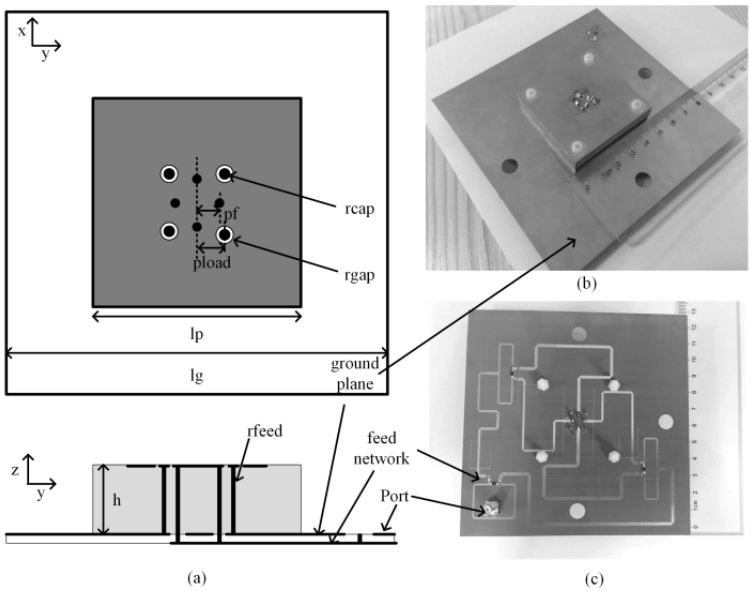

Figure 2.21: Compact wideband GNSS patch antenna using shorting loaded pins (a) Structure and the fabricated photograph of (b) GNSS antenna and (c) Feed network [37].

the use of high permittivity materials which decrease the device bandwidth and in part, necessitated the use of a QFN. Consequently, the feed network substrate would have to be increased to decrease the size of the feed network in order to meet the $\lambda_0/2$ inter-element distance array design limit. As such, it is unclear how these changed may affect the performance of the antenna.

2.10.7 Triple Stacked-Patch GPS Wideband Circularly Polarized Microstrip Antenna Array

The antenna element shown in Fig. 2.22 from [22] was designed for GPS (GNSS) applications. It is composed of three resonant patches and a DFN etched on the bottom side of a grounded substrate that is coupled to the patches through two U-shaped slots. Each of the four laminates are 1.524 mm thick and are composed of Rogers RO4003™ ($\epsilon_r = 3.38$ and $\tan\delta = 0.0027$) while all the substrates have 10 mm air gaps between them. The DFN is composed of a T-junction power splitter and a two-section Schiffman phase shifter with a 270° delay line on the opposite trace. This high-performance feed network measured a phase imbalance $< \pm 2°$ and power imbalance of < 0.5 dB and an IBW of 29% virtually covering the entire

GNSS L-band. This antenna element was designed as part of a larger 2×2 SRA as shown in Fig. 2.22(b). The array exhibited a $|S_{11}| < -15$ dB, an AR < 1.2 dB and the gain for the array was measured at $8 - 12.5$ dBic spanning across the entire GNSS L-band.

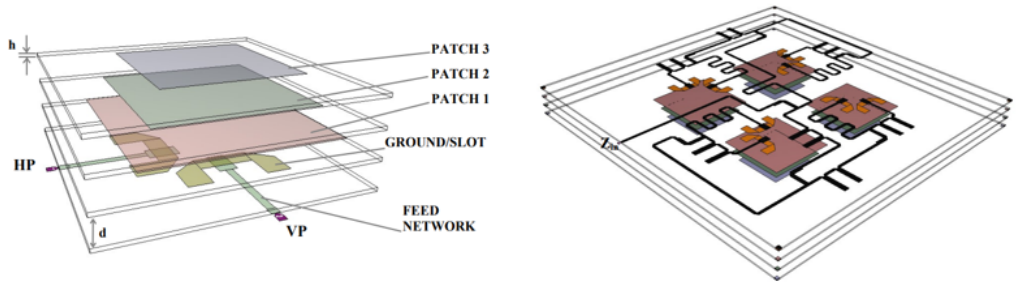

(a) **(b)**

Figure 2.22: GNSS triple stacked-patch aperture-coupled antenna element (a) 2 × 2 SRA (b) [22].

The antenna element was specifically designed to be a part of an array. This required the design of a compact DFN that could incorporate an array feeding network. In fact, the antenna elements were able to be spaced 65 mm from the center of each element to the center of the array. Also, since Schiffman phase shifters and T-junctions were used for the feed network, no surface mount components or vias were required. Additionally, there was only one substrate that was used leading to lower cost of fabrication. However, three resonant patches for a wideband response and thus three air gaps were needed for optimized performance leading to a total antenna height of approximately 36 mm. In addition, despite how close the antenna elements could be placed together, the antenna array is still large at 350 mm × 350 mm in planar dimensions. A larger antenna array utilizing this configuration would result in a bulky design that would be difficult to fabricate.

2.10.8 Dual-Circularly-Polarized Stacked Patch Antenna for SOTM application at Ka-band

This final antenna is a SOTM antenna design with the frequency of operation between $18-20$ GHz in the Ka-Band [1]. What also sets this antenna apart from all others in this survey is that it includes the use of both a microstrip layer and a stripline layer as part of the feed network as shown in Fig. 2.23. These researchers were attempting to minimize the element

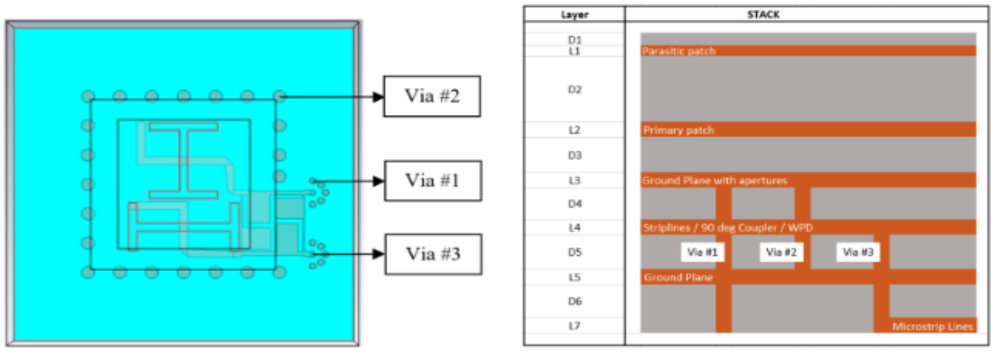

(a) **(b)**

Figure 2.23: SOTM aperture-coupled stacked-patch antenna (a) Top view (b) Side view [1].

size so to be able to integrate active elements such as LNAs, reconfigurable switches in a PCB stack-up. Furthermore, the antenna element size is small enough to be part of an array since it was ultimately designed as both a 2×2 and 4×4 antenna array. The substrates include Rohacell® 31HF ($\epsilon_r = 1.04$) foam spacer between the parasitic and primary patches and a medium relative permittivity substrate, Isola I-Tera®, for the remainder of the substrates. This antenna could be fabricated using standard PCB fabrication techniques. Within the frequencies of interest, the gain of the antenna element is $4 - 4.4$ dBi well within the average gain of a GNSS antenna. Furthermore, the $|S_{11}|$ and AR are below the < -10 dB and < 3 dB levels respectively.

The major disadvantage of this design is its bandwidth $15 - 18\%$ which is well below the $> 30\%$ bandwidth needed for GNSS wideband performance. This is largely due to the use of a single-stage hybrid coupler shown in Fig. 2.23(a). Based on this configuration, use of a feed network with a wider bandwidth response could increase the size of the antenna element beyond the $\lambda_0/2$ inter-element spacing requirement without the use of further size reduction techniques.

2.11 Summary

An overview of microstrip antennas was presented along with the current state of research in the field. This includes antenna and feed network fundamentals and wideband response design. Additional discussion included requirements for GNSS antennas, patch antenna and antenna array design criteria. While there has been much work done in this area, there are design issues that remain. This primarily concerns the design trade-off between wideband performance of GNSS antennas and compact size that could permit its use in an array configuration.

During the literature survey, the feed network was identified as the primary area of interest due to the demanding bandwidth needed for GNSS L-band antennas. After evaluating the current state of the art in CP, wideband microstrip antennas, of which most were for GNSS applications, only the antennas in [1] and [22] specifically were designed as part of a larger array. All other antennas would have been too large to be used in an array configuration due to the size of the ground plane or the feed network. Although the antenna at [22] was high performance its 2×2 configuration was large. One design, though, has large potential in this area, the SOTM aperture-coupled stacked-patch antenna, shown in Fig. 2.23, due to it being dual-fed and only with the use of PCB materials. The following chapters describe the investigation of a dual-fed GNSS aperture-coupled stacked-patch antenna, PCB integrated design and array integration.

Chapter 3

GNSS Aperture-Coupled Stacked-Patch Antenna

3.1 Introduction

Antenna 1, the GNSS aperture-coupled stacked-patch antenna, described in this chapter, must be wideband, or $> 30\%$ bandwidth over the GNSS L-band, including IBW, ARBW and GBW. Next it must be compact size according to both GNSS antenna design requirements and in comparison to other state-of-the-art designs. Finally, Antenna 1 must be able to be integrated into an array requiring the center-to-center inter-element spacing be less than half the smallest wavelength in the GNSS L-band i.e. $d_n < \lambda_0/2 = 93.4$ mm. As a result, there must be enough space on the feed network plane to be able to incorporate other element feed networks and an array feed network. Chapter 5 details the attempt to prove whether the last criterion can be achieved.

In addition, Antenna 1 must achieve high performance using only standard PCB materials such as core laminates and prepreg rather than the use of any air gaps or L-probes ensuring the most compact and versatile design possible. This balance between performance and size necessitate the use of a multi-layered, uniform medium permittivity substrate.

There are no existing GNSS antennas that attempted this design and met the performance criteria as detailed in Chapter 2. From those elements surveyed, high performance was achieved using one of three methods. One method included the use of a QFN where four

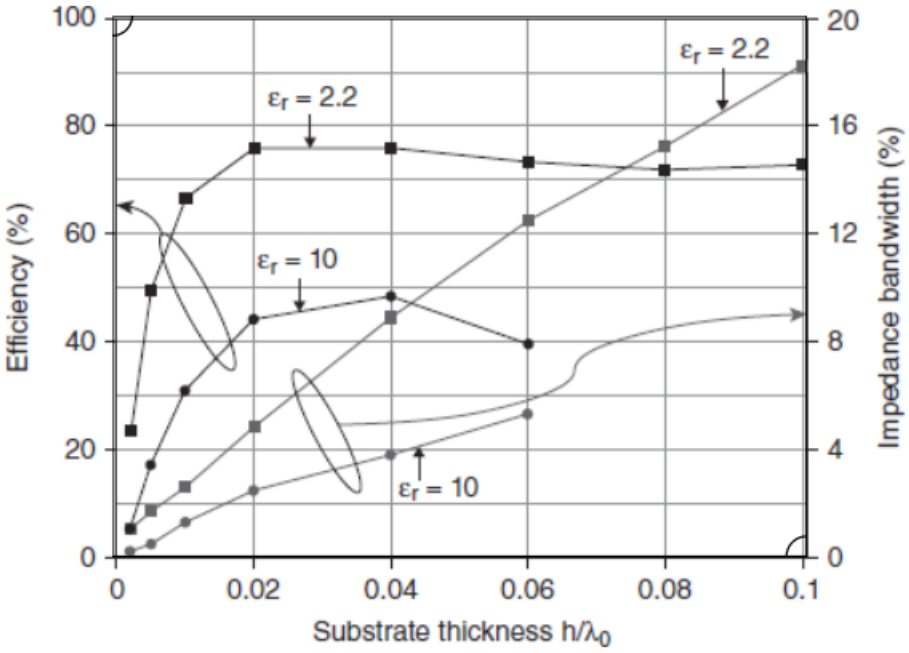

Figure 3.1: Effect of substrate thickness and dielectric constant on the impedance bandwidth (VSWR < 2) and radiation efficiency [28].

feed points are required to achieve a progressive phase shift of 0°, 90°, 180°, and 270°. This feeding scheme has a robust IBW and ARBW which can be hard to achieve with a dual-fed antenna. The issue though is that there would be limited space to add traces to feed the patches without violating the inter-element spacing requirement when using lower permittivity materials. Another method was through the design of large and tall antennas that utilized probes and/or air gaps which are not suitable for use in array applications due to their large size and bulky design. Finally, there are some designs that use high permittivity materials to achieve a minimized design that could reduce antenna performance, especially if used as part of an antenna array.

As detailed in Fig. 3.1, for small substrate heights, IBW increases as the height of the antenna increases. Additionally, as the substrate ϵ_r increases, the antenna is able to store more energy and increase its Q or quality factor, thereby decreasing its bandwidth [28]. Thus, tall antennas with an air gap ($\epsilon_r \approx 1$) will provide a high IBW. Air gaps also allow for superior flexibility as any air substrate height can be used while other dielectrics

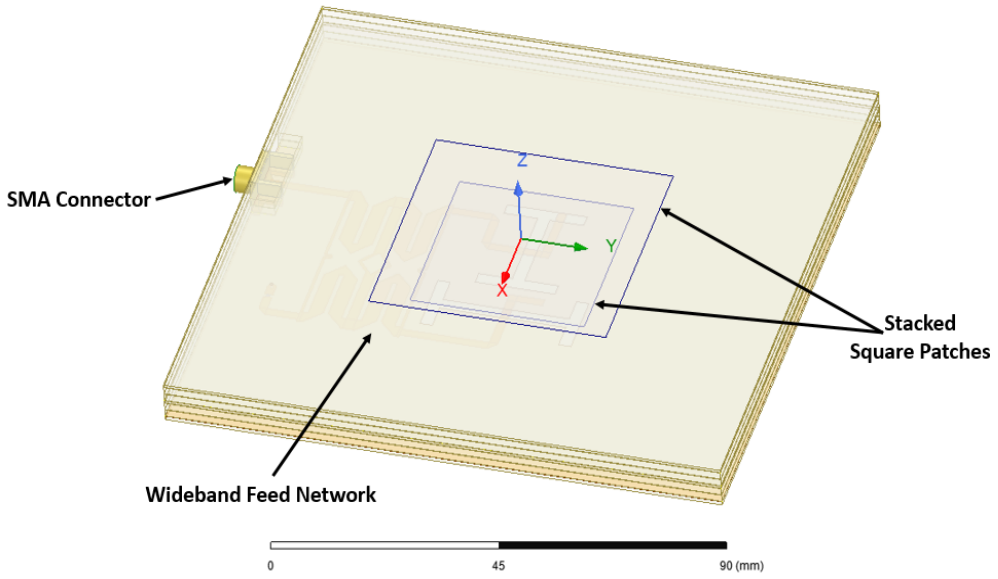

Figure 3.2: HFSS model of Antenna 1

typically come in a specific thickness that become a design constraint. Furthermore, air gaps can be used in conjunction with probe assemblies that have been known to provide robust impedance matching with patch antennas [9][35]. However, these benefits in performance come at the expense of increased size, and reliability of fabrication. Conversely, higher permittivity materials result in an antenna design with lower performance, in particular a smaller bandwidth.

With these ideas and the three main criteria in mind, the course of this thesis led to the dual-fed aperture coupled stacked-patch antenna presented in [1] to be strongly considered for further investigation. That antenna was designed and developed using standard PCB fabrication techniques and was able to be designed in both in 2×2 and 4×4 corporate array configuration.

An HFSS model of Antenna 1, shown in Fig. 3.2, illustrates the adaptation of the aperture-coupled stacked patch antenna element [1] from Ka-Band to an operating frequency at mid-L-band, using only Isola I-Tera® MT-40 (RF/MW) laminates ($\epsilon_r = 3.45$ and $\tan\delta = 0.0031$). Additionally, this design incorporates an UWB BLC [4] adapted from the original operating frequency of 2.4 GHz also to mid-GNSS L-band, 1.4 GHz. In addition, the use of

a uniform permittivity substrate and equal substrate heights above and below the primary patch was inspired by the stacked patch aperture coupled GNSS antenna at [3].

The remainder of this chapter will discuss the design process of the UWB BLC feed network, followed by the design details of Antenna 1, then fabrication procedure and concluding with an analysis of simulation and experimental testing results.

3.2 Wideband Feed Network

Typically, the feed network is discussed in the context of the larger antenna design, but it was necessary to provide a dedicated discussion due to its critical nature of the overall antenna performance. The antenna element from [1], utilizes a miniaturized single-stage hybrid coupler that is connected to stripline traces that couple with the radiators. The results from this antenna having an ARBW and IBW of 15-18% which is significantly less than the $> 30\%$ bandwidth requirements for covering the GNSS L-band. As it happens, this is primarily a function of the feed network as a single stage hybrid coupler has a theoretical bandwidth upwards of $15 - 20\%$ and would not be able to support wideband performance without modification. Similarly, a single stage 90° Wideband Power Dividing Phase Shift Network would not support this application either without the use of probes and air gaps found in the literature survey. Therefore, additional stages had to be added to the feed network. This led to the investigation of a two-stage BLC.

3.2.0.1 Conventional Two-Stage Branch-line Coupler

As discussed in the previous chapter, a two-stage BLC, shown in Fig. 3.3(a) increases the IBW and ARBW of a single-stage BLC to $45-50\%$. However, the BLC is approximately twice the size, $\lambda_g/2 \times \lambda_g/4$. Because of the uniform permittivity substrate design of the antenna, a conventional BLC would be of similar dimensions to that of the radiating aperture. This requires a larger antenna area to incorporate all the traces of this feed network and in addition to a larger size, the BLC must remain clear of the ground plane slots in the center of the antenna to avoid any undesirable coupling. Ultimately, the use of a conventional BLC in the

Antenna 1 design would result in a large GNSS antenna that would be difficult to integrate into an array.

A simple solution could have been to simply increase the permittivity of the two-stage BLC substrate to a much higher value, but this would reduce the bandwidth of the BLC and therefore, impact antenna performance and likely require the use of a QFN, further increasing the size and complexity. As such, an alternative solution was required to include a wideband device that could be used on a more medium permittivity material to minimize size while maximizing performance.

3.2.1 Ultra-Wideband Two-section Branch Line Coupler Feed Network

A thorough survey was conducted to find a BLC that addressed these design considerations. This included the use of parallel-coupled three-line configuration [20], ATLs [38] and settling on single-coupled-lines from UWB two-section hybrid coupler shown in Fig. 3.3(b).

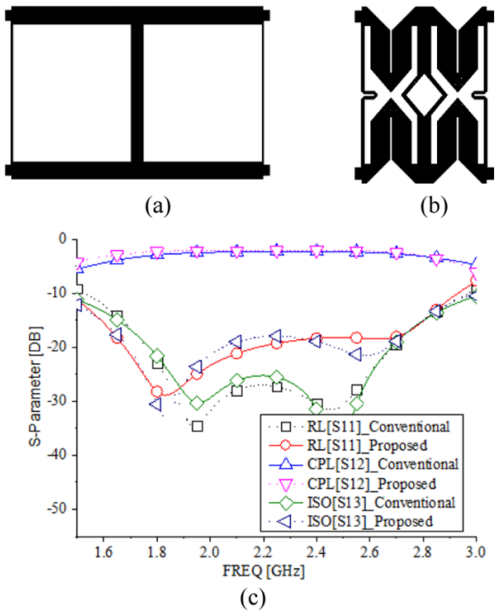

Figure 3.3: (a) PCB layout of conventional 3 dB BLC and (b) PCB layout of UWB coupled-line 3 dB BLC (c) Simulation result comparison [4].

This hybrid coupler with an operating frequency centered at 2.2 GHz is 48% of the area of a conventional hybrid coupler. This design has a similar performance to a conventional

two-stage BLC of 54.6% IBW and excellent power division over the band centered at 2.2 GHz as illustrated in Fig. 3.3(c). These results are promising for wideband GNSS antenna performance and the antenna array element design. The compact design was realized using four folded arms. These circuits are single-coupled-lines that can approximate transmission lines. This is possible because the response of this circuit is that of an all-pass filter [11].

3.2.1.1 Adapted Design

To use this design, it needs to be adapted from a center frequency of 2.2 GHz down to a 1.4 GHz to operate squarely in the GNSS L-band. This primarily involved lengthening the coupler such that the shunt arms and coupled arms were extended by a ratio of roughly 2.2/1.4 corresponding to the ratio of operating center frequencies. However, the design required many parametric simulations to optimize the performance of the device.

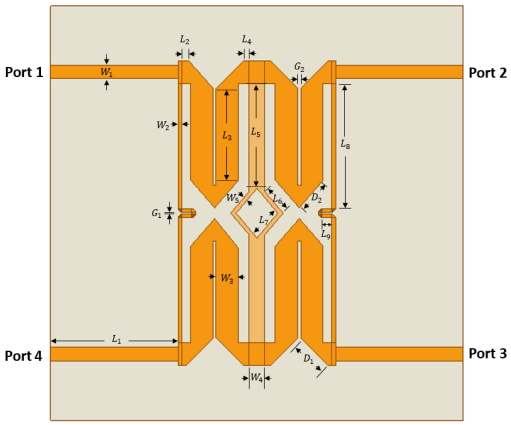

Figure 3.4: HFSS model of adapted UWB BLC design

The choice to only lengthen the coupler was needed to minimize the width of the BLC and maximize the length available for the microstrip traces extending from each of the ports. In particular, the input port connected to the SMA connector at the edge of the board and output ports coupled to the slots in the middle of the antenna. The same substrate and thickness, Isola I-Tera® MT40 (RF/MW) ($\epsilon_r = 3.45$, $\tan\delta = 0.0031$) and $h = 0.762$ mm was used so that the width of the transmission lines remained the same minimizing design overhead. The illustration of the design and relevant dimensions are provided in Fig. 3.4

Table 3.1: Adapted UWB BLC dimensions

Parameter	Dimension (mm)	Parameter	Dimension (mm)
D_1	5.01	L_6	3.83
D_2	4.95	L_7	4.39
G_1	0.26	L_8	17.04
G_2	0.39	L_9	1.29
L_1	17.4	W_1	1.74
L_2	0.9	W_2	0.51
L_3	12.43	W_3	3.06
L_4	0.75	W_4	2.16
L_5	14.2	W_5	0.55

and Table 3.1 respectively.

3.2.1.2 Simulation Results and Discussion

The magnitude simulation results of $|S_{11}|$, $|S_{21}|$ and $|S_{31}|$ of the adapted UWB BLC are shown in Fig. 3.5(a). The goal of this design was to ensure that the $|S_{11}| < -15$ dB was achieved over the entire L-band to ensure that the antenna matching could be achieved with the radiating aperture.

Additionally, a -1 dB difference in amplitude between output ports 2 and 3 centered about -3 dB was expected over the band of interest. The $|S_{11}| < -15$ dB across the band while the difference in output amplitude, $|S_{21}| - |S_{31}|$ was less than -1 dB for 33.1% bandwidth with a center freq of 1.4 GHz. Fig. 3.5(b) exhibits the phase change variation The results showed that the differential phase between outputs, $\angle S_{21} - \angle S_{31}$, only varied between 89.5° and 92.4° which is below the $90 \pm 5°$ variation that was expected for a robust performance of a wideband feed network.

3.3 Antenna Design

3.3.1 Square Patch Design

The rectangular patch is well documented in literature and there is a comprehensive understanding of its behaviour and radiation characteristics [13][28]. It is often modeled as a rectangular cavity where the patch is a perfect electric conductor (PEC) with a perfect

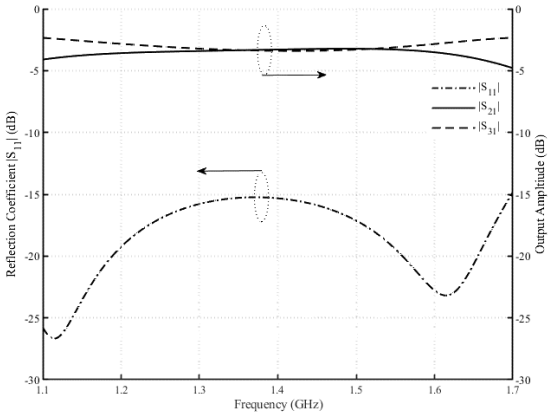

(a)

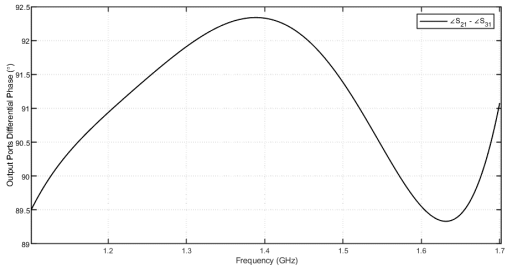

(b)

Figure 3.5: Adapted UWB BLC simulated results (a) S-parameter amplitude (b) S-parameter phase variation

magnetic conductor (PMC) at the edges of the patch corresponding to an open circuit. In addition, the substrate height is small ($h << \lambda$) and the dielectric material is truncated beyond the edge of the patch to minimize surface waves in the patch. The normalized electric field of a rectangular patch antenna is described in (3.1) where L and W are the length and width of the patches and m and n are the indices of the mode of operation. The variables expressed in (3.1) correspond to those dimensions listed in Fig. 3.6. The resonant frequency of operation is described in (3.2) where c_0 is the velocity of light in free space.

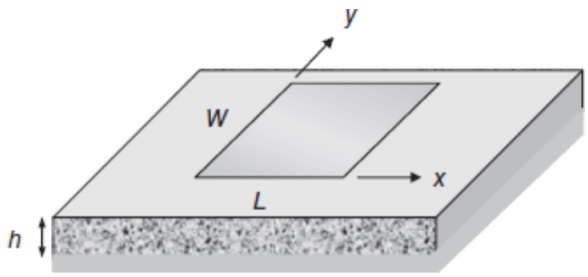

Figure 3.6: Rectangular Microstrip Patch Antenna [28]

$$\mathbf{E_z}(\mathbf{x},\mathbf{y}) = \cos\left(\frac{m\pi x}{L}\right)\cos\left(\frac{n\pi y}{W}\right) \tag{3.1}$$

$$(f_0)_{10} = \frac{1}{2L\sqrt{\mu\epsilon}} = \frac{c_0}{2L\sqrt{\epsilon_r}} \tag{3.2}$$

The usual mode of operation is TM_{10}, where there is no variation in the electric field in the x direction and L is approximately one-half wavelength in the dielectric cavity. This mode of operation corresponds to a broadside radiation pattern that would be normal to the surface of the patch, in this example, the $+\mathbf{z}$ direction. For this mode, the patch acts as a wide microstrip transmission line where f_0 is determined by the L and the input impedance of the patch is determined by W. To improve bandwidth and reduce input impedance, the ratio of $W/L = 1.5$ is typical [28].

Except for the circular patch in the literature survey, all the state-of-the-art patches antennas were square. This is common for wideband state-of-the-art CP antennas including GNSS antennas as the rectangular patch is not optimal for CP operation. The magnitude components of the electric field need to be within 3 dB of each other to stimulate CP and sufficient AR. Therefore, symmetry of the patch geometry requires the use of a square patch instead of a rectangular patch. This geometry, however, introduces changes in input impedance and decreases bandwidth. As such, there is a requirement to better match the input impedance of the patch and thus improve bandwidth of the antenna while ensuring the patch has a strong CP capability.

3.3.1.1 Wideband Patch Antenna

The next issue to address is the wideband capability of the antenna. There have been many ways to address patch bandwidth, including slots in patches or ground planes, multiple feeds, or multiple patches. In all these cases, the intent is to introduce multiple resonances within the band of concern to form an overall wideband response.

In line with antennas in [1][3][14][22], the aperture-coupled stacked-patch design was ultimately the investigated patch configuration. The benefits from this design would be two-fold as both the stacked-patch and aperture-coupled designs both increase the bandwidth of the antenna. Changes to the feed network could be made independently of the patch and thus making it easier to facilitate the use of parametric modelling analysis.

Furthermore, neither the stacked-patched nor the aperture-coupled designs increase the footprint of the antenna but only its height. It was important that the height of the antenna remain < 10 mm as this would be comparable to other similar state-of-the-art designs. A more detailed view of the antenna can be found in Fig. 3.7. Of note, the sizes of the primary and parasitic square patches are $L_{p1} = 36$ mm and $L_{p2} = 49$ mm and the size of Antenna 1 is 115 mm $\times$ 115 mm $\times$ 8.5 mm.

3.3.1.2 Substrates

The substrate thicknesses of Isola I-Tera® MT40 core laminates with $\epsilon_r = 3.45$ are limited to 5 (0.127), 10 (0.254), 20 (0.508), 30 (0.762) and 60 (1.524) mil (mm). This is a relatively standard choice of boards available from a variety of manufacturers. This substrate was chosen due to its medium $\epsilon_r = 3.45$ to balance performance and size while still offering a lower $\tan\delta = 0.0035$ to reduce dielectric losses that would be found in more popular and cheaper substrates such as FR-4. The use of only this substrate was selected to minimize variation of materials and design overhead as this also is the same substrate that is used for the UWB BLC design.

A uniform permittivity substrate is atypical as the feed network is generally composed of a higher permittivity than the patches to have more confined fields and minimize any unintended feed line coupling. Also, within the stacked-patch substrates, the parasitic or

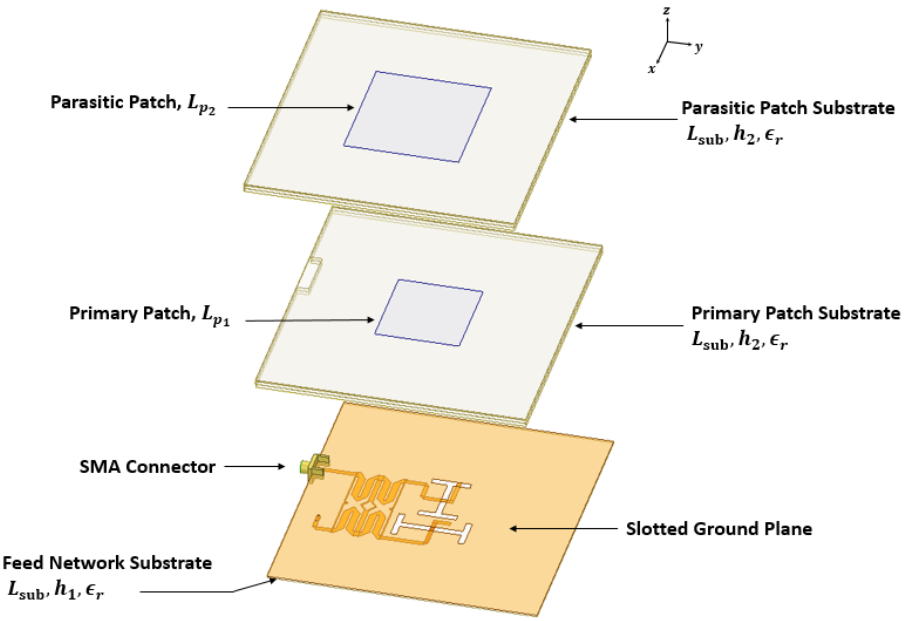

Figure 3.7: Antenna 1 model exploded view

upper patch substrate is generally a thick substrate with lower permittivity than the primary patch substrate to allow for more loosely confined fields, improving IBW and radiation efficiency. In this design, the feed network is situated on 0.762 mm core laminate, the primary and parasitic patches are located on 3.8 mm substrates, each composed of 2 x layers of 1.524 mm and 1 x layer of 0.508 mm core laminate.

In order for all of these layers to be attached, the core laminates are not the sole material this multi-layer board, but also a prepreg that binds the core boards together. Extensive research was conducted on the prepreg material and manufacturing process to comprehend its modeling in a multi-layer dielectric [39][40]. Various configurations were simulated using HFSS, altering the material and its thickness. The prepreg Isola I-Tera® MT40 with 65% resin content, thickness of 0.089 mm and $\epsilon_r = 3.31$ was selected to meet the height requirements of the antenna. Nevertheless, the performance of the antenna showed limited variation, perhaps due to the comparable permittivity and minute thickness of the prepreg layer where it accounts for only 0.53 mm or about 6% of the total antenna height.

3.3.1.3 Slot Design

The slots used in Antenna 1 were adapted from the I-slots in [1]. Bowtie slots were initially considered as they feature the largest bandwidth of all slot geometries [41]. However, for CP operation, two orthogonal slots would be required. If bowties were used there would be a risk of slot overlap or being too close to one another that would introduce undesired coupling. As such, the geometry with the next best bandwidth was the I-slot.

There were many parametric simulations that were carried out to determine an optimal design. This included the slot locations, width, length of the slot and slot ends. The slot ends are designed to increase the electric length of the slots. Therefore, the slot ends of the vertical slot had to be longer than the horizontal slot to ensure similar electrical lengths for the correct resonant frequencies and robust CP operation. Complementary to the design of the slots were feed line microstrip impedance, stub lengths for both slots, and feed location.

3.3.1.4 Integrated Branch-line Coupler Feed Network

A bottom view of the GNSS Antenna 1 is shown in Fig. 3.8. As the feed network needed to be integrated into the antenna, there were some changes in reference to the original adapted design in Fig. 3.4. There were several reasons for this. First, the input port had to be adapted so that the system could be excited by an SMA connector at the edge of the antenna. Second, the port 2 and 3 traces needed to navigate around the I-slots so that they could properly couple with the radiating aperture. Finally, the isolated port needed to be terminated which required a surface mount resistor and ground via.

In addition, tuning stubs that extended beyond the I-slots were included for further performance enhancement of the antenna. However, there were some changes that needed to be made to the coupler mainly to tune the AR of the system. This required the single-coupled-lines to be adjusted to optimize ARBW. Tuning of this parameter proved to be more difficult than expected due to the asymmetry of the position and size of the I-slots. A full description of the integrated UWB BLC dimensions can be found in Table 3.2. Note that the O dimensions refer to offsets where O_1 is the offset from the edge of the substrate and O_2 and O_3 indicate the medial position of each of the orthogonal slots to a center line running

horizontally across the antenna in the y-axis. The simulated model of Antenna 1 was initially defined using the variables that are identified in this chapter. Then, the geometry of this design was optimized using parametric studies and the optimetrics module in HFSS.

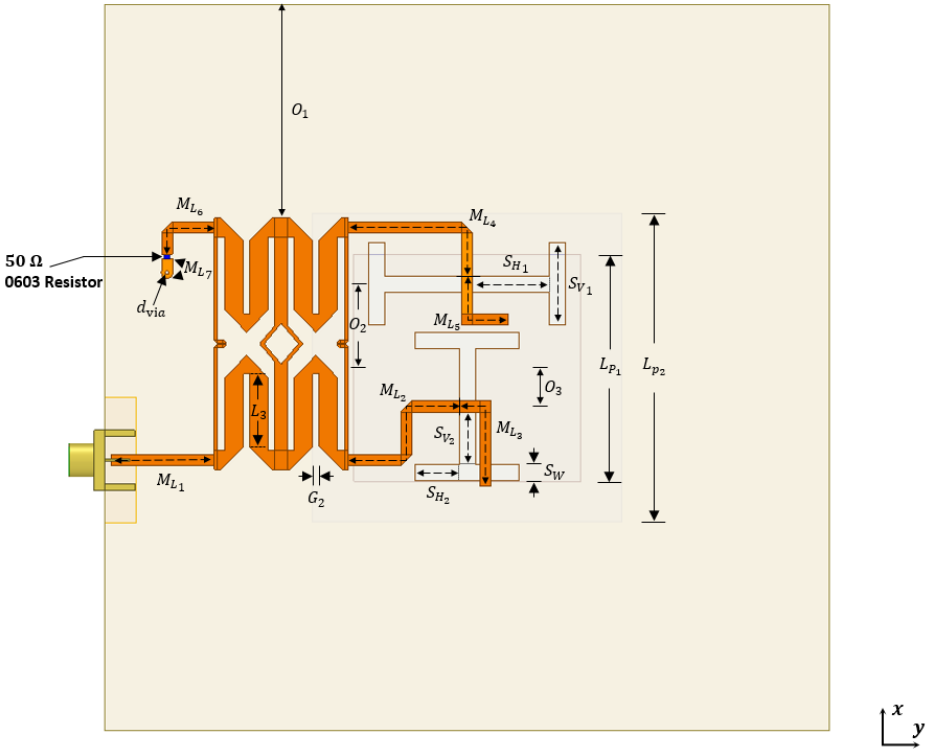

Figure 3.8: Antenna 1 bottom view

3.3.1.5 Antenna 1 Planar Size

In literature, it is not always common to publish the overall planar antenna size. However, as this is one of the requirements for this antenna, it is necessary to include this information. Antenna 1 measures 115 mm × 115 mm. As this antenna size is $<$ 120 mm in its longest dimension, it is not considered a large and is comparable in size to other current state-of-the-art GNSS antennas. According to [13], the size of ground plane required for a patch is given in (3.3) and (3.4) where W_g is the ground plane width and L_g is the ground plane length and h is the height of the entire substrate. This scenario requires $L_g = W_g = 94.6$ mm for

Table 3.2: Antenna 1 dimensions

Parameter	Dimension (mm)	Parameter	Dimension (mm)
d_{via}	0.6	M_{L_6}	12.23
G_2	0.99	M_{L_7}	2.21
L_{p_1}	36	O_1	33.77
L_{P_2}	49	O_2	13.26
L_{sub}	0.386	O_3	6.16
M_{L_1}	16.41	S_{V_1}	8.292
M_{L_2}	26.18	S_{V_2}	6.97
M_{L_3}	16.79	S_{V_3}	12.18
M_{L_4}	26.6	S_{V_4}	5.25
M_{L_5}	15.83	S_W	2.55

the parasitic patch L_{p2} of 49 mm and a substrate height of 7.6 mm above the ground plane. However, the ground plane size needed to be increased due to the size of the feed network trace extending out to the edge of the substrate. The trace could have been modified to minimize ground plane size, but this required changes that would have significantly modified the design of the antenna. Therefore, some modifications will be required to integrate this device into an array design.

$$W_g = 6h + W \tag{3.3}$$

$$L_g = 6h + L \tag{3.4}$$

3.4 Performance Criteria

There were several performance specifications that were the focus of the antenna performance, including IBW, ARBW and GBW across the entire L-band. In addition, the overall radiation pattern is a parameter of interest with particularly, HPBW and FBR, measured at three frequencies, 1.18 GHz, 1.25 GHz and 1.575 GHz.

The IBW was achieved using the optimization of the UWB BLC, the primary and parasitic patch sizes and stub lengths. Then, the ARBW was concentrated on. This was found to be the most difficult parameter to optimize. This involved optimization of the I-slot sizes and

their locations, microstrip trace lengths between the coupler and microstrip feed lines traces between the ports and the coupler. Finally, the gain profile was optimized by increasing the height of the patch substrates.

Although the process was somewhat linear, it should be noted that these performance criteria often conflicted with one another. For example, impedance matching can be maximized over a larger range, but this impacted the gain profile and AR performance. Design compromises were required to be able to achieve an effective GNSS antenna design.

3.5 Fabrication Procedure

Antenna 1 was fabricated according to the following procedure. All laminates came prepared from the manufacturer with a 1 oz (35µm) copper layer on both sides. All undesired copper was removed such that only the microstrip traces and patches as part of Antenna 1 remained using an LPFK PCB prototype milling machine located at RMC. First, the bottom laminate, of height h_1, with the UWB BLC on one side and the slotted ground plane on the other side, were milled with a via hole $d_{\text{via}} = 0.6$ mm drilled to serve as part of the port 4 termination. Then, a simple piece of copper wire was cut to the appropriate length and copper tape was used to secure the wire and maintain an electrical connection between the ground plane and the port 4 terminating via-pad. Next, the two laminates of thickness 0.508 mm were prepared as the primary and parasitic patch layers respectively. Then four layers of 1.52 mm core laminate where the copper layers were completely removed with two of the layers having a notch cutout for placement and access to solder the SMA connector. The combination of the three laminates and three prepreg layers results in the substrate height of h_2.

Subsequently, all laminates layers had prepreg trace layers cutout and placed between one another other, using some stick glue to keep all the layers aligned while securing all layers under even distributed pressure using two steel plates. Then, to activate and cure the prepeg, the antenna rig was placed in an oven at room temperature and set to 200°C for approximately 90 minutes and was left to cool in the oven overnight. This was designed to emulate the steps of using a vacuum oven fabrication set-up that is listed by the manufacturer

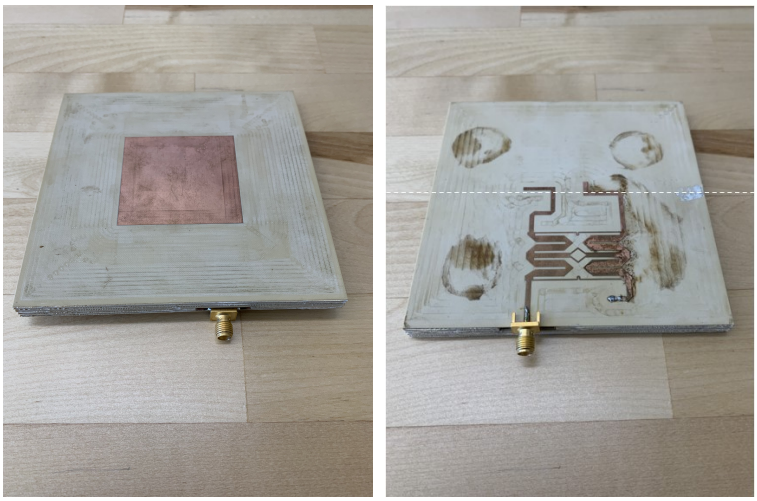

(a) **(b)**

Figure 3.9: Antenna 1 fabricated antenna (a) Top View (b) Bottom View

[42]. After the antenna was baked and the steel plates removed, the final steps required the soldering of an end launch SMA connector, a 50 Ω surface mount resistor terminating port 4 of the UWB BLC on the bottom side of the antenna. Pictures of the fabrication process can be found in Appendix A.

There were several issues that were identified as part of this procedure. The most significant was the orientation of the feed network with respect to the orthogonal slots. In fact, the feed network should have been mirrored along the x-axis, or white dotted line in Fig. 3.9(b) bisecting the antenna. In the LPKF milling machine, the laminate board could only be flipped in one direction. Since the .dxf files for both the feed network and the orthogonal slots were captured in the same orientation in HFSS, when the laminate board was flipped over, the feed network was now mirrored as noted earlier, leading to the reversal in antenna polarization. For future projects, it is important to ensure that if two sides of the same laminate are being prepared with respect to one another that the proper orientation is captured in the simulation model prior to fabrication.

Other minor issues included pressure not being evenly distributed across the entire antenna assembly which led to a 2 mm deflection in the antenna when measured between opposite corners. Also, the glue bled through the substrate leading to some residue in on the

bottom of the BLC substrate. As a result, this may have changed the electrical properties of the antenna. Top and bottom images of the fabricated Antenna 1 are captured in Fig. 3.9.

3.6 Experimental Set-up

All antenna testing for this thesis was conducted inside the RMC anechoic chamber and microwave lab utilizing an Agilent N5244A PNA-X Network Analyzer (PNA). After electronically calibrating the PNA, the $|S_{11}|$ measurements were completed outside of the chamber, sweeping over 121 frequencies between $1.1 - 1.7$ GHz. Those experimental results were compared to HFSS simulation results of the same number of sample frequencies.

Once the IBW was confirmed, the antenna pattern measurements were conducted in the anechoic chamber. This process followed a standard two antenna setup, as illustrated in Fig. 3.10, to verify the radiation pattern and the AR over the GNSS L-band. These results were also sampled using the same frequency sweep for the $|S_{11}|$ measurement. This sample size number was chosen as it was the lowest number of sampled frequencies that yielded a smooth curve while the far-field measurements could be specifically captured at each of the frequencies of interest, 1.18 GHz, 1.25 GHz, and 1.575 GHz.

Prior to conducting measurements, the PNA and chamber were calibrated using a S_{21} response and two identical wideband horn antennas with known gain. The process essentially sets the $|S_{21}|$ measured by the PNA to 0 dB across the calibrated frequency range. After calibration, one of the horns was replaced with the AUT for pattern measurements. The gain could then be calculated based upon the known gain of the calibration horn through subtraction of the two gain profiles also known as the substitution calibration method [5].

To conduct the antenna radiation pattern measurements, both of the two standard radiation cuts, $\phi = 0^\circ$ and $\phi = 90^\circ$ were required. To acquire this data, the AUT was set to boresight, $\phi = 0^\circ = \theta = 0^\circ$ and the source antenna which could only be rotated in the polarization angle γ was initially set to 0°. Then the AUT was swept from $-90^\circ \leq \theta \leq 90^\circ$. This process was then repeated after the AUT was rotated to $\phi = 0^\circ$ and the source antenna horn was rotated to $\gamma = 90^\circ$. The last measurement was for AR. This required that the

source antenna and AUT be set to boresight. Then, the source antenna was swept from $0 \leq \gamma \leq 180^{\circ}$, in 1° increments. References to experimental set-up can be found in Fig. 3.10.

After the required measurements were conducted in the anechoic chamber, the gathered data was exported to another computer where it could be processed. Specifically for AR, the difference in the highest and lowest $|S_{21}|$ value at each frequency were found across the entire range of γ. The highest and lowest values are then subtracted, which is commensurate with the ratio of the major and minor axes of an ellipse, in other words, the AR of the antenna as noted in (2.8) on page 16.

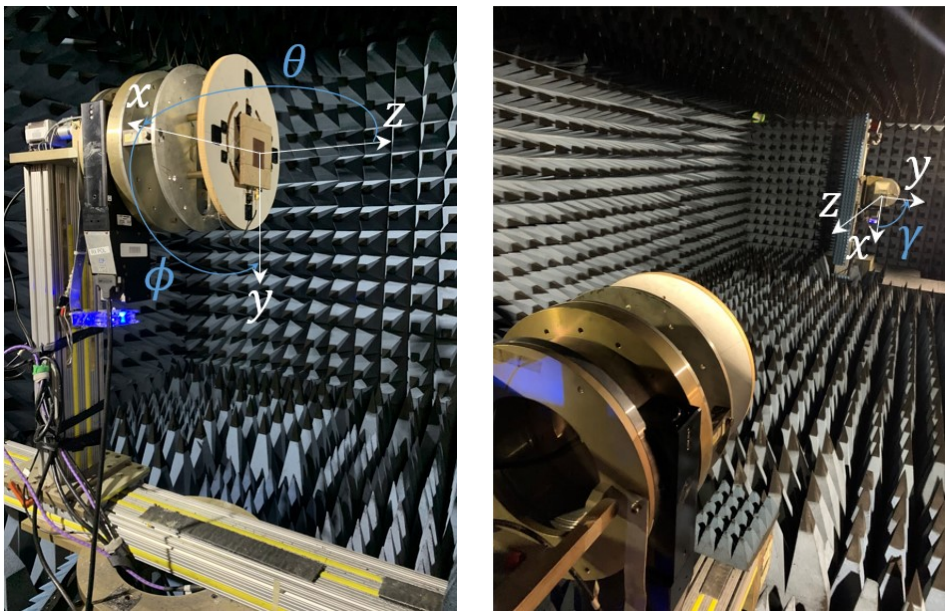

(a) **(b)**

Figure 3.10: Experimental test set-up with orientations (a) Antenna 1 AUT (b) Source Horn antenna

Initially it was unclear whether the RHCP and LHCP gains could be confirmed as the horn antennas only capture the total linear gain in dBi. However, one RHCP and two LHCP wideband spiral antennas, with known gain, were found to be available for use in the chamber as shown in Fig. 1.2. Therefore, the tests were completed again using these CP antennas. Since there was only one RHCP spiral antenna, only the LHCP spiral calibration data was used for both LHCP and RHCP gain measurements. This assumption was supported by the

fact that according to the data sheets, the gain and axial ratio of the antennas are virtually identical [43][44], simply with reversed polarizations. Lastly, the entire radiation pattern could not be captured for several reasons. First, due to the lack of clearance in the chamber, the AUT positioner would not have been able to complete a full 360° sweep in the elevation plane. Second, as there are many reflective surfaces at the rear of the AUT positioner, it was decided to limit the radiation pattern measurement to $-90° \leq \theta \leq 90°$.

3.7 Results and Discussion

First, the IBW was measured using the PNA prior to chamber measurements. The results shown in Fig. 3.11(a) with have a good match, only with a small shift in frequency in comparison to the simulated results. In this case, the measured IBW for the antenna is $> 40\%$.

Second, the simulated antenna gain is shown in Fig. 3.11(b). The measured $G_{\min} > 2.24$ dBic over the entirety of the GNSS L-band. The results are very similar, but with reversed gain profiles with respect to frequency, likely due to inaccuracies in modelling of the antenna, especially that of the prepreg. However, what should be apparent is the measured results are LHCP. This is due to the feed network being mirrored along the x-axis with respect to the orthogonal slots. However, it is assumed that if the feed network was in the proper orientation, the performance of the antenna would be identical apart from the change in polarization. Therefore, as Antenna 1 meets the $G_{\min} > -10$ dBi minimum metric, and with a gain drop of 3 dB, thus the GBW $\approx 38\%$, extending across the entire L-band.

Third, in Fig. 3.11(c) the measured AR performed well relative to the simulations even exhibiting a very similar profile. However, the measured results show that the AR > 3 dB in the middle and upper boundary of the L-Band. The simulated ARBW is $> 41\%$ between extending beyond the L-band, while the measured AR is 20% exhibiting a more dual-band response. Nevertheless, almost all GNSS satellite services are still within the measured ARBW of the fabricated antenna except for the G1 GLONASS frequency band.

Next, the simulated and measured RHCP/LHCP radiation patterns are shown in Figs.

3.12-3.13 in the $\phi = 0°$ cut and Figs. 3.14-3.15 in the $\phi = 90°$ cut with a summary of results in Table 3.3. These experimental results show similarity between simulated and measured results. The simulated HPBW of Antenna 1 was found to be less than minimum HPBW, 100° for GNSS applications, ranging between $89° - 97°$, whereas the measured HPBW value ranges between $57° - 116°$. Again, the RHCP and LHCP radiation patterns are reversed because of the incorrect orientation of the feed network with respect to the orthogonal slots. Furthermore, simulations suggested that the FBR > 10 dB, however, due to the limitations of the chamber set-up, this value could not be confirmed experimentally.

Table 3.3: SRA radiation pattern summary

	Freq	1.18 GHz		1.25 GHz		1.575 GHz	
Parameter	ϕ Plane	0°	90°	0°	90°	0°	90°
HPBW	Simulated	90°	97°	90°	93°	89°	89°
	Measured	57°	92°	92°	88°	116°	115°
Peak Gain Offset from Boresight	Simulated	-3°	-1°	-3°	-1°	1°	1°
	Measured	1°	0°	-4°	-4°	-3°	25°

Another issue that is apparent is that there is instability in the direction of maximum gain and therefore the radiation pattern. In simulations, the maximum of the main lobe varies moderately ±3° in both $\phi = 0°$ and $\phi = 90°$ planes. The measured results were much different with the direction of maximum gain. Although the results in the $\phi = 0°$ plane are similar to those simulated, with the main lobe varying only $1° - 4°$, except at 1.575 GHz in the $\phi = 90°$ plane where the peak gain is shifted to 25° from boresight.

Possible sources of error could include the modelling of the final fabricated antenna, especially the prepreg material, may not have been as precise as expected. Another source could be the fabrication process. The preparation and processing of the prepreg was emulated as best as possible with the specs that were provided by the manufacturer. However, those instructions are intended to be used in temperature-controlled vacuum oven, where the fabrication is carried out using pressure plates and a conventional oven. As such, the pressure may not have been evenly distributed across the entire element leading to minute changes in height throughout the device. In fact, there is a slight curvature in the antenna with a deflection of 2 mm when measured diagonally corner to corner.

In addition, as part of the experimental set-up, the antenna was rigged against the mounting plate, as the bottom of antenna was pressed up against several rubber stoppers which may have been on some of the microstrip traces, affecting the velocity of the guided waves to the antenna elements. Also, fishing line was used to secure the antenna around the patch element which could have impacted results. Finally, some of the stick glue that was used to hold the antenna in place while it was being prepared for the oven bled through the bottom element which may have affected the electrical properties of antenna element.

A summary of Antenna 1 results in comparison to GNSS performance requirements are detailed in Table 3.4. Note that the asterisk (*) notes that the value is an average of all measured radiation plots at 1.18 GHz, 1.25 GHz, and 1.575 GHz in both $\phi = 0°$ and $\phi = 90°$ azimuth plane cuts.

Table 3.4: Antenna 1 Summary of Performance vs. GNSS performance requirements

Parameter	GNSS Performance Requirement	Measured Antenna Performance
IBW	$> 30\%$	$> 40\%$
ARBW	$> 30\%$	20%
GBW	$> 30\%$	38%
HPBW	$100° \leq \theta \leq 140°$	74°*
Long Dimension	< 120 mm	115 mm
Height	< 10 mm	8.74 mm

3.8 Summary

This chapter covered the methodology of the antenna design including the UWB BLC feed network. The fabrication process and experimental set-up of Antenna 1 are also detailed. It was discovered that the multi-layer fabrication using core laminates and prepreg could be conducted entirely at RMC, achieving good performance that compare well to simulated results and GNSS requirements. In fact, the gain, IBW and ARBW performance of the fabricated antenna is comparable to existing microstrip antenna found during the literature review without resorting to the use of a QFN, probes or air gaps. The radiation pattern also performed well apart from the limited HPBW found in the $\phi = 0°$ plane at 1.18 GHz

and reversed antenna polarization due to the improper orientation of the feed network with respect to the orthogonal slots. Sources of error in the measured results could be the result of modelling, fabrication design, or with the experimental set-up. Finally, this design is comparable in size to current state-of-the-art designs, however it is in excess of the $\lambda_0/2$ inter-element spacing requirement at the upper limit of the L-band. Therefore, additional effort will be required to integrate this design into an array. Nonetheless, the simulated results of this antenna design provided the confidence to attempt to design a PCB integrated antenna in the next chapter and subsequently as an element in an array in Chapter 5.

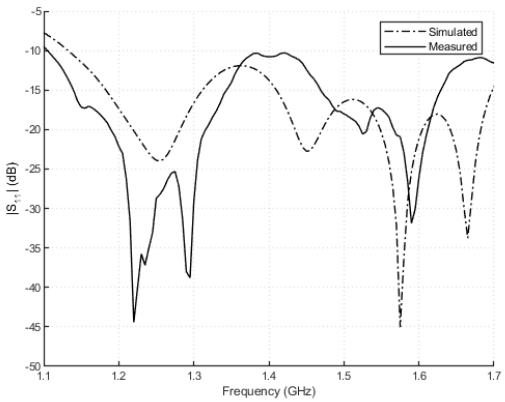

(a)

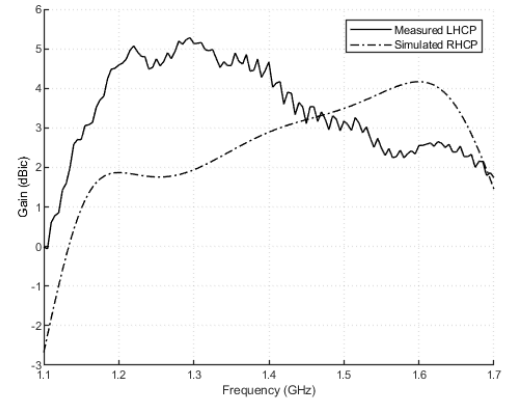

(b)

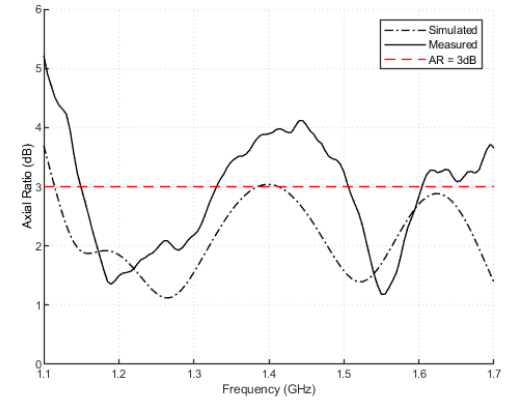

(c)

Figure 3.11: Simulated vs. measured results with respect to frequency (a) $|S_{11}|$ (b) Gain (c) Axial ratio

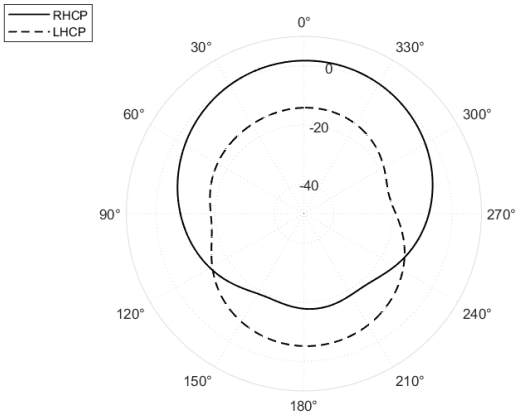

(a)

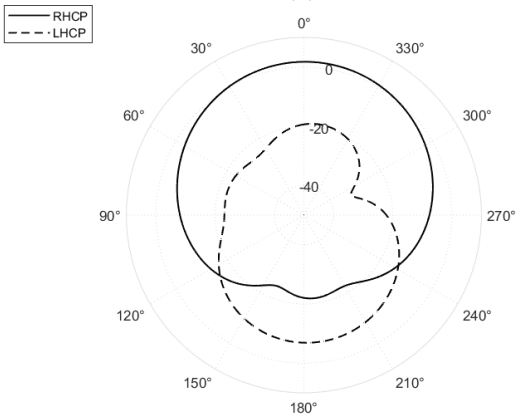

(b)

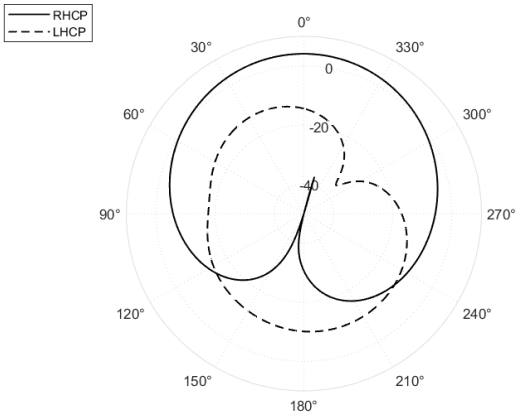

(c)

Figure 3.12: Simulated radiation pattern in $\phi = 0°$ plane (a) 1.18 GHz (b) 1.25 GHz (c) 1.575 GHz

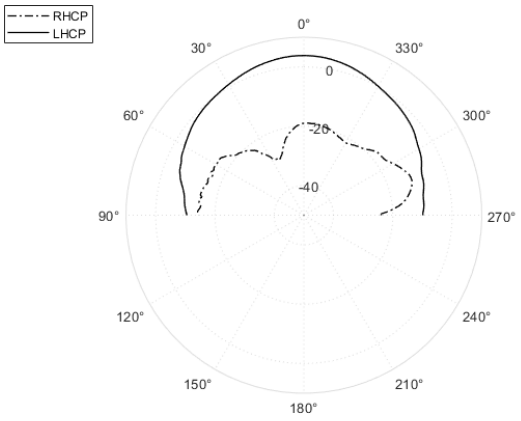

(a)

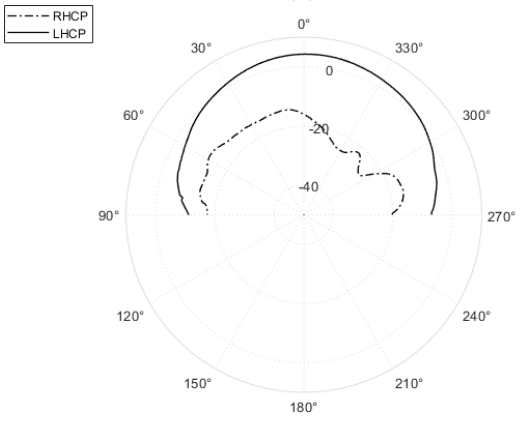

(b)

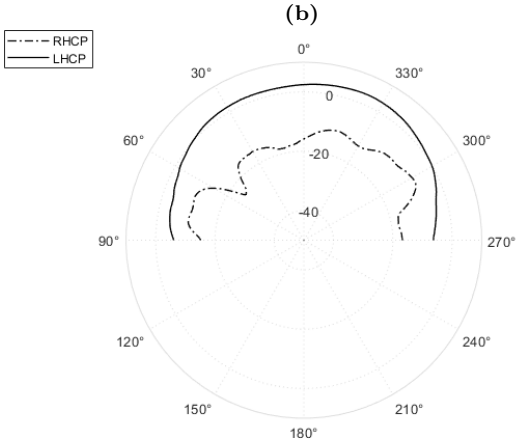

(c)

Figure 3.13: Measured radiation pattern in $\phi = 0°$ plane (a) 1.18 GHz (b) 1.25 GHz (c) 1.575 GHz

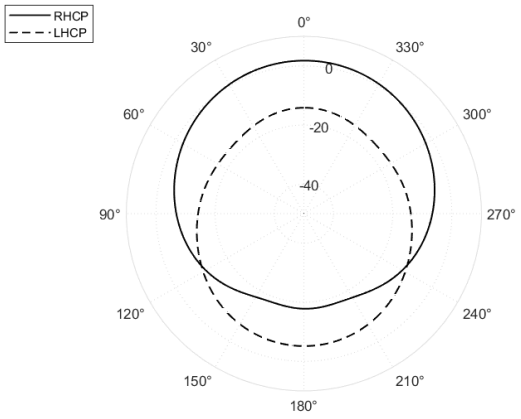

(a)

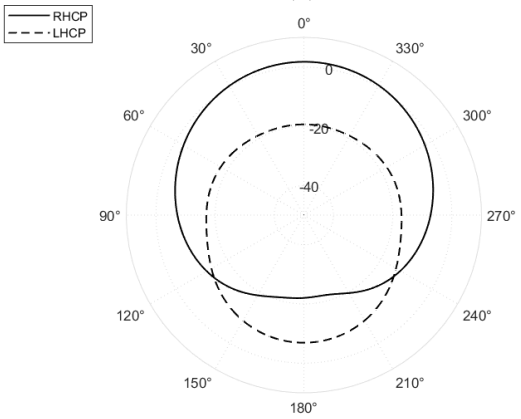

(b)

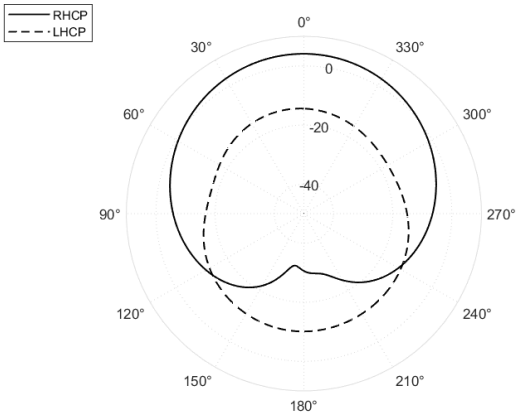

(c)

Figure 3.14: Simulated radiation pattern in $\phi = 90°$ plane (a) 1.18 GHz (b) 1.25 GHz (c) 1.575 GHz

(a)

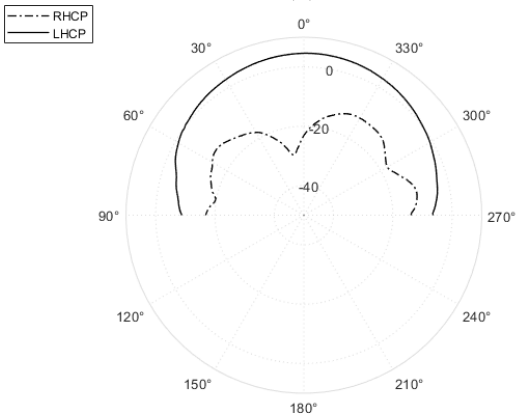

(b)

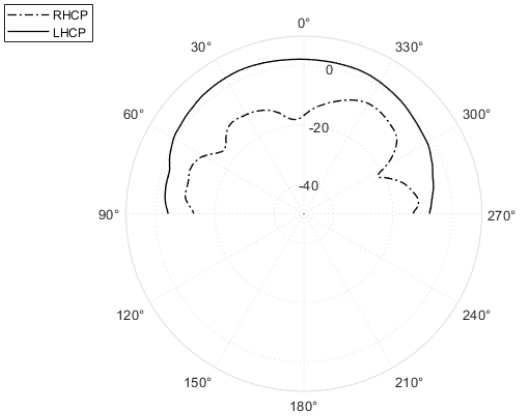

(c)

Figure 3.15: Measured radiation pattern in $\phi = 90°$ plane (a) 1.18 GHz (b) 1.25 GHz (c) 1.575 GHz

Chapter 4

GNSS Aperture Coupled Integrated Printed Circuit Board Antenna

4.1 Introduction

This chapter presents information regarding the GNSS aperture-coupled PCB integrated antenna, Antenna 2. This design path was initially the intended focus of this thesis. However, this study was curtailed as there were significant concerns that substantive results would have extended the time frame of this thesis beyond what was available. Nevertheless, it is important to provide an overview the investigation into the development of this PCB integrated design and the findings that were found as part of a larger discussion.

It should be noted that the results presented in this chapter are preliminary and would require further investigation to understand the best way forward with this research. The remainder of this chapter includes a description of the antenna integrated PCB design model, some preliminary simulation results and discussion.

4.2 Antenna 2 Design

The antenna design presented is based upon an early version of Antenna 1. This design aims to incorporate a stripline layer between the radiating aperture and the microstrip layer in

an attempt to reduce the size of the antenna by utilizing more of the area at the center of the antenna. However, what may be a more attractive feature of this design is to reduce the amount of back radiation that is inherent when using an aperture-coupled patch excitation method. This is key if such an antenna is to be integrated in a PCB stack-up that includes RF components such as LNAs and reconfigurable switches. Like the strategy with Antenna 1, the intent was to use a uniform permittivity substrate throughout the antenna, in an effort to balance antenna size and performance.

The current version of Antenna 2 is shown in Fig. 4.1. It features the UWB BLC found on the microstrip layers as part of Antenna 1. Then there are two microstrip-to-stripline transitions as part of the feed lines which are coupled to the orthogonal slots and the rest of the radiating aperture.

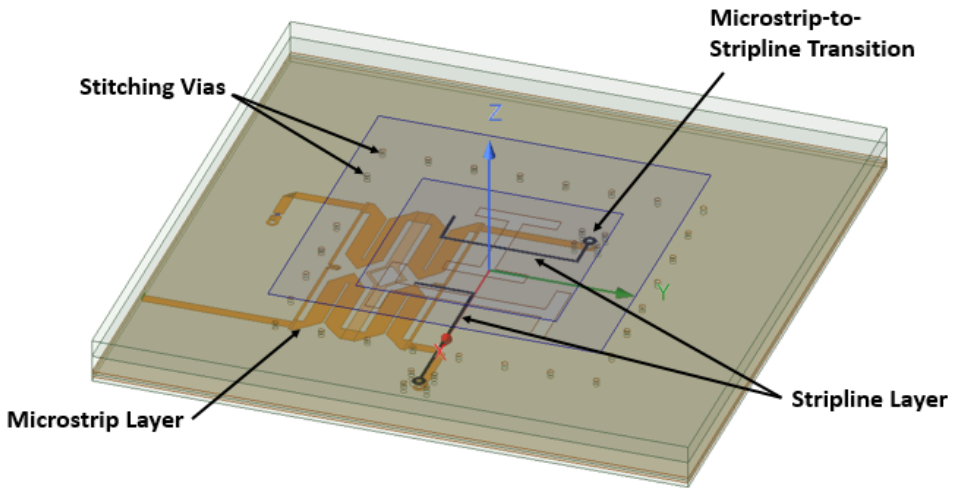

Figure 4.1: Antenna 2 HFSS model

The microstrip layer substrate h_1, the primary and parasitic patches substrate layers h_3, as noted in Fig 4.2 are designed with the same substrate properties and thickness as that in the Antenna 1. However, it is the introduction of the stripline layer that is a significant departure from all other proposed antenna models in this thesis, and is based on the antennas found in [1] and [6]. This layer is sandwiched between two laminates and two ground planes. The stripline traces couple with the radiating aperture as opposed to the microstrip traces

that are coupling with the radiation apertures of Antenna 1. A full annotated description of Antenna 2 is provided in Figs. 4.2-4.4 and Tables 4.1-4.3.

The microstrip-to-stripline via transition that is shown in Fig. 4.3 features a 50 Ω microstrip impedance to a 41.8 Ω stripline characteristic impedance. Additionally, the stitching vias are located between the ground planes at the edges of the parasitic patch. They serve two purposes in this model. First, to ensure that the two ground planes are at the same potential to mitigate the effects of the fundamental parallel-plate waveguide mode. Second, these vias also are designed as an EM fence to mitigate effects of mutual coupling between elements in an array configuration with the addition of the stripline layer. Note, all via-holes for the signal, return and stitching vias are the same diameter, d_{via}

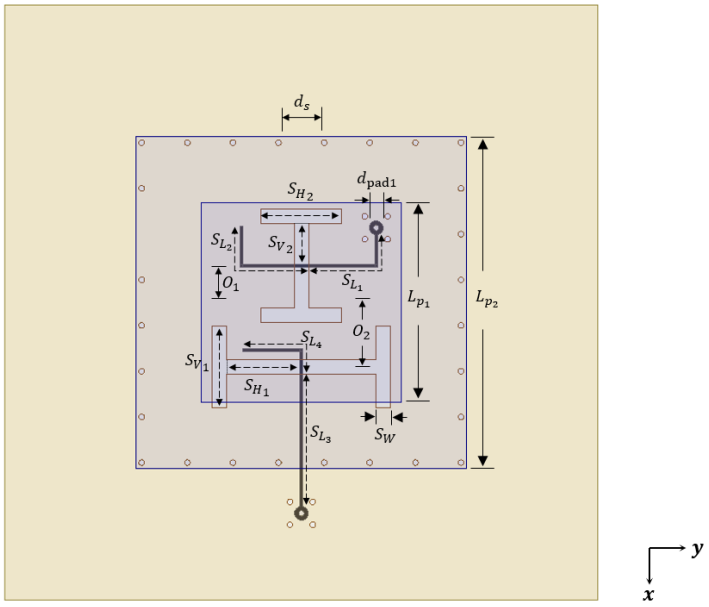

Figure 4.2: Antenna 2 top view

Table 4.1: Antenna 2 top view dimensions

Parameter	Dimension (mm)	Parameter	Dimension (mm)
d_{pad_1}	1.2	S_{H_2}	12.86
d_s	8	S_{L_1}	17.38
d_{via}	0.6	S_{L_2}	18.69
L_{p_1}	34	S_{L_3}	23.21
L_{p_2}	58	S_{L_4}	14.45
O_1	6.44	S_{V_1}	7.17
O_2	11.25	S_{V_2}	14.31
S_{H_1}	5.85	S_W	2.5

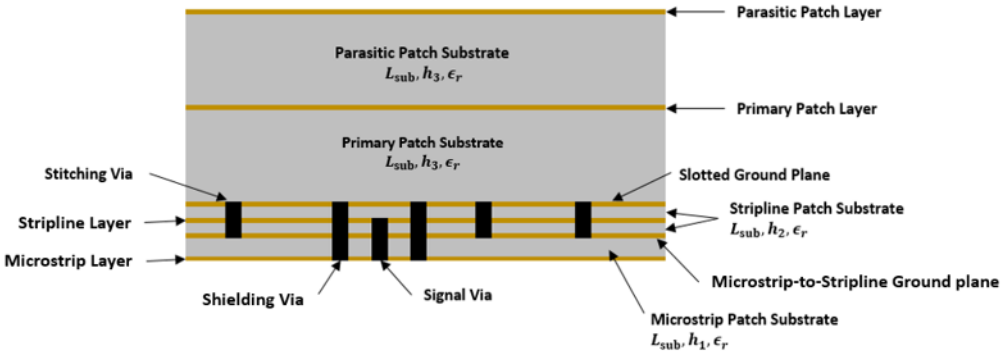

Figure 4.3: Antenna 2 side view

Table 4.2: Antenna 2 side view dimensions

Parameter	Dimension (mm)
ϵ_r	3.45
h_1	0.5
h_2	0.76
h_3	3.8
L_{sub}	104

Table 4.3: Antenna 2 bottom view dimensions

Parameter	Dimension (mm)	Parameter	Dimension (mm)
D	4.8	M_{L_4}	19.07
d_{pad2}	2	M_{L_5}	4
L_{sub}	104	O_3	25.41
M_{L_1}	25.71	r_{slot}	1.5
M_{L_2}	17.5	W_1	1.74
M_{L_3}	18.82	W_2	0.54

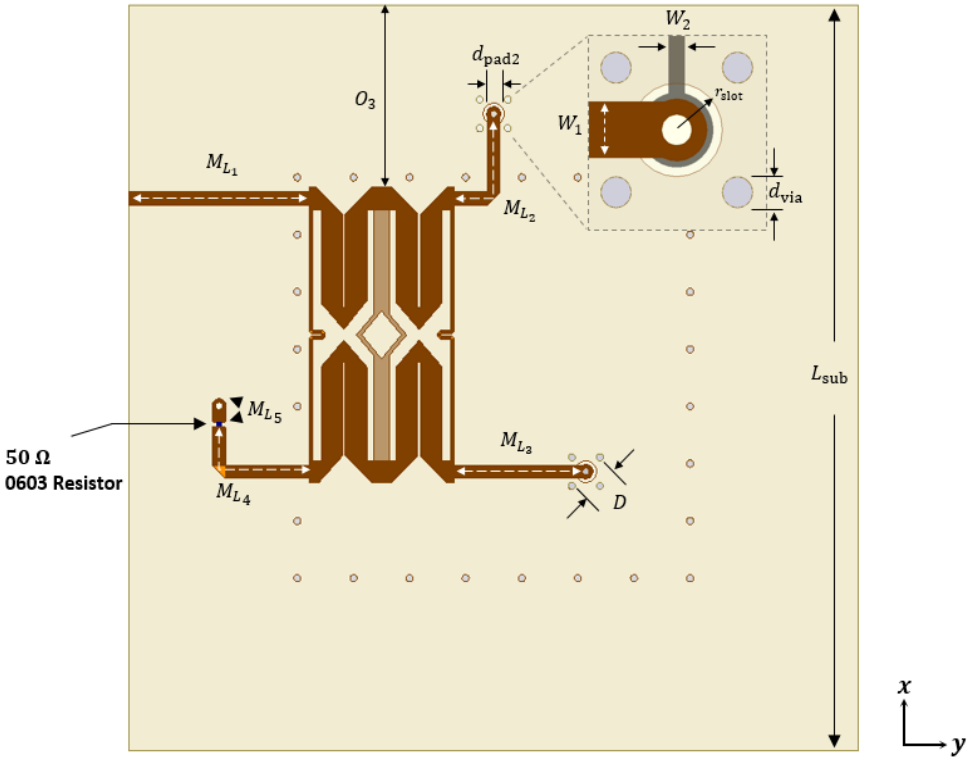

Figure 4.4: Antenna 2 bottom view

4.3 Simulation Results

The simulated results of this PCB integrated design are preliminary and suggest that further investigation is required. The simulated $|S_{11}|$ results of Antenna 2 captured in Fig. 4.5(a) indicate good matching in reference to the input of the antenna. However, the AR and gain shown in Fig. 4.5(b)-(c) describe two of the significant issues of this antenna. One, the gain is significantly lower than that of Antenna 1. Separate electric field analysis of the antenna denotes that the issue was primarily between the stripline traces and the radiating aperture where almost no electric fields existed on either the primary or parasitic patches. The second issue is the instability of the AR. Although the AR < 3 dB over some parts of the GNSS L-band, the AR has two spikes suggesting that the AR is nearing linear polarization within the GNSS L-band.

Initially it was unclear why this was the case but after studying the optimized radiation patterns of Antenna 1, the LHCP radiation was directed backwards as shown in Figs. 3.12 and 3.14 which appear to be reversed in comparison to the Antenna 2 patterns in Figs. 4.6 and 4.7 respectively. This information suggests that this LHCP is being significantly affected by the introduction of the stripline layer, especially, the microstrip-to-stripline ground plane.

Finally, as a means of fault-finding, a graph of the ratio of the total gain over the total directivity, or the efficiency of the antenna is illustrated in Fig. 4.8. As can be seen in the results, the antenna is operating below 16% efficiency over the entire band with a minimum efficiency of approximately 1% in some parts of the band. For all intents and purposes, almost none of the energy that is available at the antenna input will be able to be radiated out.

4.4 Summary and Potential Future Work

The design of the Antenna 2 is still in the preliminary steps, however, there are possible avenues of future investigation. Although the impedance matching appeared to be suitable, the modifications required to improve the overall performance will likely require further attention to the $|S_{11}|$. Second, understanding why the introduction of the stripline layer

caused the decline in antenna performance is imperative to confirm whether this antenna could meet its intended objectives. Another possible investigation is to understand what is happening within the stripline layer, perhaps through use of modal analysis. Lastly, an investigation to understand the source of the polarization issues and how they can be optimized for GNSS wideband applications.

This chapter has included an overview of a PCB integrated design that was an initial focus of this thesis. However, due to the significant amount of time that would been required to complete this design to a satisfactory level was beyond what was available, it was therefore was no longer pursued. In its place, the study of a 2×2 GNSS SRA based on a modified version of Antenna 1.

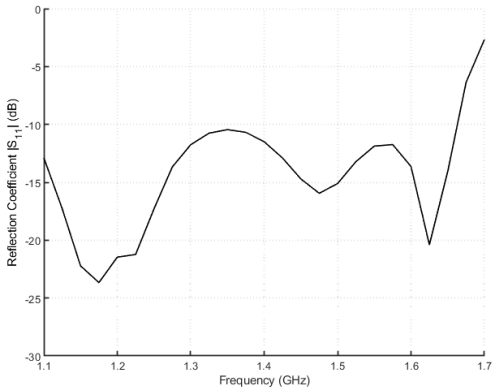

(a)

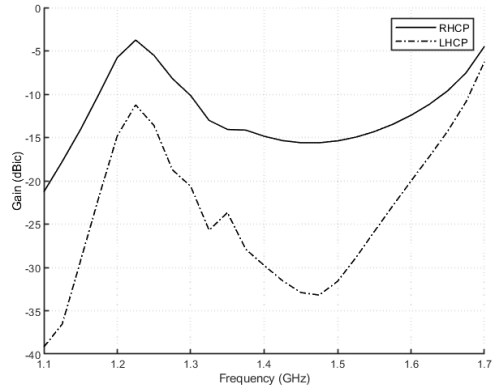

(b)

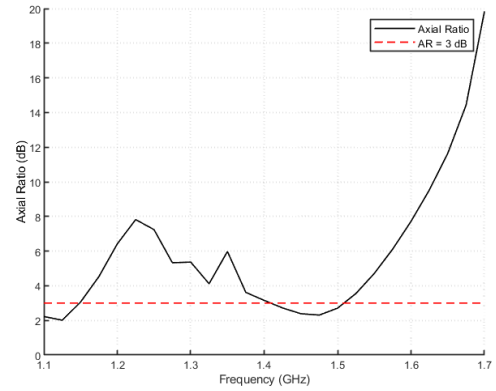

(c)

Figure 4.5: Antenna 2 simulated results with respect to frequency (a) $|S_{11}|$ (b) Gain (c) Axial Ratio

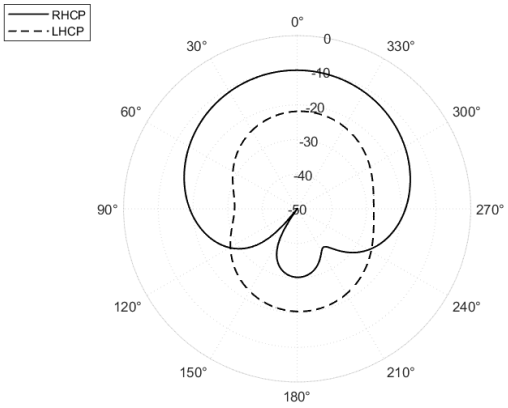

(a)

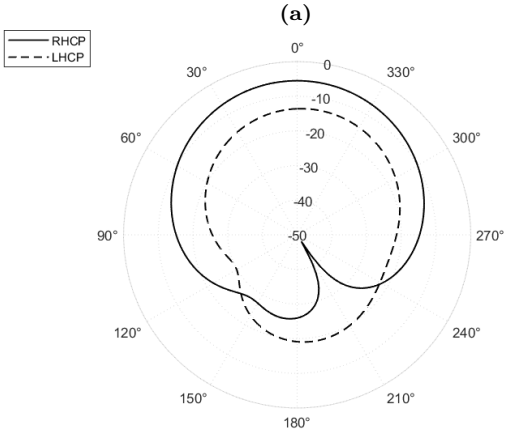

(b)

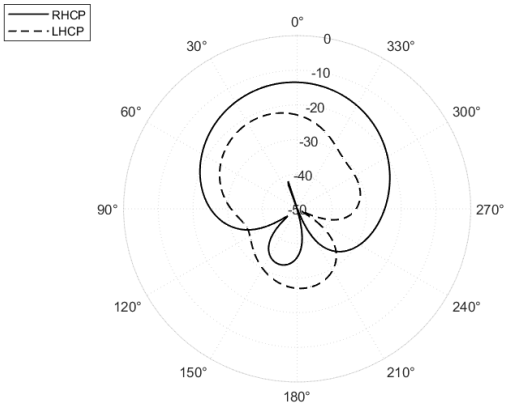

(c)

Figure 4.6: Antenna 2 simulated results $\phi = 0°$ plane (a) 1.175 GHz (b) 1.25 GHz (c) 1.575 GHz

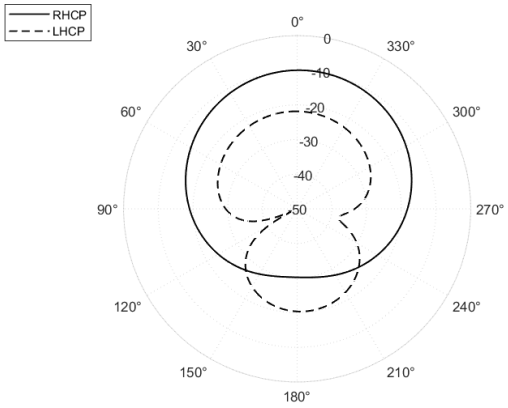

(a)

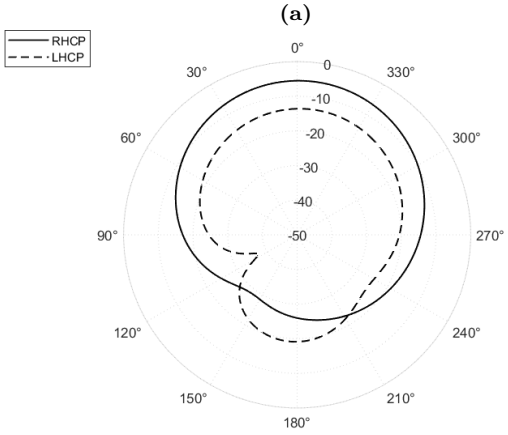

(b)

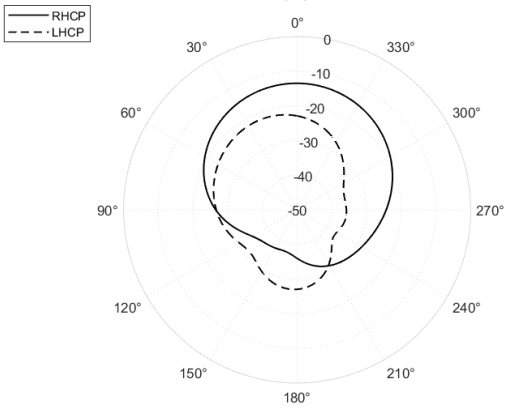

(c)

Figure 4.7: Antenna 2 simulated results $\phi = 90°$ plane (a) 1.175 GHz (b) 1.25 GHz (c) 1.575 GHz

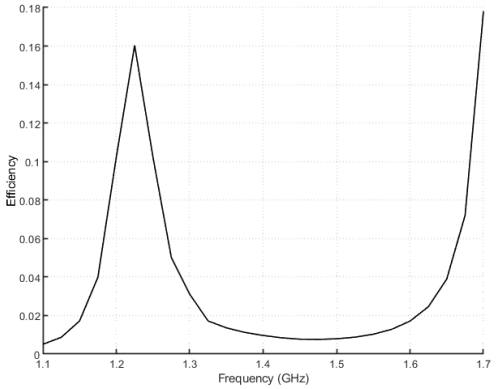

Figure 4.8: Antenna 2 simulated efficiency

Chapter 5

Investigation of a GNSS Stacked-Patch Antenna in a 2×2 Sequentially Rotated Array

5.1 Introduction

With the design of Antenna 1 complete, the focus was on the implementation of a wideband GNSS array. Although Antenna 1 was determined to be effective for standalone wideband GNSS antenna applications, small modifications were required to meet all the performance requirements of the array, specifically, GBW. The simulated in-band peak gain drop of Antenna 1 was found to be 2.5 dB. Although this was within the limits of the Antenna 1 design, it was expected that this would not be the case if implemented in an array. Results did confirm that when Antenna 1 was integrated into an SRA configuration, the peak gain drop was about 3 dB over the GNSS L-band as noted in Fig. 5.1. As such, Antenna 3, a modified version of Antenna 1 was integrated into an SRA to ensure optimal experimental results.

This chapter will cover the details of Antenna 3, followed by its implementation into a 2×2 SRA. The specifics of the design process, fabrication as well as simulated and measured results are included. There is also a discussion of simulated mutual coupling and antenna performance including gain, ARBW, and IBW of the antennas. Note that Antenna 3 was only simulated and not fabricated.

The fabrication of the SRA was similar to that of Antenna 1 although there was an

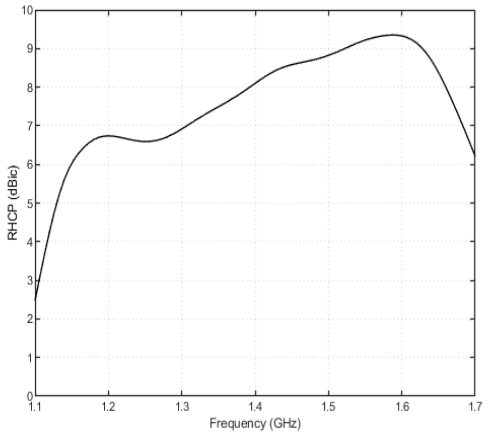

Figure 5.1: SRA antenna 1 simulated RHCP gain

obvious need for more substrate material, four ground vias and surface mount resistors, and the use of several C-clamps in the middle of the steel plates to apply even pressure as the SRA was much larger than Antenna 1. Also, the SRA was rigged differently to the AUT positioner mounting plate. Images of the fabrication process can be found in Appendix B. Also, like Antenna 1, as the issue of feed network orientation was not discovered until after the SRA was fabricated, the measured results show a similar performance with a reversal of the antenna polarization.

5.2 Antenna 3 Design

A bottom view of Antenna 3 is depicted in Fig. 5.2 and is very similar to Antenna 1. There were no changes made to the UWB feed network, patch, or substrate dimensions. However, to achieve a flatter peak gain response across the band, there were two other modifications required. One included resizing the I-slots in the ground plane. This did not have a significant impact on the $|S_{11}|$ of the system as shown in Fig. 5.3(a). However, it did have a positive response on the gain of the antenna with only 1.5 dB difference in peak gain drop as shown in Fig. 5.3(b). To optimize the ARBW, changes needed to be made to the size and location of the slots and tuning stubs on both I-slots. Ultimately, this antenna was able to achieve

all specifications except for ARBW, which exhibits more of a multi-band response as the AR $>$ 3 dB over two bands with a maximum AR of 3.4 dB at 1.36 GHz as illustrated in Fig. 5.3(c). This antenna was not fabricated to confirm validity of results due to limited substrate material available for use.

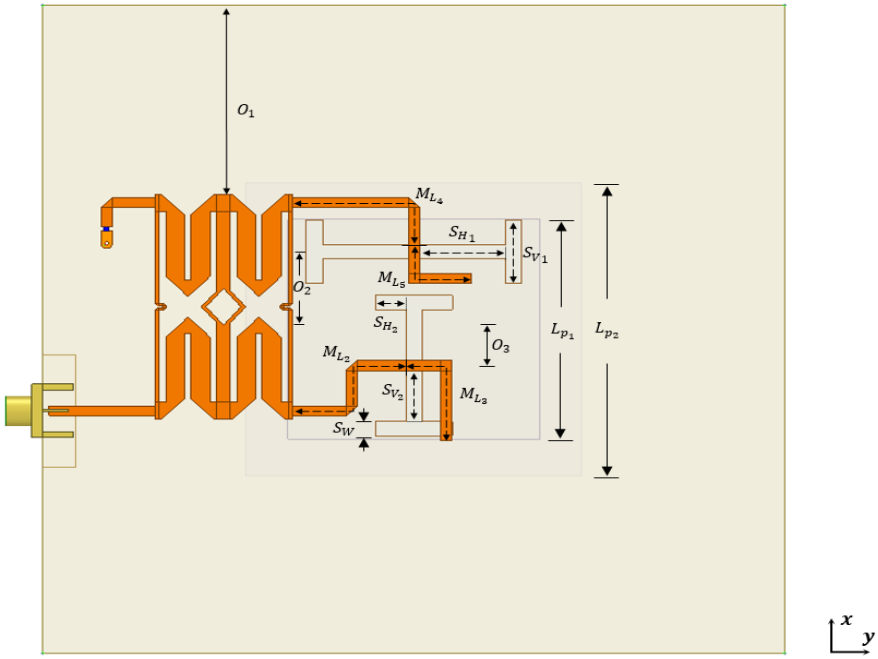

Figure 5.2: Bottom view of Antenna 3 design

Table 5.1: Antenna 3 dimensions

Parameter	Dimension (mm)	Parameter	Dimension (mm)
L_{p_1}	52	O_1	33.57
L_{p_2}	39	O_2	13.76
M_{L_2}	25.67	O_3	6.43
M_{L_3}	19.66	S_{H_2}	3.5
M_{L_4}	26.3	S_{V_2}	4.38
M_{L_5}	14.93	-	-

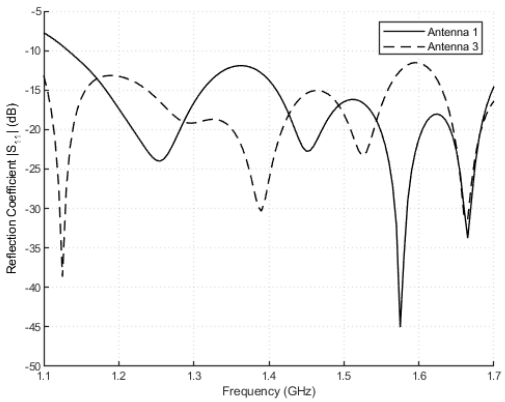

(a)

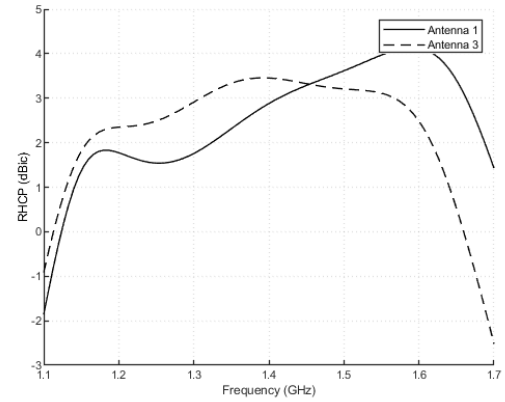

(b)

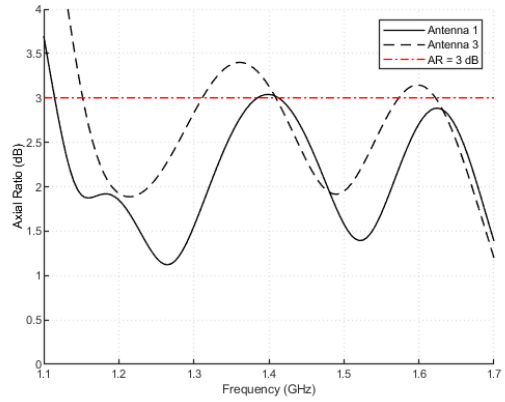

(c)

Figure 5.3: Antenna 1 vs. Antenna 3 comparison with respect to frequency (a) $|S_{11}|$ (b) RHCP Gain (c) AR

5.3 Sequentially Rotated Antenna Design

The SRA is composed of four elements of Antenna 3 in a 2×2 pattern. An exploded view is depicted in Fig. 5.4. The most difficult parameter to design was AR. For any antenna array design, symmetry is paramount, including the fact that each antenna element must be identical, and equidistant to neighboring antenna elements to ensure optimum performance. To generate RHCP, copies of Antenna 3 were rotated, counterclockwise around a center axis. This configuration also allows for easy access to each of the elements from the edge of the board if this antenna element were to be incorporated into a phased array configuration.

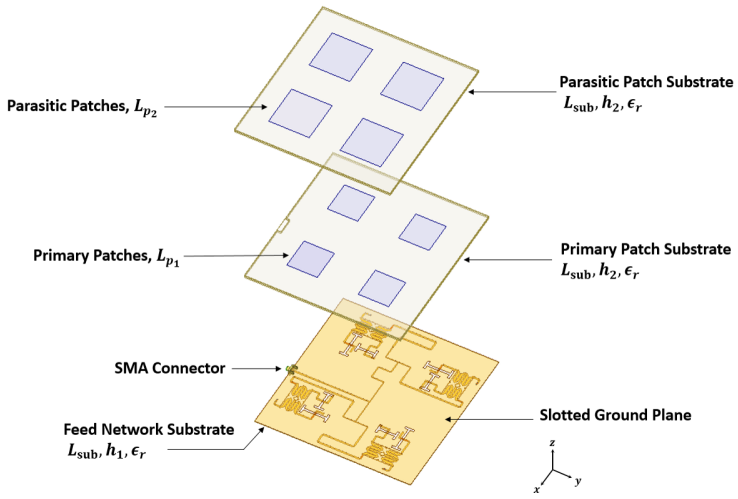

Figure 5.4: SRA exploded view

To fabricate this device, it was determined that the antenna had to be less than or equal to 210 mm × 210 mm in planar dimensions otherwise the antenna simply would not fit in the LPKF milling machine. Antenna 3 has an $L_{\text{sub}} = 115$ mm and thus the entire SRA substrate would be 230 mm in length. Therefore, L_{sub} needed to be decreased in size by at least 20 mm. Concurrently, the inter-element distance d_n was decreased to 80% of the original distance or 91.4 mm, which meets the $< \lambda_0/2 = 93.4$ mm requirement at the upper end of the GNSS L-band. This to some degree mitigates the back lobe radiation issues inherent in antenna array designs. The fabrication procedure is very similar to that of Antenna 1 except the SRA required four via holes be drilled and soldering of four surface mount resistors for each

of the four elements. To reduce the size of the antenna elements and fit the feed networks within the bottom layer of the antenna, the input port was modified so that it could meet the outputs of the array feed network as shown in Fig. 5.4. The simulation results of these modified elements were not captured as part of the SRA study and so it is unclear how the performance of these elements changed with the modification of the input traces.

5.3.1 Mutual Coupling

As discussed in Section 2.9.4, mutual coupling is the EM interaction between elements in an array that if not properly accounted for can significantly degrade its performance. The mutual coupling was managed by setting an appropriate distance between each of the elements. Although a mutual coupling is function of the active impedance of each element, if $|S_{21}| < -20$ dB is measured between neighbouring elements, this is considered an acceptable level of mutual coupling in array design [18].

A study was conducted by placing two elements orthogonal to each other as one half of the 2×2 SRA RHCP configuration as shown in Fig. 5.5(a). Originally, the elements were positioned almost half the entire SRA substrate away from each other. Then the inter-element spacing d_n was decreased to 90% and then 80% of the original distance while $|S_{21}| < -20$ dB.

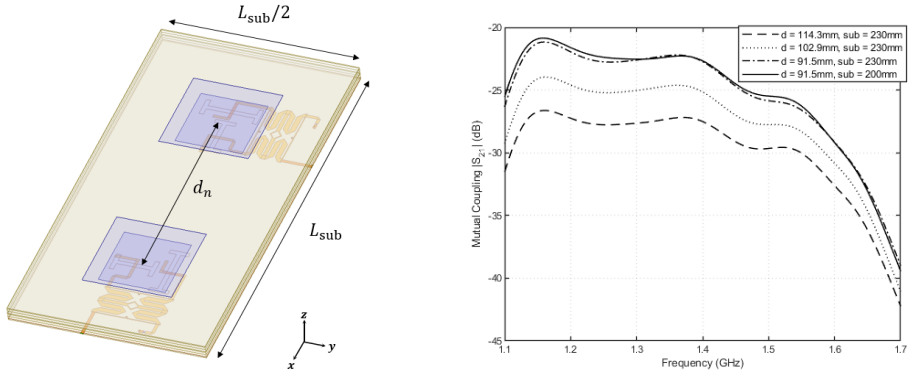

(a) **(b)**

Figure 5.5: SRA mutual coupling simulation (a) Model (b) Results

A complicating factor was the longest dimension of the SRA had to be < 210 mm to fit

in the LPKF milling machine. Fortunately, L_{sub}, was able to be decreased to 200 mm while maintaining the same distance, d_n between the elements. As can be shown in Fig. 5.5(b), the mutual coupling remained acceptable while also verifying that the entire SRA size met the $<$ 210 mm fabrication requirement.

5.3.2 Array Feed Network

In addition to the physical rotation of the antenna elements, the microstrip array network was designed with a progressive phase shift based on the SRA parallel feed network found at [34]. This feeding system comprises of three parallel T-junction sections arranged in a two-stage configuration as shown in Fig. 5.6. T-junctions were chosen as there was no need for additional features such as surface mount components or vias and could easily be used within the limited space available between antenna elements.

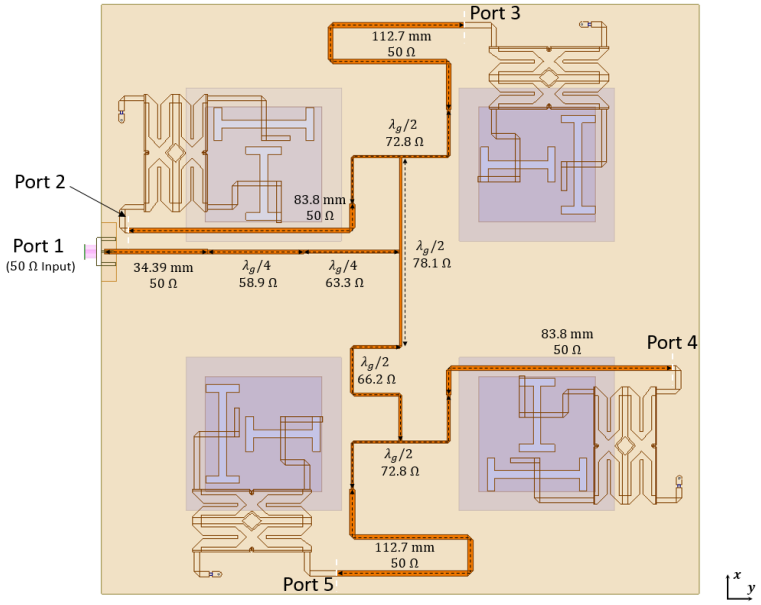

Figure 5.6: SRA feed network model (bottom view)

The first stage serves as an impedance matching section between the input port and the first T-junction where two-QWTs are used for wideband impedance matching. The second stage is an anti-phase equal power divider, generating a 180° phase difference between output

ports of stage 1. This requires the 78.1 Ω T-junction power divider, to be connected with two identical 72.8 Ω T-junction power dividers with the one connected to ports 4 and 5 at the output of the $\lambda_g/2$ or 180° delay line.

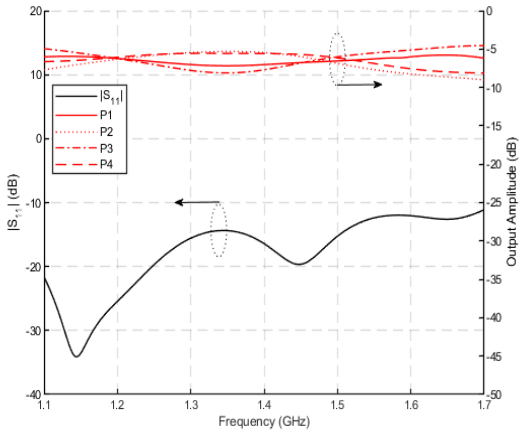

(a)

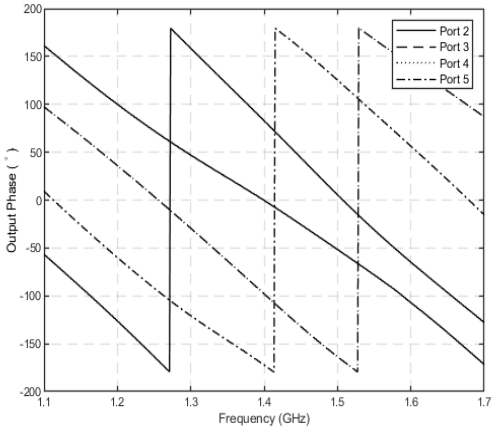

(b)

Figure 5.7: SRA feed network simulated results (a) $|S_{11}|$ and S-parameter port amplitude (b) S-parameter port phase

The third and final stage has 50 Ω feed lines connecting to each of four output ports. The port 4, 50 Ω feed line, is $\lambda_g/4$ longer than port 3 line. By symmetry, the port 2 feed line which is identical to the port 4 feed line, is $\lambda_g/4$ longer than the port 1 feed line which is identical to the port 3 feed line. This feed network results in a progressive phase shift of

0° (port 2), 90° (port 3), 180° (port 4), and 270° (port 5) in the counterclockwise rotation when viewed from above.

To ensure symmetry in this array feed network, the input port was offset by $\lambda_g/8$ so that the $\lambda_g/2$ delay line could be accommodated. Fig. 5.7(a) and (b) show the simulated output amplitudes and phases of the array feeding network respectively. The full-wave simulation results suggest that the array feed network is in a reasonable range for successfully exciting the 2×2 SRA.

Originally, λ_g, was designed to be 11.7 cm, corresponding to a mid-L-band frequency of 1.385 GHz and $\epsilon_r = 3.45$. However, when the feed network was integrated into the SRA, the $|S_{11}|$ appeared nearing the impedance matching limit at the lower end of the L-band. A parametric study of λ_g was conducted to improve impedance matching while maintaining the integrity of the progressive phase shift at each of the elements. Due to the improved IBW results, and other results revealed later in this chapter, it was decided that the λ_g would be increased to approximately 12.9 cm which corresponds to an $f_0 = 1.25$ GHz. Simulated results of this parametric study are shown in Fig. 5.8.

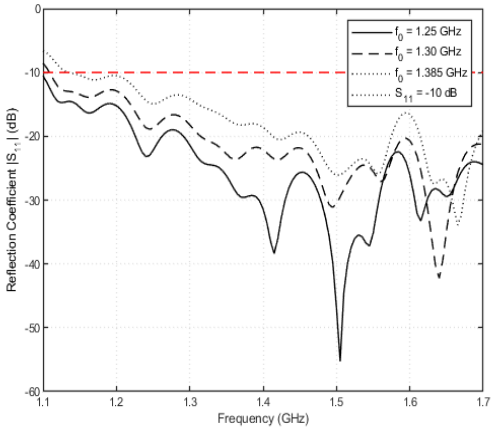

Figure 5.8: SRA feed network parametric λ_g analysis

5.3.3 Results and Discussion

The SRA substrate design is the same uniform permittivity as Antenna 1, except now with four elements in a 2×2 arrangement, instead of as a standalone unit. In addition, the experimental set-up of the SRA was very similar to that of Antenna 1. The simulated and measured $|S_{11}|$, AR, and gain are plotted versus frequency in Fig. 5.9(a)-(c) with an overall agreement between results. The simulated and experimental results show that SRA is very well impedance matched with an IBW $> 43\%$ with a $|S_{11}| \leq -12.7$ dB.

The ARBW for simulated and experimental results are $> 43\%$ covering the entire L-band with AR < 0.8 dB, while the AR < 2.2 dB when measured experimentally. Although the measured AR is below the AR limit across L-band, there is a spike centered around 1.48 GHz. Finally, the gain drops by approximately 1.97 dB over the entire L-band for simulated results and approximately 2.2 dB, between $5.5-7.7$ dBic for experimental results for an FBW $\approx 40\%$. The difference is that the measured gain is LHCP whereas the simulated gain is RHCP similar to measured results from Antenna 1. As such, it was assumed that the RHCP results would be identical in performance. Therefore, there is good agreement between the simulation and experimental results. Furthermore, these results are comparable to the SRA in [22], with the gain about 25% less RHCP gain while being 67% smaller in area and and 77% shorter in height.

Figs. 5.10 and 5.11 illustrate the simulated and measured radiation patterns at 1.18 GHz, 1.25 GHz and 1.575 GHz in the $\phi = 0^\circ$ plane while Fig. 5.12 and 5.13 show the simulated and measured radiation patterns at the same frequencies in the $\phi = 90^\circ$ plane. A summary of the results is available in Table 5.2. These experimental results show good agreement with the simulated radiation pattern results albeit with a reversed polarization.

Table 5.2: SRA radiation pattern summary

	Freq	1.18 GHz		1.25 GHz		1.575 GHz	
Parameter	ϕ Plane	0°	90°	0°	90°	0°	90°
HPBW	Simulated	67°	67°	65°	63°	60°	50°
	Measured	61°	48°	59°	60°	55°	45°
Peak Gain Offset from Boresight	Simulated	7°	-2°	4°	-1°	-3°	-1°
	Measured	-5°	0°	-5°	6°	3°	-2°

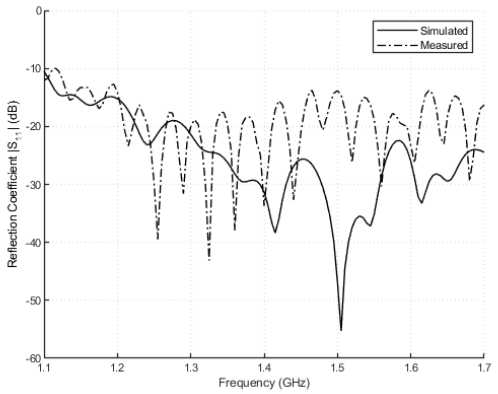

(a)

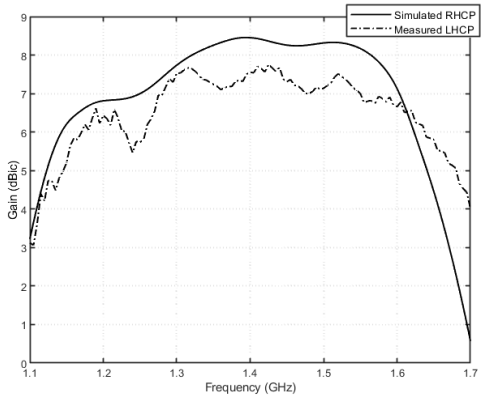

(b)

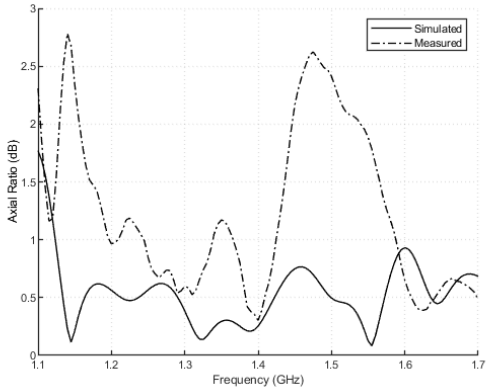

(c)

Figure 5.9: Experimental vs. simulation results of GNSS 2×2 SRA (a) S_{11} (b) Gain (c) Axial Ratio

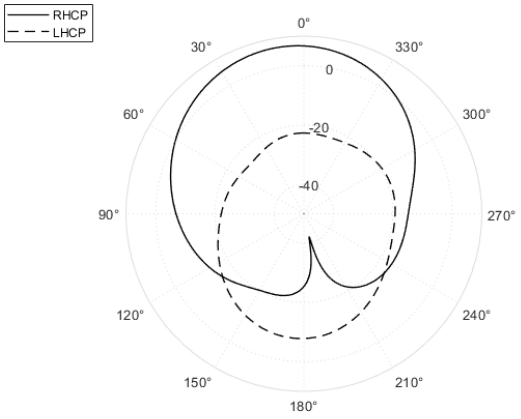

(a)

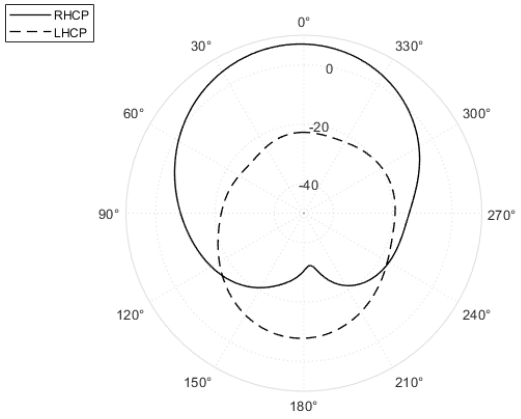

(b)

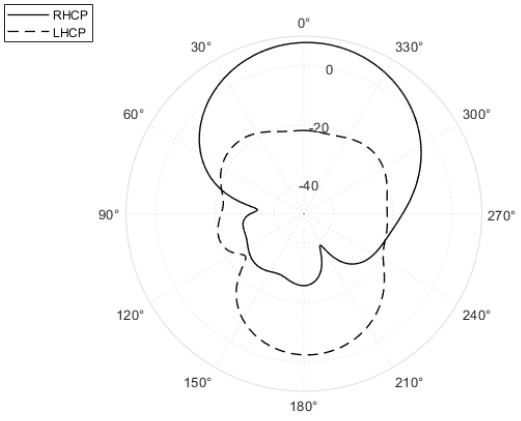

(c)

Figure 5.10: Simulated SRA radiation pattern in $\phi = 0°$ plane (a) 1.18 GHz (b) 1.25 GHz (c) 1.575 GHz

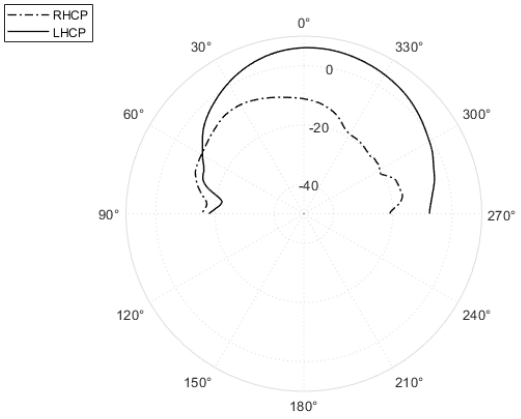

(a)

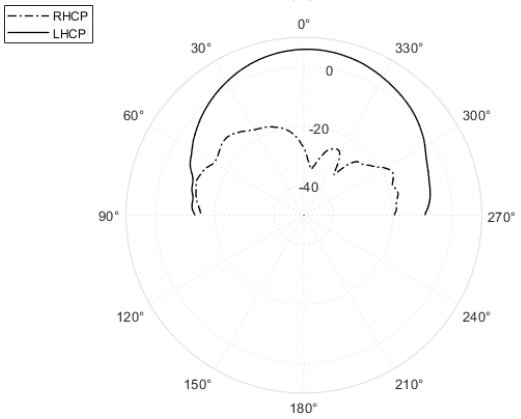

(b)

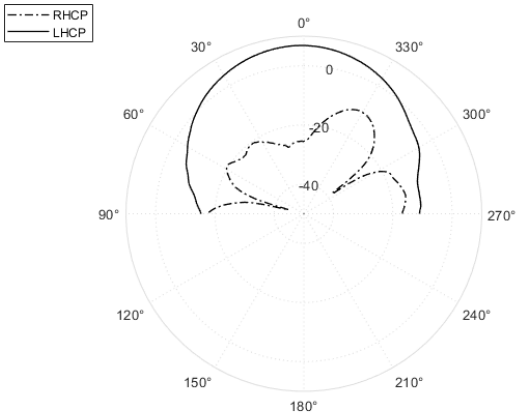

(c)

Figure 5.11: Measured SRA radiation pattern in $\phi = 0^{\circ}$ plane (a) 1.18 GHz (b) 1.25 GHz (c) 1.575 GHz

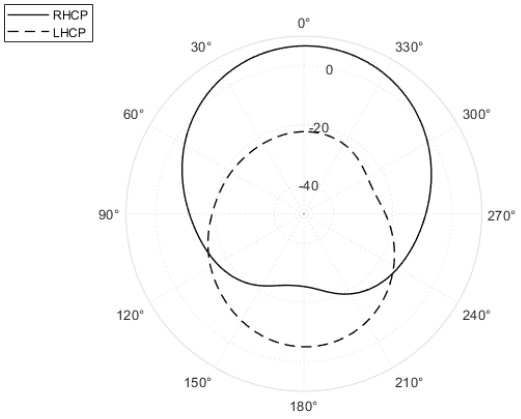

(a)

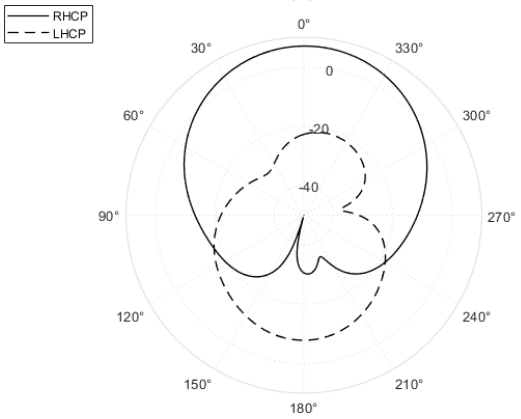

(b)

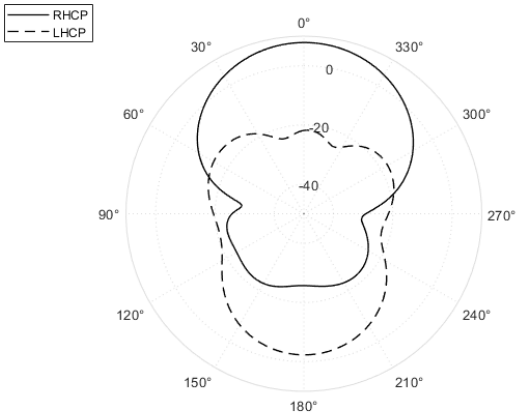

(c)

Figure 5.12: Simulated SRA radiation pattern in $\phi = 90°$ plane (a) 1.18 GHz (b) 1.25 GHz (c) 1.575 GHz

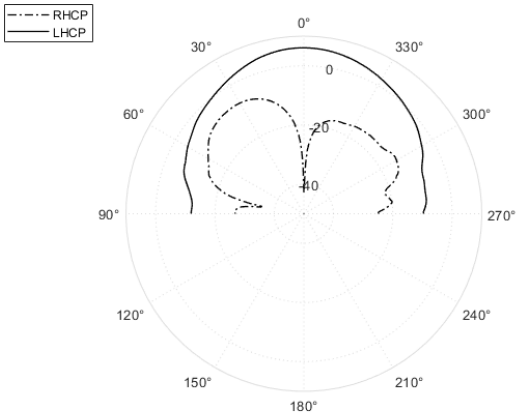

(a)

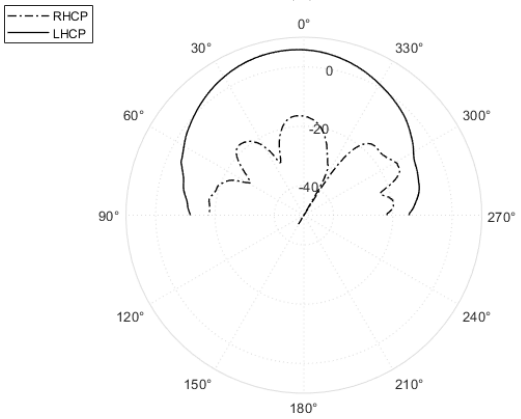

(b)

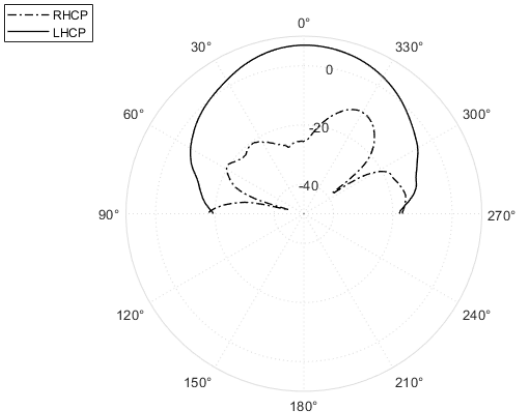

(c)

Figure 5.13: Measured SRA radiation pattern in $\phi = 90°$ plane (a) 1.18 GHz (b) 1.25 GHz (c) 1.575 GHz

However, one issue that continues to be apparent is the stability of the main lobe. Simulated data illustrates this shift by $-2^\circ \leq \theta \leq 7^\circ$ leading to an asymmetrical radiation pattern. Measured results show similar issue with a maximum $-5^\circ \leq \theta \leq 6^\circ$ shift from boresight in the 1.25 GHz radiation pattern. It is possible that this issue is due to the asymmetrical radiation patterns at the element level that propagated through to the array. One thought was that this was due to the array feeding network. Many parametric simulations revealed limited changes to the radiation pattern. Other potential sources of error were investigated such as the position and size of the ground plane slots, stub lengths, position of the UWB BLC and size of the antenna ground plane with no discernible changes to the radiation pattern.

Possible sources of error that cause differences in the radiation pattern and gain could include the modelling of the final fabricated antenna, especially the prepreg material, as it might not have been as precise as expected. In addition, as part of the experimental set-up, the SRA was rigged against the mounting plate, as the bottom of antenna was pressed up against several rubber stoppers which may have been on some of the microstrip traces, affecting the velocity of the guided waves to the antenna elements. Also, fishing line was used to secure the SRA between the patch elements which could have impacted results. Unexpectedly, despite the larger area of the SRA, there was practically no curvature in the SRA like what was seen in the fabrication of Antenna 1. Figure 5.14 captures the top and bottom images of the fabricated SRA. Further details regarding the fabrication of the SRA can be found in Appendix B.

Additionally, an FBR $>$ 10 dB was achieved through simulations, however, due to the inability to conduct the test in a full 360° sweep in θ, this data could not be confirmed experimentally.

With an average measured HPBW $\approx$ 55°, this SRA is not designed to be used as a standalone device as the HPBW is much narrower than the $>$ 100° required to capture the number of satellites needed for reliable positioning. However, with a wider IBW and ARBW, and increased gain, the purpose of this device was to be a primer for a phased array configuration with the addition of a phase shifter network for active control of the main lobe

while the array is in operation.

Table 5.3: 2×2 SRA performance vs. GNSS SRA performance requirements

Parameter	GNSS Performance Requirement	Measured Antenna Performance
IBW	$> 30\%$	$> 43\%$
ARBW	$> 30\%$	$> 43\%$
GBW	$> 30\%$	$> 43\%$
d_n	< 93.4 mm	91.4 mm
Long Dimension	< 210 mm	200 mm
h	< 10 mm	8.74 mm
Phased Array Integration	Simple Port Access?	Yes

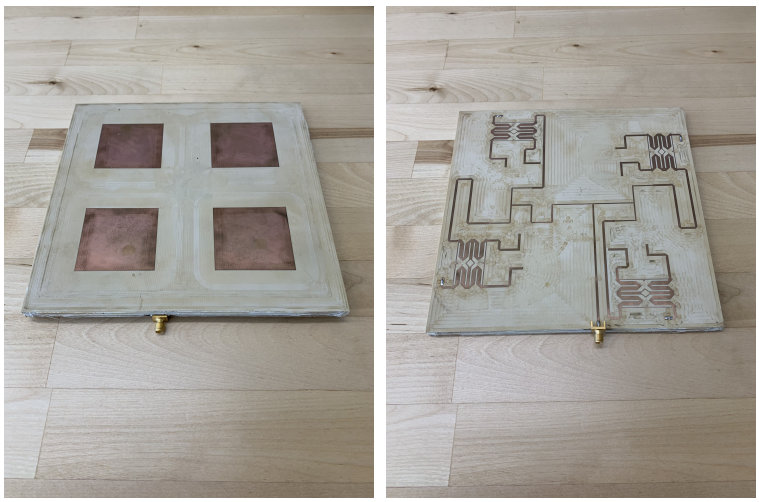

(a) **(b)**

Figure 5.14: SRA fabricated antenna: (a) Top View (b) Bottom View

5.4 Summary

This chapter has presented the investigation of a 2×2 SRA of a dual-fed aperture-coupled stacked-patch antenna of a modified version of the Antenna 1 presented in Chapter 3, through the design, fabrication, and testing phases. This included the design of the antenna element, the simulated mutual coupling between elements and the parallel SRA feed network. In particular, it was important to discover the performance of the array and how beneficial it

would be if it were further implemented into a GNSS phased array.

There were several important conclusions that were reached from this investigation. First, the multi-layer fabrication of the SRA, like Antenna 1, using core laminates and prepreg could be conducted entirely at RMC and achieved good results. In fact, the fabricated SRA works well in comparison to the SRA in [22], with similar IBW and ARBW, while being much smaller in overall area and height. This along with easy access to each of the array elements suggests that this antenna array would be suitable in a phased array configuration provided the radiation pattern is optimized to ensure symmetrical coverage. Simulation testing could not confirm the source of the asymmetry of the radiation pattern, although it is suspected that it may be propagating from design issues inherent at the element level or surfaces waves and scattering within the array. Similar to Antenna 1, due to the error in fabrication, the SRA is LHCP and not RHCP. Luckily, the design of the feed network and the antenna elements proved to be symmetrical with limited change in performance other the polarization of the antenna. Also, due to the limitations of the experimental set-up, the entire radiation pattern could not be captured and thus the FBR could not be confirmed experimentally.

Chapter 6

Conclusion

6.1 Summary of Results

There were several objectives that were studied during this thesis starting with the design of a wideband dual-fed CP aperture-coupled stacked-patch antenna, Antenna 1, for use in GNSS applications. Part of these objectives included the investigation of both a multi-layer and uniform permittivity substrate design. The initial focus of this thesis was the development of Antenna 2, a PCB integrated Antenna design with the addition of a stripline layer and microstrip-to-stripline via transitions, to Antenna 1. However, due to time constraints only initial simulation results could be collected. However, the second established objective was to determine how the aperture-coupled stacked-patch antenna design could be integrated into a 2×2 SRA. In addition, the success of the Antenna 1 and SRA fabricated designs demonstrate that the design of the multi-layer substrate design using only core laminates and prepreg material could entirely be completed at RMC with some substitutions in the procedure that emulate those conducted at state-of-the-art fabrication facilities.

The design of Antenna 1 was conducted in two distinct stages. The first stage was to adapt the design of the UWB BLC feed network from 2.2 GHz down to mid-GNSS L-band 1.4 GHz. Once the simulation of this design met specification, then this feed network was integrated into Antenna 1, a dual-fed aperture-coupled stacked-patch GNSS antenna, which performed well in simulations. After fabrication, experimental tests of Antenna 1 revealed good results with $> 43\%$ IBW, 20% ARBW, 38% GBW with LHCP gain, between $2.2-5.3$ dBic across the

entire L-band. Horn antennas initially were used to measure the performance of the antenna, but was retested using RHCP and LHCP spiral antennas due to sub-optimal performance results. As a result of the subsequent tests, it was discovered that the antenna was in fact LHCP due to the fabrication modelling issue. During the fabrication modelling process, the orientation of the feed network was mirrored with respect to the symmetric axis of the antenna and as such, the polarization of the antenna was reversed with gain and radiation patterns measured as LHCP as opposed to those RHCP that were simulated. However, if the fabrication modelling errors were rectified, it is expected that the magnitude of the experimental results would remain the same, with the correct RHCP antenna polarization and no changes to the AR or $|S_{11}|$ of the system. In addition, Antenna 1 fabricated design measures $115 \times 115 \times 8.74$ mm and is not considered large for GNSS applications as it was < 120 mm in its longest dimension, and height $h < 10$ mm, comparable to other state-of-the-art GNSS patch antennas. However, this antenna was larger than the $d_n > \lambda_0/2$ limit at the high end of the GNSS L-band. The experimental results did not capture the entire radiation pattern as the antenna element could only be swept $-90° \leq \theta \leq 90°$ and therefore the FBR could not be confirmed.

The study of the SRA was conducted in four separated stages. The first stage was to perform an adjustment to the design of Antenna 1, for more optimized use in an array, resulting in Antenna 3. The next stage included the simulation of the mutual coupling between two adjacent elements to ensure suitability in an array configuration. The third stage was the design of a parallel sequential array feed network that would feed all the elements of the 2×2 SRA. This included the integration of the array feeding network with the SRA configuration of Antennas 1 and 3. The final stage included the fabrication and testing of the SRA. Fabrication and testing were completed using the same procedure for Antenna 1. The experimental results matched well with the simulated results of which confirmed that this device has significant potential with an AR < 2.6 dB, $|S_{11}| < -12.7$ dB and a LHCP gain between $5.5 - 7.7$ dBic, though similar to Antenna 1, experimental RHCP results are expected be very similar except for the polarization with the rectification of fabrication modelling errors. Further optimization of the SRA will be required to better

define a symmetrical radiation pattern. The SRA measures 200 mm $\times$ 200 mm $\times$ 8.7 mm which is comparable to other published results. As the same experimental set-up was used with the SRA as with Antenna 1, the FBR could not be confirmed.

6.2 Proposed Future Work

The work and the contributions made herein, will potentially lead to several areas of future research including:

- Investigate ways to further optimize the performance of Antenna 1 such as increasing ARBW and further minimizing its area.
- Further investigate the PCB integrated design, Antenna 2, including the issues surrounding the integration of the stripline layer to confirm whether this element could be further decreased in size and be integrated directly with high frequency electronics.
- Optimize the performance of the 2×2 SRA, especially the radiation pattern to enable seamless integration into a GNSS phased array configuration for future projects such as EW and SOTM applications.
- Develop an optimized procedure for the fabrication of a multi-layer substrate patch antenna including the steps needed to prepare an antenna model for fabrication especially for designs requiring milling or etching on both sides of the same laminate.

Bibliography

[1] Salvatore Liberto, George Goussetis, and Andrew Christie. "Design of a Dual-Circularly-Polarized Stacked Patch Antenna for SOTM application at Ka-band". In: *2020 14th European Conference on Antennas and Propagation (EuCAP)*. Mar. 2020, pp. 1–5. DOI: 10.23919/EuCAP48036.2020.9135835.

[2] Abdulgader Omar, Abbas Omar, and Jamal Hawwary. "A 2x2 Dual-polarization Wideband Microstrip Antenna Array for Ku-band Satellite Applications". In: *2022 45th International Conference on Telecommunications and Signal Processing (TSP)*. 2022, pp. 338–341. DOI: 10.1109/TSP55681.2022.9851393.

[3] Ehsan Gharib Doust et al. "An aperture-coupled circularly polarized stacked microstrip antenna for GPS frequency bands L1, L2, and L5". In: *2008 IEEE Antennas and Propagation Society International Symposium*. 2008, pp. 1–4. DOI: 10.1109/APS.2008.4619440.

[4] Xiaoqing Wu and Lin-Ping Shen. "Compact Ultra-Wideband Microstrip 3dB Branch-Line Coupler Using Coupled-Lines". In: *2022 IEEE International Symposium on Antennas and Propagation and USNC-URSI Radio Science Meeting (AP-S/URSI)*. July 2022, pp. 1462–1463. DOI: 10.1109/AP-S/USNC-URSI47032.2022.9886053.

[5] "IEEE Recommended Practice for Antenna Measurements". In: *IEEE Std 149-2021 (Revision of IEEE Std 149-1977)* (2022), pp. 1–207. DOI: 10.1109/IEEESTD.2022.9714428.

[6] Qi Luo et al. "Design and Analysis of a Reflectarray Using Slot Antenna Elements for Ka-band SatCom". In: *IEEE Transactions on Antennas and Propagation* 63.4 (Apr. 2015), pp. 1365–1374. ISSN: 1558-2221. DOI: 10.1109/TAP.2015.2401393.

[7] Shing-lung Steven Yang et al. "Study on Sequential Feeding Networks for Subarrays of Circularly Polarized Elliptical Dielectric Resonator Antenna". In: *IEEE Transactions on Antennas and Propagation* 55.2 (2007), pp. 321–333. DOI: 10.1109/TAP.2006.889819.

[8] Johnson J. H. Wang. "Antennas for Global Navigation Satellite System (GNSS)". In: *Proceedings of the IEEE* 100.7 (July 2012), pp. 2349–2355. ISSN: 1558-2256. DOI: 10.1109/JPROC.2011.2179630.

[9] Farshid Tamjid et al. "Toward High-Performance Wideband GNSS Antennas-Design Tradeoffs and Development of Wideband Feed Network Structure". In: *IEEE Transactions on Antennas and Propagation* 68.8 (Aug. 2020), pp. 5796–5806. ISSN: 1558-2221. DOI: 10.1109/TAP.2020.2983800.

[10] Fawwaz T. Ulaby and Umberto Ravaioli. *Fundamentals of Applied Electromagnetics, Seventh Edition*. Pearson, 2007. ISBN: 9780133356816.

[11] D.M. Pozar. *Microwave Engineering, 4th Edition*. Wiley, 2011. ISBN: 9781118213636.

[12] Frank B. Gross. *Smart Antennas with MATLAB*. McGraw-Hill Education, 2015. ISBN: 9780071822381.

[13] C.A. Balanis. *Antenna Theory: Analysis and Design*. Wiley, 2012. ISBN: 9781118585733.

[14] Liu Wen et al. "Design of a wideband circularly polarized microstrip antenna for compass and GPS". In: *2013 International Conference on Computational Problem-Solving (ICCP)*. 2013, pp. 195–198. DOI: 10.1109/ICCPS.2013.6893536.

[15] "IEEE Standard Definitions of Terms for Antennas". In: *IEEE Std 145-1983* (1983), pp. 1–31. DOI: 10.1109/IEEESTD.1983.82386.

[16] Penn State College of Earth and Mineral Sciences. *GEOG 160 Mapping Our Changing World*. Online. Available: https://www.e-education.psu.edu/geog160/node/1923. 2023.

[17] Jean Louis Van Belle. *The difference between a theory, a calculation, and an explanation*. Apr. 2020. DOI: 10.13140/RG.2.2.31128.83208.

[18] Jun Xu, Kwai-Man Luk, and Wei Hong. "Low-Profile Wideband Circularly Polarized Complementary Antenna and Arrays for Millimeter-Wave Communications". In: *IEEE Transactions on Antennas and Propagation* 71.3 (2023), pp. 2052–2063. DOI: 10.1109/TAP.2022.3233647.

[19] Daniel Egea-Roca et al. "GNSS User Technology: State-of-the-Art and Future Trends". In: *IEEE Access* 10 (2022), pp. 39939–39968. ISSN: 2169-3536. DOI: 10.1109/ACCESS.2022.3165594.

[20] Hong-Jib Yoon and Byung-Wook Min. "Two Section Wideband 90° Hybrid Coupler Using Parallel-Coupled Three-Line". In: *IEEE Microwave and Wireless Components Letters* 27.6 (2017), pp. 548–550. DOI: 10.1109/LMWC.2017.2701304.

[21] Shaoqing Hu et al. "A wideband antenna for global navigation satellite systems". In: *Proceedings of 2014 3rd Asia-Pacific Conference on Antennas and Propagation*. 2014, pp. 51–54. DOI: 10.1109/APCAP.2014.6992408.

[22] Shailesh Raut and Aldo Petosa. "GPS wideband circularly polarized microstrip antenna array". In: *2009 3rd European Conference on Antennas and Propagation*. 2009, pp. 2990–2993.

[23] Samnada Khairkar et al. "Broadband Branch-Line Coupler using Open Ended Stubs for L-band Microwave Applications". In: *2021 2nd International Conference on Range Technology (ICORT)*. Aug. 2021, pp. 1–4. DOI: 10.1109/ICORT52730.2021.9581621.

[24] K.W. Eccleston and S.H.M. Ong. "Compact planar microstripline branch-line and rat-race couplers". In: *IEEE Transactions on Microwave Theory and Techniques* 51.10 (2003), pp. 2119–2125. DOI: 10.1109/TMTT.2003.817442.

[25] Gao Dong et al. "Research on the influence of vias on signal transmission in multi-layer PCB". In: *2017 13th IEEE International Conference on Electronic Measurement and Instruments (ICEMI)*. Oct. 2017, pp. 406–409. DOI: 10.1109/ICEMI.2017.8265976.

[26] Mario Leib, Michael Mirbach, and Wolfgang Menzel. "An ultra-wideband vertical transition from microstrip to stripline in PCB technology". In: *2010 IEEE International Conference on Ultra-Wideband*. Vol. 2. Sept. 2010, pp. 1–4. DOI: 10.1109/ICUWB.2010.5614563.

[27] A. Bhattacharyya, O. Fordham, and Yaozhong Liu. "Analysis of stripline-fed slot-coupled patch antennas with vias for parallel-plate mode suppression". In: *IEEE Transactions on Antennas and Propagation* 46.4 (1998), pp. 538–545. DOI: 10.1109/8.664118.

[28] John L. Volakis. *Antenna Engineering Handbook, 5th Edition*. McGraw Hill, 2018.

[29] David Pánek et al. "Performance Comparison of Quantized Control Synthesis Methods of Antenna Arrays". In: *Electronics* 11 (Mar. 2022), p. 994. DOI: 10.3390/electronics11070994.

[30] Randy L. Haupt. "Mutual Coupling". In: *Antenna Arrays: A Computational Approach*. 2010, pp. 339–400. DOI: 10.1002/9780470937464.ch6.

[31] L. Lechtreck. "Effects of coupling accumulation in antenna arrays". In: *IEEE Transactions on Antennas and Propagation* 16.1 (1968), pp. 31–37. DOI: 10.1109/TAP.1968.1139110.

[32] H. Singh et al. "Mutual Coupling in Phased Arrays: A Review". In: *International Journal of Antennas and Propagation* (2013). DOI: 10.1155/2013/348123.

[33] M. Akbari, Shraman Gupta, and A. R. Sebak. "Sequential feeding networks for subarrays of circularly polarized patch antenna". In: *2016 IEEE International Symposium on Antennas and Propagation (APSURSI)*. 2016, pp. 587–588. DOI: 10.1109/APS.2016.7696002.

[34] Muhammad Imran Nawaz et al. "A review on wideband microstrip patch antenna design techniques". In: *2013 International Conference on Aerospace Science and Engineering (ICASE)*. 2013, pp. 1–8. DOI: 10.1109/ICASE.2013.6785554.

[35] Shaoqing Hu et al. "A wideband antenna for global navigation satellite systems". In: *Proceedings of 2014 3rd Asia-Pacific Conference on Antennas and Propagation*. 2014, pp. 51–54. DOI: 10.1109/APCAP.2014.6992408.

[36] Xiulong Bao, Arman Mirmanov, and Diego Caratelli. "Wideband Circularly Polarized Slotted Multi-Port Patch Antenna for High-Precision GNSS Systems". In: *2023 IEEE International Symposium on Antennas and Propagation and USNC-URSI Radio Science Meeting (USNC-URSI)*. 2023, pp. 1539–1540. DOI: 10.1109/USNC-URSI52151.2023.10237501.

[37] Chao Sun, Zhao Wu, and Bowen Bai. "A Novel Compact Wideband Patch Antenna for GNSS Application". In: *IEEE Transactions on Antennas and Propagation* 65.12 (2017), pp. 7334–7339. DOI: 10.1109/TAP.2017.2761987.

[38] K.W. Eccleston and S.H.M. Ong. "Compact planar microstripline branch-line and rat-race couplers". In: *IEEE Transactions on Microwave Theory and Techniques* 51.10 (2003), pp. 2119–2125. DOI: 10.1109/TMTT.2003.817442.

[39] Jr. Clyde F. Coombs. *Printed Circuits Handbook*. McGraw-Hill Education, 2016.

[40] Charles Harper. *Electronic Assembly Fabrication*. McGraw-Hill, 2002.

[41] V. Rathi, G. Kumar, and K.P. Ray. "Improved coupling for aperture coupled microstrip antennas". In: *IEEE Transactions on Antennas and Propagation* 44.8 (1996), pp. 1196–1198. DOI: 10.1109/8.511831.

[42] Isola Corp. Isola I-Tera® *MT40 Processing Guide*. 2020.

[43] Q-PAR Angus. *QMS-00315 0.5 - 22 GHz Left Hand Circularly Polarised Spiral Antenna fitted with an SMA type Connector Data Sheet*. 2013.

[44] Q-PAR Angus. *QMS-00315 0.5 - 22 GHz Right Hand Circularly Polarised Spiral Antenna fitted with an SMA type Connector Data Sheet*. 2013.

Appendix A

Antenna 1: Additional Data

A.1 Additional Simulation Results

As part of the initial experimental set-up, two standard horns were used that measured the radiation patterns and gain of the antennas. However, after assessment of the results, and the discovery of wideband CP antennas available for use, these total gain results were not used as official results for this thesis. Instead, the results are included in this appendix as reference.

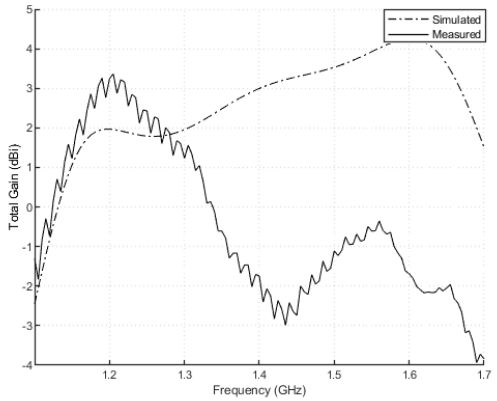

Figure A.1: Antenna 1 total gain at $\theta = \phi = 0°$

Furthermore, although axial ratio beamwidth is a necessary requirement for high performance GNSS antennas, those results are not routinely published in literature. Additionally, since it would have taken many hours to capture the measured axial ratio beamwidth it was

decided to include these results in this appendix. Fig. A.4 illustrates the simulated axial ratio beamwidth of the three L-band frequencies of interest, 1.18 GHz, 1.25 GHz, and 1.575 GHz. The results show that the axial ratio beamwidth varies between $100^\circ - 140^\circ$ which are suitable for GNSS applications. However, like the issue with the radiation pattern instability noted in Chapter 3, it appears as though the axial ratio beamwidth was asymmetric at times, especially at 1.575 GHz seen in Fig. A.4(c). This corresponds to the shift in the radiation pattern seen in Fig. 3.12(c).

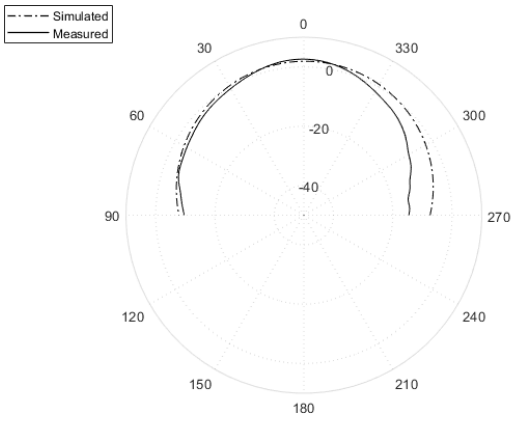

(a)

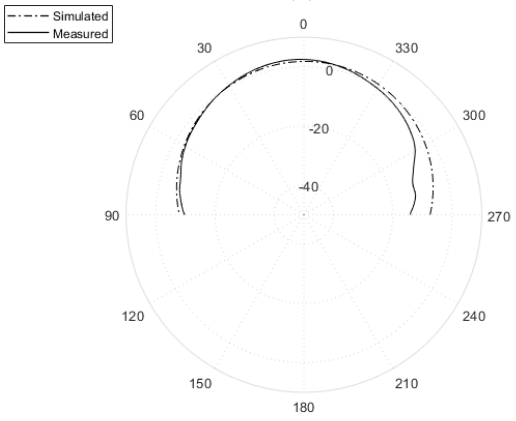

(b)

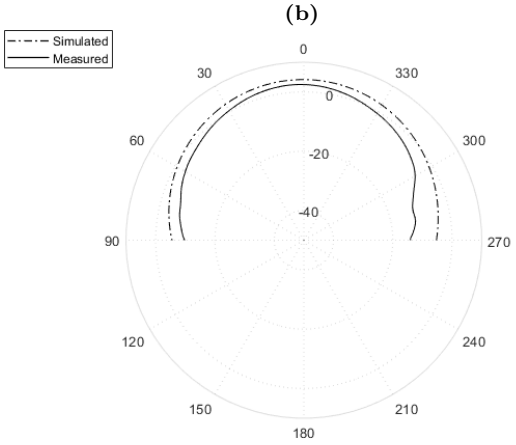

(c)

Figure A.2: Total gain radiation pattern in $\phi = 0°$ plane (a) 1.18 GHz (b) 1.25 GHz (c) 1.575 GHz

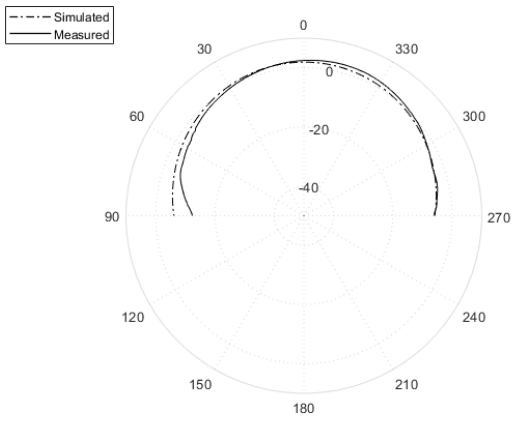

(a)

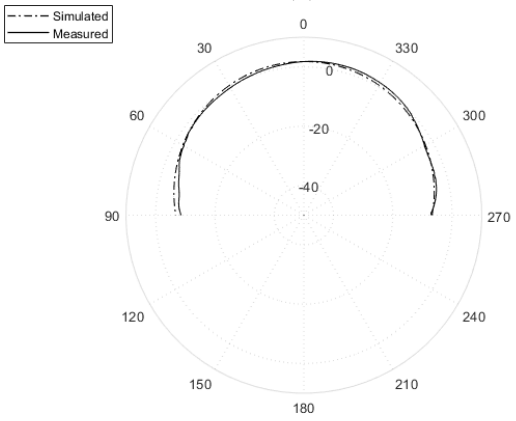

(b)

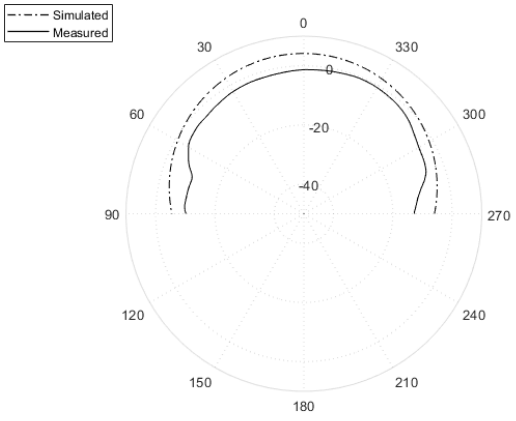

(c)

Figure A.3: Total gain radiation pattern in $\phi = 90°$ plane (a) 1.18 GHz (b) 1.25 GHz (c) 1.575 GHz

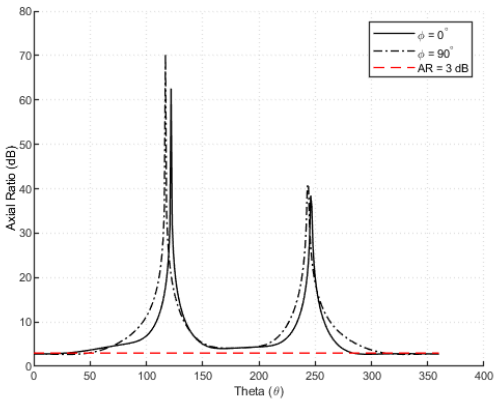

(a)

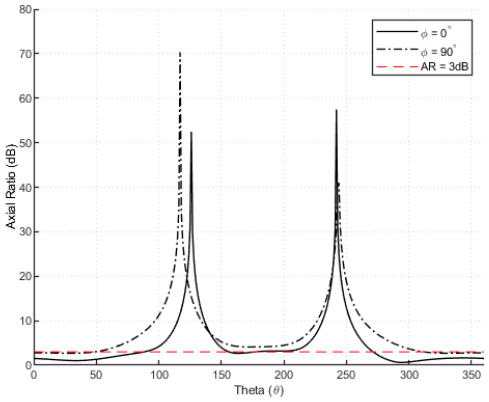

(b)

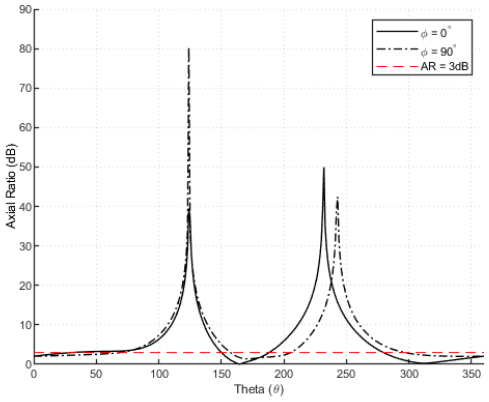

(c)

Figure A.4: Simulated axial ratio beamwidth in $\phi = 0°$ and $\phi = 90°$ planes: (a) 1.18 GHz (b) 1.25 GHz (c) 1.575 GHz

A.2 Fabrication and Experimental Photos

Included in this section are additional photos of the fabrication and experimental testing process at RMC discussed in Chapter 3.

Figure A.5: Antenna 1 pressure plate rig

Figure A.6: Antenna 1 in fabrication oven

Figure A.7: Antenna Chamber Rig Side View Set-up

Appendix B

2×2 Sequentially Rotated Array: Additional Data

B.1 Additional Simulation Results

This appendix presents data that supplements the investigation of the 2×2 SRA in Chapter 5. Similar to the methodology of Antenna 1, an experimental set-up, two standard horns were originally used to measure the radiation patterns and total gain of the antennas. However, after assessment of the results, and the discovery of wideband CP antennas available for use, these total gain results were not used as official results for this thesis. Instead, the results are included in this appendix as a reference.

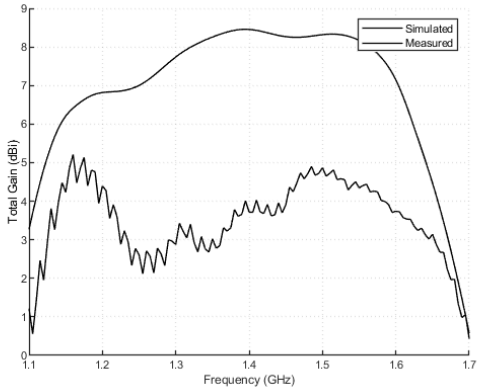

Figure B.1: Simulated SRA total gain at $\theta = \phi = 0^{\circ}$

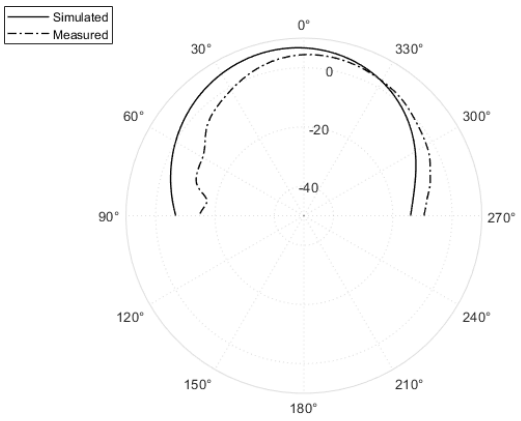

(a)

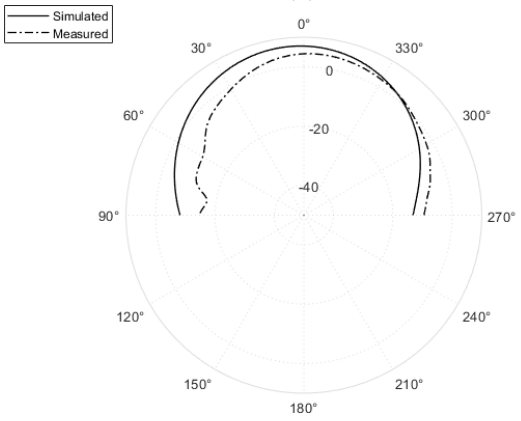

(b)

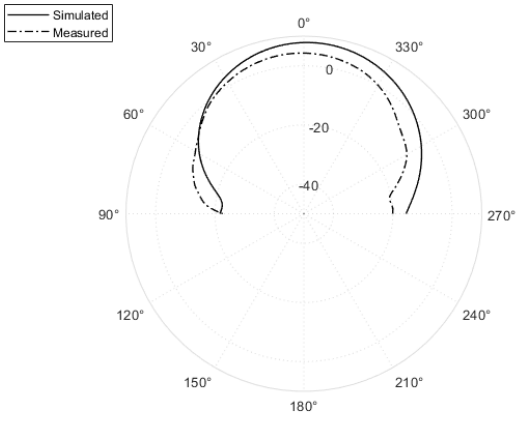

(c)

Figure B.2: Total gain SRA radiation pattern in $\phi = 0°$ plane (a) 1.18 GHz (b) 1.25 GHz (c) 1.575 GHz

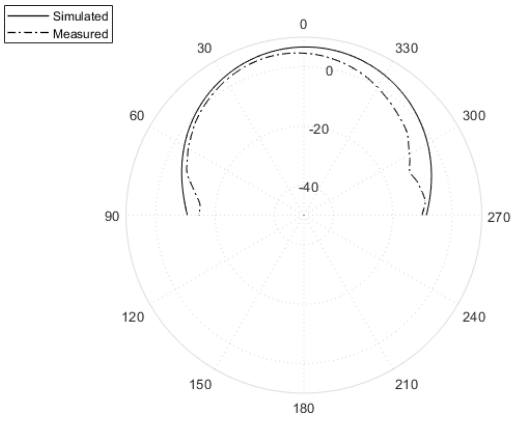

(a)

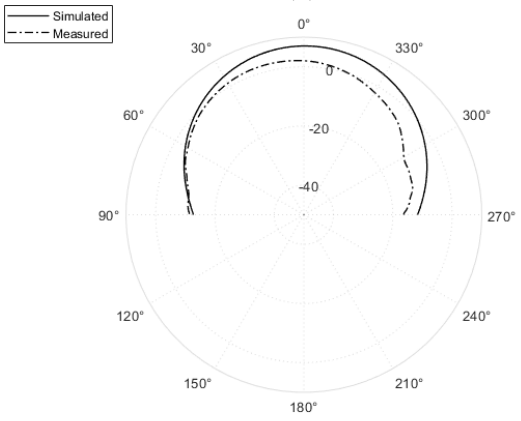

(b)

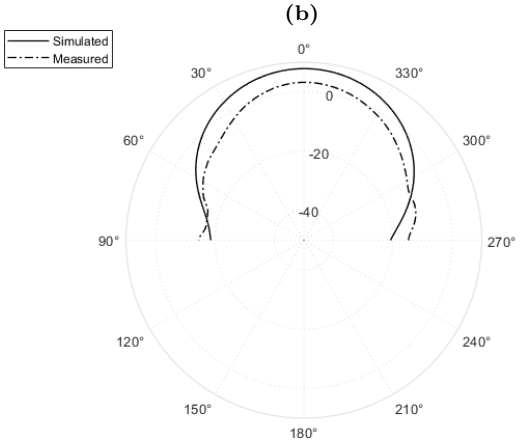

(c)

Figure B.3: SRA radiation pattern in $\phi = 90°$ plane (a) 1.18 GHz (b) 1.25 GHz (c) 1.575 GHz

B.2 Fabrication and Experimental Photos

Included in this section are additional photos of the fabrication and experimental testing process at RMC discussed in Chapter 5.

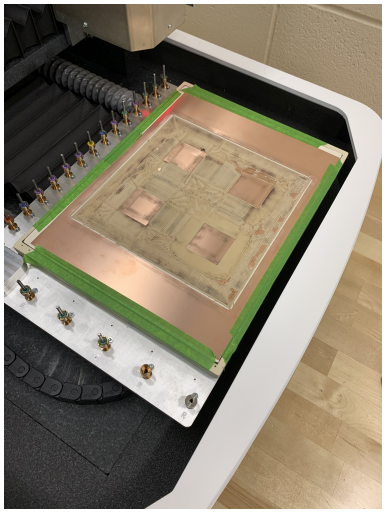

Figure B.4: SRA during milling process

Figure B.5: SRA pressure plate rig

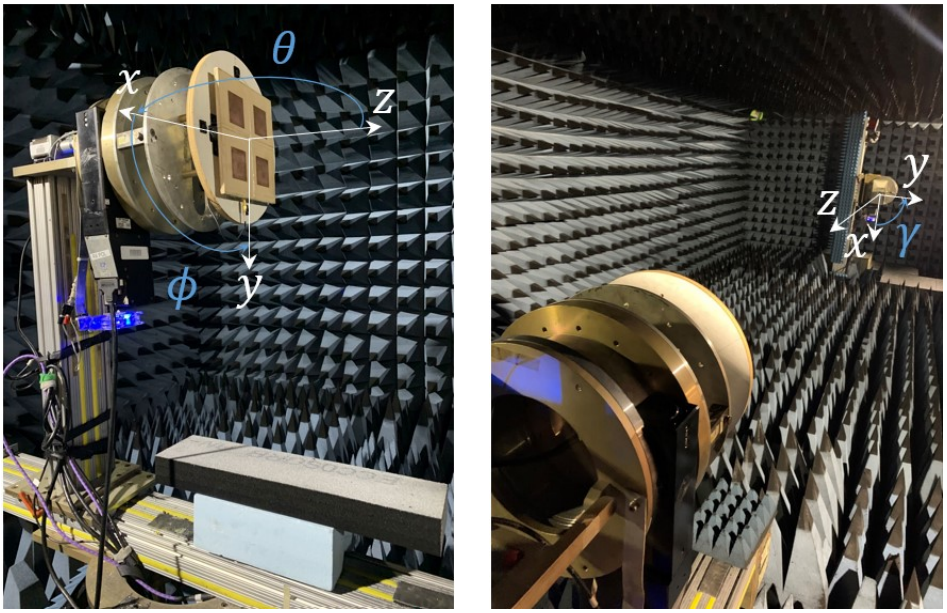

(a) **(b)**

Figure B.6: Experimental test set-up with orientations (a) SRA AUT (b) Source Horn antenna